NEVIS 116

COLUMBIA UNIVERSITY

Department of Physics

Muon Capture in Hydrogen

JOSEPH E. ROTHBERG

NEVIS LABORATORIES

Irvington-on-Hudson, New York

R - 369
CU - 222
NEVIS - 116

Nevis Laboratories
Columbia University
Physics Department
Irvington - on-Hudson
New York

Muon Capture in Hydrogen

JOSEPH E. ROTHBERG

Submitted in partial fulfillment of
the requirements for the degree
of Doctor of Philosophy in the Faculty
of Pure Science, Columbia University

June 1963

Office of Naval Research
Contract Nonr-266(72)

Muon Capture in Hydrogen

Contents

Muon Capture in Hydrogen*

JOSEPH E. ROTHBERG†

Columbia University, New York, New York

---

* Work supported in part by the Office of Naval Research.

† Submitted in partial fulfillment of the requirements for the degree of Doctor of Philosophy in the Faculty of Pure Science, Columbia University.

ABSTRACT

An experiment to measure the muon capture rate in liquid hydrogen was carried out using scintillation counter techniques. The experiment tests muon-electron universality in interaction with a proton at a momentum transfer of 100 MeV/c. The use of ultra-pure liquid hydrogen, a purified muon beam, neutron-gamma ray discriminating detectors and oscilloscope photography made possible the detection of the 5.2 MeV neutron from the relatively improbable capture reaction ($\mu^- + p \rightarrow n + \nu$). Observation of the well known pion capture reaction ($\pi^- + p \rightarrow n + \gamma$) served as a check on many aspects of the experimental arrangement as well as on the neutron detector efficiency calculation. Interpretation of the muon capture experiment depends on knowledge of the muon molecular wave function and the muon-proton spin configuration; these are

known from detailed calculations. The muon molecular formation rate was measured in an independent experiment, but the present result is relatively insensitive to it. The stability of the muon molecular ortho state against transitions to the para ground state for times comparable to the free muon lifetime is confirmed. The experimental result of the capture rate measurement, 464 ± 42 sec^{-1} is compared with 562 ± 60 sec^{-1}, the rate expected on the basis of the conserved vector current theory, muon-electron universality and the accepted value of the "induced pseudo-scalar" coupling constant.

I. INTRODUCTION

A. Status of the Universal Fermi Interaction

The concept of a Universal Fermi Interaction (UFI) governing all weak processes was placed on a quantitative foundation by the discovery that the rate of O^{14} beta decay could be used to predict the muon decay rate rather accurately.[1] It is of great interest to test this hypothesis in the third class of strangeness-conserving weak interactions, the muon-proton interaction.

The muon-proton interaction at low energies is available for study in nuclear muon capture, analogous to K-electron capture. This capture can take place because negative muons stopping in matter will eventually cascade to the lowest Bohr orbit of a muonic atom,[2] a structure that is more tightly bound than a normal atom because of the large muon mass ($m_\mu = 207\ m_e$). The atomic wave function overlap is sufficiently large to make the muon capture interaction competitive with the free muon decay. Most muon capture experiments carried out with complex nuclei have as a prerequisite detailed knowledge of the nuclear wave functions, if accurate inferences about the muon-proton coupling constants are to be made.

A long series of muon capture experiments in complex nuclei has provided some qualitative information on the capture reaction.[3] The axial vector coupling (f) in muon capture was shown to be equal to that in beta decay to within 20-30% by studying the (purely Gamow-Teller) reaction cycle[4]

$$\mu^- + C^{12} \rightarrow B^{12}\ (J = 1 \text{ ground state}) + \nu,\quad B^{12} \rightarrow C^{12} + e^- + \nu.$$

A spin dependent capture rate has been observed[5a] in F^{19}. Measurements of the angular distribution of neutrons from muon capture in calcium[5b] and of muon capture[5c] in O^{16} populating discrete levels of N^{16} yield results that are consistent with a large contribution from the so-called induced pseudo-scalar coupling (see Section II). The muon capture rate in He^3 has been observed to be within about 10% of that expected on the basis of the current theory.[5d]

Experiments were initiated to study muon capture in hydrogen, a system free of nuclear complications, to provide a test of the universality of the V-A weak interaction coupling theory. A complete experimental result would indicate whether or not a muon behaves exactly as an electron does in interactions with a proton. Beta decay experiments involve momentum transfers much lower than the 100 MeV/c available when a muon is captured; an unknown momentum dependence of the effective coupling constants could result in an ambiguity of interpretation.

Previous experiments on muon capture in hydrogen have established the relative sign of the vector and axial vector coupling[6] and have established the presence of a strong vector contribution[7].

A muon-proton coupling scheme of the form vector minus axial vector (V-A) results in a strong spin dependence of the muon capture reaction[8]

$$\mu^- + p \rightarrow n + \nu \qquad (1)$$

If the reaction proceeds from a singlet state then the neutrons are emitted isotropically and are in fact polarized due to

the two component nature of the neutrino. On the other hand if the muon and proton are in an L = 0 triplet state (^3S) then the reaction is inhibited altogether. Momentum dependent contributions to the coupling modify the V,A destructive interference and allow some triplet capture to take place, the singlet rate being altered as well.

B. Experimental Problems in Muon Capture in Hydrogen

1. Specification of the Initial State

The possibility of a spin dependent reaction rate makes accurate specification of the initial muon proton state vital to an interpretation of experimental results. The history of a negative muon[2] after considerable reduction of velocity in liquid hydrogen (density = 0.07 gm/cc) proceeds as follows (see Fig. 1). At a low velocity the muon is captured by a proton and cascades to the lowest Bohr orbit (the 1s state) in about 10^{-9} sec,[9] this atomic system is formed in a statistical mixture of triplet and singlet states. The (μp) system is small (Bohr radius $\equiv a_\mu = a_e \cdot m_e/m_\mu$), neutral and completely detached from the hydrogen molecule from which it was formed. It is able to wander through the hydrogen, the muon being exchanged from proton to proton. If the liquid hydrogen is pure the result of these exchanges is a 100% population of the energetically lower singlet state and total depolarization of the muons. If even small amounts of deuterium or other atoms are present then it is more or less likely that one of the exchanges will leave the muon bound to a deuteron (or heavier atom) which it will not subsequently

leave. In the case of (μd) the reduced mass effect makes that system more tightly bound by 130 eV than a (μp) system. In pure liquid hydrogen the singlet (μp) system will eventually (in about 0.6 μsec) become part of a $(p\mu p)^+$ molecular ion[10] if the muon has not decayed first (with lifetime 2.2 μsec).

The molecular ion is a stable configuration and it is from this system that the muon is most likely to be captured or to decay. In this experiment the time of each capture event is measured; thus if the transition rate λ_{pp} from a (μp) system to a ($p\mu p$) is known then the configuration from which capture takes place is also known. The transition rate has been measured in a separate experiment.[10,11] Only capture events which have originated in a ($p\mu p$) system have been included in the analysis. Measurements of the muon capture rates using a bubble chamber include contributions from both atomic and molecular capture since time measurement is impossible. There are two questions concerning the nature of the molecular ion which must be considered and which have been answered by detailed calculations: (1) What is the angular momentum character of the molecular ion and hence what is the composition in terms of singlet and triplet (μp)? (2) What is the wave function overlap of the muon and proton? The $(p\mu p)^+$ molecular ion is almost invariably formed in the ortho state[12] (para formation is $\lesssim 10^{-3}$ smaller) and it has been shown with a high degree of confidence that only states with total spin = 1/2 are present.[13] It then follows (see Appendix IV) that the capture rate from the molecular ion is given by $2\gamma_o(3/4\ \lambda_s + 1/4\ \lambda_t)$, where the λ's refer to

the capture rates in the triplet and singlet atoms and $2\gamma_o$ is a wave function overlap factor for the ortho molecule. Although the para state is the molecular ion ground state, it can be shown that transitions to it are extremely unlikely during the muon lifetime.[12] The capture rate in this state is lower, however, being given by $2\gamma_p(1/4\ \lambda_s + 3/4\ \lambda_t)$, and any appreciable amount of conversion to it could be detected in this experiment.

2. The Expected Rate

On the basis of the V-A interaction with certain correction terms included, the rate of reaction (1) when the muon is bound in the molecular ion is expected[8] to be about 560 sec^{-1}. The decay of the muon

$$\mu^- \rightarrow e^- + \nu + \tilde{\nu} \qquad (2)$$

which is not appreciably affected by the muon being bound in a hydrogen orbit (binding energy = 2.5 keV) takes place at the rate[14] 0.455×10^6 sec^{-1}, so that capture is only 1/1000 as likely as decay. In the case of nuclei of higher atomic number the capture rate increases at least as fast as Z^3 due to the increased muon-nucleus overlap ($a_o \sim 1/z$) and is equal to the decay rate at Z = 12 (magnesium).

3. Detection of Capture Events

The only signature of a muon capture event is the detection of the 5.2 MeV neutron in reaction (1). The experimental arrangement for measuring the muon capture rate must be able to distinguish this neutron from all background and

must detect it with known efficiency relative to the number of available muons. Because of the possibility of transfer of a muon to deuterium or other impurities in the hydrogen the experiment must be carried out under ultra-pure conditions. Whereas in a gas the various molecular transfer rates would be under control of the pressure and it would be possible to alter at will the ratio of triplet and sirglet states[8] beam intensity considerations make it difficult to use a gas target at reasonable pressure, thus liquid hydrogen was chosen as the target material. Gamma rays produced in the bremsstrahlung of decay electrons [reaction (2)] constituted an intense source of neutral background which could not be eliminated by shielding. The neutron detectors that were employed were capable of distinguishing between neutrons and gamma rays eliminating much of the background problem; they were simulaneously used for decay electron detection.

The known rate of the pion capture reaction

$$\pi^- + p \rightarrow n + \gamma \qquad (3)$$

emitting an 8.9 MeV neutron made it possible to perform a control experiment in situ.

The experiment to be described here is an extension and refinement of a similar experiment previously performed at this laboratory.[7] Evaluation of the earlier experiment resulted in minor improvements in the target, meson beam and running procedures that were incorporated into the present experiment.

II. THEORETICAL BACKGROUND

The muon capture rate is given by

$$w = \frac{1}{2\pi^2} \frac{k^2 E}{m_\mu + M_N} |M|^2 a^{-3} \tag{4}$$

where k is the neutrino momentum, a is the muon atomic Bohr radius and M is the matrix element. This has been derived by assuming a hydrogenic wave function for the muon initial state

$$\Psi(r) = (\pi a^3)^{-\frac{1}{2}} \exp(-r/a) \tag{5}$$

and then integrating the matrix element over all momenta that are relevant; the integral can be approximated by

$$M = (2\pi)^{3/2} M(0) \Psi(0) \tag{6}$$

where M(0) is the matrix element evaluated at zero initial momentum and $\Psi(0)$ is the wave function evaluated at the origin. The matrix element can be written[15] as

$$M \sim \sum_i g_i \bar{u}_\nu O_i u_\mu \langle n|J_i|p\rangle \tag{7}$$

where the O_i are the usual operators S, V, A, T, P and the sum is taken over as many of them as are present. In the limit of small momentum transfer and treating nucleons as though strong interactions were absent the matrix element reduces to the form

$$M \sim \sum_i g_i (u_\nu O_i u_\mu)(\bar{u}_n O_i u_p) + g_i' (\bar{u}_\nu O_i u_\mu)(\bar{u}_n O_i \gamma_5 u_p) + \text{h.c.} \tag{8}$$

If in addition the interaction is taken as V,A and the coefficients of the odd parity terms g_i' in the Hamiltonian

are equal in magnitude to those of the even parity terms, the matrix element becomes

$$M \sim g_V \bar{u}_\nu \gamma_\mu (1+\gamma_5) u_\mu (\bar{u}_n \gamma_\mu u_p) + g_A u_\nu \gamma_\mu \gamma_5 (1+\gamma_5) u_\mu (\bar{u}_n \gamma_\mu u_p) + \text{h.c.} \tag{9}$$

In the non-relativistic limit the vector operator reduces to unity while the axial vector operator reduces to $\vec{\sigma}$, the spin matrix so that the matrix element becomes proportional to

$$M \sim g_V + g_A \langle \sigma_\mu \cdot \sigma_p \rangle \tag{10}$$

The term $\langle \sigma_\mu \cdot \sigma_p \rangle$ can be evaluated from the relationship $(\sigma_\mu + \sigma_p)^2 = 3 + 3 + 2\sigma_\mu \cdot \sigma_p$ for the singlet and triplet cases

$$\lambda_s \sim \left| g_V - 3g_A \right|^2 \quad \text{and} \quad \lambda_t \sim \left| g_V + g_A \right|^2 , \tag{11}$$

Using the relationship $(\sigma_\mu \cdot \sigma_p)^2 + 2(\sigma_\mu \cdot \sigma_p) - 3 = 0$, the square of the matrix element can be written in general as

$$M^2 \sim g_V{}^2 + 3g_A{}^2 + 2(g_V g_A - g_A{}^2) \langle \sigma_\mu \cdot \sigma_p \rangle \tag{12}$$

The table below lists numbers (M^2) proportional to the capture rate for either of the two initial spin states; we assume that the coupling constants are equal in magnitude.

TABLE I

Muon Capture Matrix Element

Initial State	Coupling Const.	$\langle \sigma_\mu \cdot \sigma_p \rangle$	M^2
singlet	$g_V = g_A$	-3	$4g_V^2$
triplet	$g_V = g_A$	+1	$4g_V^2$
singlet	$g_V = -g_A$	-3	$16g_V^2$
triplet	$g_V = -g_A$	+1	0

Thus the equality of sign of the coupling constants results in no hyperfine effect while the expected V-A theory results in a much larger capture rate in the singlet state but no triplet state capture at all.

In order that the Hamiltonian be invariant under time reversal the coupling constants must be relatively real. In the case of the free neutron decay, the phase angle between g_V^β and g_A^β was shown[16] to be approximately 180°. If it is assumed that $|g_V^\mu| = |g_A^\mu|$ but that they have a relative phase φ, then the expressions for the singlet and triplet muon capture rates become $\pi_s \sim g_V^2(10 - 6 \cos \varphi)$ and $\lambda_t \sim g_V^2(2 + 2 \cos \varphi)$ and a system involving 3/4 singlet capture and 1/4 triplet would then have a capture rate $\lambda \sim g_V^2(8 - 4 \cos \varphi)$. The usual choice of $\varphi = \pi$ results in the maximum capture rate.

The above treatment of the strongly interacting particles is, of course, not legitimate. The part of the Hamiltonian

which concerns the neutron and proton can be handled phenomologically by writing the vector and axial vector part of the matrix element $\langle n|J_i|p\rangle$ in the most general form consistent with the known conservation laws. Assuming Lorentz invariance, parity invariance and time-reversal invariance, which hold for strong interactions, we write[17]

$$\langle n|J_V|p\rangle = \bar{u}_n \left\{\gamma_\lambda F_V(q^2) + \sigma_{\lambda p} iq_\rho F_M(q^2) + iq_\lambda F_S(q^2)\right\} u_p \ . \quad (13)$$

$$\langle n|J_A|p\rangle = \bar{u}_n \left\{\gamma_\lambda F_A(q^2) + \sigma_{\lambda p} iq_\rho F_{PT}(q^2) + iq_\lambda F_p(q^2)\right\} \gamma_5 u_p . \quad (14)$$

The J quantities are currents with the appropriate isotopic spin properties to convert the initial proton state to the final neutron state, the u's are Dirac wave functions; the entire complication of strong interactions has been absorbed into the F's which are form factors evaluated at the momentum transfer of the reaction ($q = 0.95\ m_\mu$). At zero momentum transfer the above expressions reduce to the familiar form with $F_V(0)$, $F_A(0)$ equal to 1 and the other terms vanishing because $q = 0$. The functions of momentum transfer, F, can be interpreted as amplitudes for interaction diagrams involving intermediate pion states. See Fig. 2 for examples of such diagrams.

The requirement that each term in the matrix elements have the same properties under G transformation ($G = Ce^{i\pi T_2}$) allows two terms to be eliminated: F_S and F_{PT}. The hypothesis of the Conserved Vector Current holds that the vector part of the interaction J_V is a conserved quantity and that it can be obtained from the vector electromagnetic currect J_λ^V

by a rotation in isotopic spin space;[1] the weak interaction current being proportional to $T_1 - iT_2$ and the other to T_3. As a consequence of this assumption one can identify the two terms F_V and F_M as follows:

$$F_V(q^2) = F_1(q^2) \tag{15}$$

$$F_M(q^2) = (1/2M)(\mu_p - \mu_n)\ F_2(q^2), \tag{16}$$

where F_1 and F_2 are the electric and magnetic form factors for nucleons and the μ's are anomalous magnetic moments: $\mu_p = 1.793$ and $\mu_n = -1.913$. Using also $F_1(q_o^2)$ for $q_o^2 = 0.9\ m_\mu^2$ the matrix element becomes proportional to the following expression (ν is the neutrino momentum)

$$M \sim G_V + G_A \langle \sigma_\mu \cdot \sigma_p \rangle - G_p \langle (\sigma_\mu \cdot \nu)(\sigma_p \cdot \nu) \rangle \tag{17}$$

where the new coupling constants are defined as

$$\begin{aligned} G_V &= g_V\left(1 + \frac{\nu}{2M}\right) \\ G_A &= g_A - g_V(1 + \mu_p - \mu_n)\ \frac{\nu}{2M} \\ G_P &= \left[g_P - g_A - g_V(1 + \mu_p - \mu_n)\right] \frac{\nu}{2M} \end{aligned} \tag{18}$$

In this expression the coupling constants g_V, g_A and g_P are proportional to F_1, F_A and F_P; they are the muon dressed-nucleon coupling constants associated with muon capture. The assumption of a universal Fermi interaction in which muons and electrons are coupled in the same way in weak interactions implies that the "bare" coupling constants that are effective in beta decay and muon capture are equal. The muon

dressed coupling constants and the electron dressed coupling constants then differ because of momentum transfer differences. The relationship[15] between these two sets of coupling constants is:

$$g_V^\mu = 0.97\ g_V^\beta \tag{19}$$

$$g_A^\mu = 0.999\ g_A^\beta \tag{20}$$

The induced pseudoscalar coupling constant g_p has been calculated, using dispersion theory and the pion decay rate, and has been found to be equal to[18]

$$g_p = 8 g_A\ . \tag{21}$$

Beta decay experiments[19] on the free neutron and the decay of O^{14} permitted evaluation of the ratio g_A^β/g_V^β as soon as it was clear that the Fermi and Gamow-Teller matrix elements contain no contribution other than V and A. Experiments give

$$g_A^\beta = -1.2\ g_V^\beta \tag{22}$$

The muon capture rate in hydrogen can finally be written explicitly[8] if the measured beta-decay rate is used to evaluate the numerical constants.

$$w = 158 \left[(g_V^\beta)^2 + 3(g_A^\beta)^2 \right]^{-1} \left(a + b\langle \sigma_\mu \cdot \sigma_p \rangle \right) \tag{23}$$

where

$$\begin{aligned} a &= G_V^{\,2} + 3\Gamma_A^{\,2} \\ b &= 2(G_V G_A - \tfrac{1}{3} G_V G_p) - 2(G_A^{\,2} - \tfrac{2}{3} G_A G_p) \\ \Gamma_A^{\,2} &= G_A^{\,2} + \tfrac{1}{3} (G_p^{\,2} - 2 G_A G_p) \end{aligned} \tag{24}$$

With the accepted values of the coupling constants, one has for the singlet and triplet atomic capture rates:

$$\lambda_s = 636 \text{ sec}^{-1}$$

$$\lambda_t = 13 \text{ sec}^{-1}.$$

A calculation including higher relativistic corrections and a slightly different value for the ratio of beta decay coupling constants ($g_A^\beta/g_V^\beta = -1.25$) yields somewhat different capture rates:[20]

$$\lambda_s = 713 \text{ sec}^{-1}$$

$$\lambda_t = 16.9 \text{ sec}^{-1}$$

The calculated values of the muon-proton overlap factors (in units of $1/\pi a_\mu^3$) for the ortho and para molecules are[12]

$$2\gamma_o = 1.165 \qquad 2\gamma_p = 1.308.$$

Due to uncertainties in the molecular wave function, these numbers are estimated[21] to be correct to within about 10% (the wave function expansion coefficient is m_μ/M_p). The muon-proton spin correlation in the molecular states (see Appendix IV) implies molecular capture rates:

		$g_A/g_V = -1.2$	$g_A/g_V = -1.25$
λpara	$= 2\gamma_p(\frac{1}{4}\lambda_s + \frac{3}{4}\lambda_t)$	$= 220 \text{ sec}^{-1}$	249 sec^{-1}
λortho	$= 2\gamma_o(\frac{3}{4}\lambda_s + \frac{1}{4}\lambda_t)$	$= 560 \text{ sec}^{-1}$	630 sec^{-1}

There have been three previous measurements of the hydrogen capture rate. One was performed in this laboratory and was the precursor of the experiment herein described; the others were both performed using a bubble chamber to detect the stopping muon and the neutron induced proton recoil. In the bubble chamber experiments capture events are recorded which took place in both the atomic and molecular systems and the expected capture rate (using $\lambda_{p\mu p} = 1.9 \times 10^6$ sec^{-1}) is then about 4% higher than that in the molecule. The three previous results are

Columbia[7]	515 ± 85 sec^{-1}
Chicago [22]	435 ± 100 sec^{-1}
CERN [23]	420 ± 75 sec^{-1} .

III. EXPERIMENTAL PREREQUISITES

A. Target

Because of the possibility that a muon, even after having reached the ground state of a μp atom, may be transferred to an impurity of higher atomic number, it is essential to carry out the muon capture experiment in ultra-pure hydrogen. Assuming the transfer rate to impurities, such as nitrogen, to be 5×10^{10} sec^{-1} (several times that to deuterium) and a concentration of one part per million (1 ppm) then the number of muons ending up bound to the impurity atom is $2\frac{1}{2}$% of the number available. If the muon capture rate were 100 times greater in the impurity than in hydrogen the effect that one seeks to

measure would be overwhelmed by nitrogen captures. It is then clear that one must take extraordinary precautions with the purity of the hydrogen; even the presence of deuterium cannot be tolerated at concentrations greater than a few parts per million. Isotopically pure hydrogen was purchased from l'Aire Liquide, Paris. This hydrogen was further purified at the entrance to the hydrogen target by passing it into a heated palladium coil; only hydrogen forms the appropriate chemical bond with palladium that allows it to diffuse through the walls of the tube, other gases do not penetrate the coil and are eliminated. This purification system was subjected to a series of stringent tests of which two examples follow. In a test for nitrogen transmission the system following the palladium purifier was evacuated; nitrogen under pressure was admitted to the input end of the palladium coil and the output pressure was watched. No change in pressure was detected, implying a maximum leak through the palladium of 1 part nitrogen to 10^8 parts hydrogen. To test for helium transmission a conventional helium leak detector was connected to the output end of the purification system and the input end was placed under helium pressure; no net increase in helium at the output was detectable. The closed system "leaked up" at the rate of 5×10^{-6} mm of Hg/hr. at a temperature of 50° C.

Liquid hydrogen was chosen as the target material for the muon capture experiment; its specific gravity, while only 0.07 (near atmospheric pressure), is much greater than that of the gas at convenient pressures. The low temperature of the liquid

(20.4° K) should retard the outgassing of foreign materials from the walls of its container. Because the experiment must be carried out in ultra pure hydrogen, the gas phase was purified and then liquefied within the target itself; this was accomplished by keeping the target region closed and in thermal contact with a reservoir of normal liquid hydrogen. At a very slight pressure above atmospheric the entering gas from the purification system liquefied in the previously evacuated target volume (see Fig. 3). The filling procedure took approximately 20 hours during which time the normal liquid hydrogen, absorbing the heat of condensation, was frequently replenished. Once the target was full heat losses were quite small. The target remained full for several weeks with no deterioration in purity and required no maintenance except for refilling of the liquid hydrogen and liquid nitrogen reservoirs.

Before filling, the "pure system" was evacuated to a pressure of 10^{-6} mm and baked for several days to release materials adsorbed on the walls. An ion pump backed by a chemical adsorption pump was used to evacuate the system; this is preferable to the more usual oil diffusion pump since it eliminates the possibility that carbon and carbon compounds will contaminate the volume being evacuated. At liquid nitrogen temperature the pressure was 6×10^{-7} mm of Hg.

The necessity of subjecting the target to a wide range of temperature and pressure conditions dictated to some extent the choice of target materials. The primary requirement was, however, that it be constructed exclusively of elements with

high atomic number to minimize the effect of muons which might stop in the target walls. Although the muon capture rate increases roughly as Z^3, the muon lifetime in the atomic ground state is already as low as 0.2 μsec in the case of iron as compared to 2.2 μsec in hydrogen so that one has only to delay data taking for a μsec after which the entire effect of wall captures has disappeared. The inner hydrogen target was constructed of stainless steel for mechanical strength and was lined with silver to provide a very high Z barrier for muons headed toward the walls. A silver thermal radiation shield held at liquid nitrogen temperature was suspended inside the vacuum jacket whose outer wall was fabricated of zirconium. Figure 4 shows the thickness and location of the target walls and window. The target window through which the muon beam enters was made as thin as safety permitted in order to decrease the number of muons stopping in it and, more important, to minimize multiple scattering of the beam which would increase the likelihood of wall captures in the vicinity of the neutron detectors.

Table II lists the composition of the target side walls and front window. Under the conditions of the experiment with 60 MeV incident muons and 26 MeV muons entering the target, one can estimate the root mean square scattering angle due to multiple scattering in the front window and in the $2\frac{3}{4}$ in. of beryllium moderator which precedes it. The front window produces an rms angle of 4.5° while the moderator scatters through roughly 2.3°. Since the multiple scattering in the hydrogen is quite

negligible, at least until the very end of the muon range, one can predict the rms spread of the beam in the vicinity of the neutron detectors due to these two sources. The beryllium is at a mean distance of 16 in. from the neutron detectors, whereas the front target window is only 9 in. from the detector center line. Thus the spread due to scattering is 0.6 in. due to the moderator and 0.7 in. due to the window.

It is difficult to use these numbers to estimate the number of wall stopping muons, partly because the beam entering the moderator may itself have an angular divergence of perhaps 8^{o}, considering the collimator geometry.

The pure hydrogen chamber in the target extends for a distance of 13 in. beyond the neutron detector center; the back wall is zirconium but it is extremely unlikely that any muon can penetrate the entire length of the target. The "dirty" liquid hydrogen cooling reservoir and the liquid nitrogen supply which cools the radiation shield are situated behind the pure target which protrudes forward into the detector assembly.

B. Meson Beam

While the hydrogen target was in preparation, studies were undertaken to improve the composition of the available meson beam. In normal operation of the Nevis Synchro-cyclotron the circulating proton beam strikes a target located at a radius of about 72 in. Negative pions produced in the forward direction are bent sufficiently in the fringe field of the cyclotron to pass through an evacuated channel in the main shielding wall (see Fig. 5). Momentum selection is accomplished by the action

of the fringe field and the small acceptance angle of the beam channel. The only muons which are able to enter the experimental target area are those which originate from pion decays in the vicinity of the cyclotron target; the typical radius of the muon source is 2 in. or 3 in. Most muons from decays along the flight path strike collimator walls and are lost. The negative meson beam is also rich in electrons which are produced when the gamma rays from the decay of neutral pions materialize in the cyclotron target. The usual particle ratio in the negative beam is approximately

Pions : 7

Electrons : 7

Muons : 1 .

For the purpose of performing the muon capture experiment this situation was considered unsatisfactory for the following reasons: First, pions stopping in the vicinity of the hydrogen target would produce uncorrelated neutron background with a wide energy spectrum; Second, electrons in the beam would be electronically indistinguishable from muons and would make an accurate determination of the number of muons stopping in the hydrogen quite difficult; they would also increase the number of accidental delayed "muon" -neutron coincidences.

Since the source of muons is more diffuse than that of pions and electrons it is possible, by suitable adjustment of the bending magnet current outside the shielding wall, to reduce greatly the transmission of the unwanted particles while at the same time to decrease the number of muons in the beam by

less than a factor of 2. Searches for the optimum conditions for this purified beam were undertaken using an analog time-of-flight system.[28] Two scintillation counters (#0 and #2) employing 56AVP photomultipliers were placed about 6 meters apart; the output pulses from these were used as the start and stop pulses in a 1/4 nsec resolution time-to-height converter whose output was displayed in a 100 channel pulse analyzer. At the particle momenta of interest (about 120 MeV/c) the pions and muons could be easily resolved. The mass spectrum that was obtained in this way was checked from time to time by measuring the differential stopping rate of the beam as a function of absorber thickness. The working conditions that were finally chosen involved an increase in bending magnet current to select muons of 128 MeV/c, this momentum is about 15% higher than the momentum of the majority of the pions which are normally transmitted through the shielding wall (beam channel "D"). Under these conditions less than 2% of the beam particles were pions and electrons.

Typical differential beam stopping distributions as a function of moderator thickness are shown in Fig. 6 for the purified and unpurified situations. Fig. 7 shows the mass spectrum of the beam consisting of pions, muon and electrons as the purification is improved.

In normal cyclotron operation the proton beam strikes a stationary target; for about 500 μsec the protons circulating with increasing radius continue to produce mesons. Shortly after the ejection time the radio-frequency accelerating voltage is turned off and the cyclotron is dormant until the frequency modulating condenser blades have rotated into proper phase for

the beginning of the next acceleration cycle. Thus only 1/2 msec out of the $16\frac{2}{3}$ msec period is used for experiments. The cyclotron "duty-cycle" is said to be equal to 30 in this case, the average time between mesons being 30 times shorter than it would be if they were produced at a uniform rate at all times. Close spacing increases the chances of a random or accidental coincidence between a muon pulse and a background neutron pulse also produced during ejection time. A method was developed[24] to improve the duty-cycle by a factor of 10. The fixed target is replaced by a target which vibrates in a vertical plane in phase with cyclotron operation. The accelerating voltage is removed when the proton beam reaches the radius of the target; it continues to circulate at this radius while the target moves upward into the beam. Vertical oscillations of the proton beam together with the relatively slow motion of the target permit beam ejection during the entire 8 msec that the radio-frequency accelerating voltage is off. The experimental electronic logic is gated on only during this time and receives about 75% of the total beam available with fixed target operation.

C. Background

In view of the very low yield of neutrons to be expected from the muon capture process, extensive measures were taken to reduce the neutron background. A directional neutron detector was constructed by embedding a cylindrical 2 liter volume of liquid scintillator capable of neutron-gamma ray discrimina-

tion in a 5 ft cube assembly of steel and lead, which was slung from a crane over the cyclotron experimental floor. The array had an angular resolution of 20° to 30°, and was capable of moving horizontally and vertically as well as being rotated. Several weak points in the shielding wall were located and corrected, and the plane of proton orbits was verified to be a source of neutron background. As a result of these studies an optimum working location on the cyclotron floor was chosen and a shielded "house" was constructed of 6 in. thick iron barbettes; extra steel and zinc shielding was installed in the direction of the open channel. It was decided to arrange for the neutron detectors used in the experiment to be located out of the median or proton plane. Once the major sources of background had been eliminated the remainder was observed to be rather isotropic in angular distribution. A steel roof several feel thick was placed over the basic structure and the interior of the "house" was lined with paraffin. An effort was made to use diverse materials for shielding to avoid transmission of neutrons at certain specific energies due to peculiarities of individual neutron cross sections. In the vicinity of the neutron detectors boron-loaded paraffin, which lacks the annoying 2.2 MeV capture gamma ray characteristic of most hydrogenous materials, was used; finally, several inches of lead surrounded each neutron detector. As a result of the extensive shielding arrangement the background counting rate was less than 0.25 neutrons per second per liter of detector in the energy range of interest. The effective background rate was reduced further by electronic requirements to be discussed below.

D. Measurement of Molecular Constants

Using the same hydrogen target and beam conditions, an experiment was performed to measure several molecular constants as well as (pd) fusion parameters. Of greatest interest to the present experiment was measurement of λ_{pp}, the (μp) to (pμp) conversion rate. This is covered in greater detail in the thesis of E. Bleser,[11] and will be reviewed briefly here.

In the presence of a small amount of deuterium some of the (μp) atoms are diverted from their normal tendency to form the (pμp) molecular ion. The muon which is continually being exchanged from proton to proton may become attached to a deuteron from which, because of its increased binding energy, it will no longer be transferable back to a proton, but will form (pμd) which may undergo fusion. A measurement of the yield of the 5.5 MeV fusion gamma rays ($p + d \rightarrow He^3 + \gamma$) as a function of the deuterium concentration (c) determines λ_{pp} if the transfer rate to a deuteron (λ_e) is known. One method of extracting the number is as follows: The total yield of fusion gamma rays is

$$\frac{kc\lambda_e}{\lambda_o + \lambda_{pp} + c\lambda_e}$$

as can be seen considering the three available channels for a μp atom; muon decay, formation of (pμp) and formation μd. The multiplicative constant k is the gamma ray yield when c is large, (the saturation value of the yield). The derivative of this expression in the limit of low concentration is

$$\frac{k\lambda_e}{\lambda_o + \lambda_{pp}} .$$

It turns out that λ_{pp} is several times larger than λ_o so that the slope is in fact sensitive to λ_{pp}. In practice a great deal of experimental information is available (such as the time distribution at each value of c) and the parameters can be decoupled and determined independently. An additional important piece of information that can be extracted is the concentration of deuterium originally present in the hydrogen; on the basis of gamma ray yield this is determined to be less than one part per million.

The value of λ_{pp} which is obtained from analysis of the results of the fusion experiment[11] is $1.89 \times 10^6 \pm 0.4$ sec^{-1}. This corresponds to a partial lifetime of the μp atom of 0.53 μsec. As has been pointed out earlier, the capture rate of muons in the singlet μp system is only about 14% higher than the capture rate when they are bound in the ortho-(pμp) molecular ion; this, together with the fact that in the present experiment useful neutron data can be obtained only after about 1.2 μsec following the arrival time of the muon, implies that the muon capture rate as measured in the present experiment is quite insensitive to the value of λ_{pp}. Experiments using bubble chamber techniques record events occurring at any time with respect to the muon stopping time, and are therefore somewhat more dependent on a knowledge of this transfer rate.

IV. DESCRIPTION OF THE EXPERIMENT

A. The Meson Beam and the Geometrical Arrangement

A magnetic field-free channel placed in the cyclotron fringe field permitted the extraction of a lower energy muon beam than would otherwise be possible. A 128 MeV/c muon beam was bent through 41° by a wedge shaped dipole magnet. The beam then passed through a pair of quadrupole magnets which were set so as to maximize the counting rate in the beam counter telescope; this condition corresponds to bringing the beam to a focus within the hydrogen target (see Fig. 5).

Beryllium moderator was used to reduce the muon energy from the initial 60 MeV to the appropriate energy which would allow muons to stop between the neutron detectors at the center of the target (see Figs. 4, 8). Beryllium was chosen as the optimum material for reducing multiple scattering of the beam. It was required that muons of 26 MeV impinge on the window of the target; the 24.5 MeV muons then entering the hydrogen would come to rest at the proper position. The differential stopping distribution of the muons was measured as a function of the amount of moderator placed in the beam. The approximately correct amount of moderator was chosen and was then varied slightly while muon decay electrons were counted; the final working conditions were chosen to be those which maximized the countring rate of decay electrons in the electron telescope. Differential and integral stopping distributions as well as the decay electron counting rate are shown as a function of moderator thickness in Figs. 9 and 10.

The differential range distribution of the muon beam as it appears in Fig. 9 has a full width at half maximum of 3.15 grams of carbon. This width is due to the momentum selection properties of the magnet and beam channel; interpreted in this way the beam is seen to have a momentum dispersion of ± 5 MeV/c or ± 3.8%. At the energies of interest hydrogen has a stopping power 2.35 times greater than has carbon. The 3-gram full width as measured with carbon then translates into 7.3 in. of liquid hydrogen. The neutron detectors are each 6 in. long in the direction of the target axis so that most of the muons are expected to stop directly in front of them. Beam distribution studies in a styrofoam dummy target which simulates the stopping power of liquid hydrogen confirm the expected stopping pattern (see Appendix II). The range distribution as measured with decay electrons is, of course, broader since the detectors subtend a large solid angle even when the beam stopping point has shifted slightly; as a result the counting rate of electrons and neutrons is less sensitive to small changes in beam momentum than might otherwise be expected. On the other hand small momentum shifts in the beam are likely to be accompanied by changes in beam purity and hence in the accidental events rate. For this reason the bending magnet current was continually monitored on a chart recorder during the run. The apparent shift between the peak of the electron curve and the half height point of the integral stopping curve in Fig. 10 represents the thickness of the hydrogen between the beam counters #3 and the projected center of the decay electron telescope.

Two different beam collimator arrangements were used during two successive weeks of running the muon capture experiment. One was characterized by an aperture 4 in. in diameter, the other by a 3 in. opening; although the latter reduced the number of muons entering the target, a somewhat improved ratio of wall stopping muons to hydrogen stopping muons was observed. The data from these two independent runs were analyzed separately and showed no significant difference; this is strong confirmation that correct account was made of phenomena relating to wall stoppings and wall penetration. The two geometrical arrangements are shown in Figs. 8a and 8b; they will be referred to as the "3 inch" and the "4 inch" conditions, respectively.

The meson beam telescope normally consisted of four plastic scintillation detectors each viewed by a photomultiplier. Two extra scintillation counters were inserted for special purposes; one to serve as the initial counter in a time-of-flight system, and the other to be in anti-coincidence with the beam telescope for differential range studies. Table III lists the detectors along with some of their properties.

Figures 5 and 8 show the locations of the beam detectors with respect to the shielding arrangement. Counter #1 was embedded in the front shielding wall but could be withdrawn from above to check line-up. It was thin to prevent beam scattering, a problem which rendered it impractical to employ the time-of-flight system as an added requirement during actual running. When the purified muon beam is used the pions are of

lower momentum than the muons which are accepted by the collimator system. They are, therefore, bent through a larger angle and most of them strike the shielding blocks or the sides of collimator walls. The location of counter #1 was chosen so as to intercept those pions which were likely to give rise to a detected neutron. These events were discarded, as shall be described, reducing the accidental neutron rate quite substantially.

Counters #3a and #3b were located adjacent to one another downstream of the moderator; the second of the two was extremely thin (0.02 in.) to reduce the number of muons stopping in plastic to a tolerable level. The two counters were placed in coincidence with one another so as to reduce the accidental counting rate in the beam telescope. An accidental coincidence in this case would very likely be due to a muon stopping in the beryllium moderator coincident with a noise pulse and would be electronically indistinguishable from a hydrogen stopping. Counter #3b consisted of a 20 mil sheet of plastic scintillator in a protective frame which supported a loose envelope of thin aluminum foil (to provide for light collection) and a 1 mil sheet of black mylar.

B. Electron and Neutron Detectors

The hydrogen target was surrounded by four $11\frac{1}{2}$" x 14" x 3/8" plastic scintillation counters; behind each of these was mounted a neutron detector surrounded by a least 2 in. of lead on five of its sides. The thin counters were used in coincidence with the neutron detectors to define electrons and in anti-coincidence

to select neutral particles. These counters were labeled A_1, A_2, A_3, and A_4 in a clockwise direction beginning at the upper right facing the beam; the respective neutron counters were called N_i. The anti-coincidence counters were constructed so as to form four sides of a box around the target; they subtended approximately 70% of the solid angle available to decay electrons from stopping muons. On the side facing the target each counter was covered only with 0.00075 in. of aluminum foil and 0.001 in. black mylar; these precautions were taken lest muons stop in low atomic number materials and be captured there. The anti-coincidence counters were used in four ways in the experimental logic: 1. As a prompt anti-coincidence at muon arrival time to warn of a muon having left the target and having penetrated the scintillator; 2. In coincidence with the neutron detectors to define electrons; 3. In prompt anti-coincidence with a pulse in the neutron detector to exclude electrons from consideration as events; 4. As a 10 μsec anti-coincidence (on film) to reduce accidental background.

The neutron detectors were made of liquid scintillator NE213 which was purified, deoxygenated and sealed in specially constructed glass vessels 6" x 5" x 4" in size. An EMI photo-multiplier, 9530B, directly viewed a 5" x 6" face of the rectangular volume. The 1.8 liter container was immersed in magnesium oxide powder inside a thin iron box; each of the four assembled counters was inserted into a lead well around the hydrogen target. The largest single source of counts in the

neutron counters are gamma rays due to bremsstrahlung of the muon decay electrons in their passage through the high Z target walls. In order to distinguish between neutron and gamma ray induced recoils in the detector, pulse shape analysis of the form developed by Brooks[25] was employed. The light produced by a chargedparticle in a scintillator is composed of a long lived (~ 300 nsec) component superposed on the more familiar 10 nsec initial pulse. The size of the slower component is always proportional to energy loss, while the fast pulse is linear only for minimum ionizing particles and saturates for particles with a high rate of energy loss $\frac{dE}{dx}$ such as 1-5 MeV protons. Thus, one can recognize neutrons and gamma rays by the ratio of the two components of the light pulse produced by the proton recoil or Compton recoil. Appendix I describes the saturation effect which enables particle discrimination and which also causes the non-linear energy response in the case of protons. The circuit in Fig. 11 was used to provide a particle discrimination pulse, derived from the slow component, which gated neutral events and was also displayed on an oscilloscope to be photographed and interpreted visually. Two pulses of opposite polarity are taken from the anode and dynode of the photomultiplier; the positive pulse enters a low pass filter to extract the fast component, it then discharges a capacitor which was charged to a negative voltage by the fast pulse from the anode. The system is balanced so that in the case of gamma rays there is very little residual voltage on the capacitor, while in the case of neutrons there is net

positive charge. The voltage at the capacitor is sensed by an emitter-follower and is then amplified and sent to a discriminator This residue pulse can be displayed as a function of particle energy by applying it and the fast component pulse to the horizontal and vertical deflection plates of a modified oscilloscope whose electron beam is unblanked only when the chosen logical requirements have been met (see Fig. 12). This sytem of display is useful in adjusting the pulse shape balance controls and the residue discriminator and for periodic checking of the particle discrimination quality.

The pulse shape discrimination circuit shown in Fig. 11 was located directly at the base of each neutron detector photomultiplier. The output amplification stage was not only necessary to provide enough gain to send the signal up to the counting area, but was biased so as to saturate on the unwanted initial negative spike and suppress it relative to the somewhat delayed neutron residue. The photomultiplier anode and dynode 11 supplied pulses to this circuit; dynodes 9 and 10 supplied fast pulses (actually the tube has a 25 nsec rise time) one of which went directly to the oscilloscopes for photographing and the other was further amplified and mixed with its sister pulses from the other three detectors. This mixed pulse then went to two pulse height discriminators; one served as a lower threshold, the other as an upper cutoff on neutron events (but not electrons). The upper discriminator which was set for about 15 MeV neutrons, eliminated high energy bremsstrahlung events whose slow residue might be sufficiently large to pass the residue

discriminator and be counted as neutrons. Discriminator settings and photomultiplier voltage stability were periodically checked by displaying the oscilloscope input pulse on a kicksorter which was gated by the logic output (discriminators, etc.). Such pulse height spectra (Fig. 24a) were also used to measure the intrinsic energy resolution of the detectors. With low energy gamma sources simulating proton recoils in a detector of the volume used (4" x 5" x 6") the resolution spread is almost entirely due to statistical fluctuations in the number of photoelectrons emitted at the tube photocathode. The resolution was taken to be $\pm$ 10% at 2.76 MeV (gamma ray energy) and proportional to $1/\sqrt{E}$. Figure 12 shows the energy versus residue plot of a Pu-Be source, showing separated neutron and gamma ray bands. Gamma ray sources are used to set the energy scale which is nonlinear for proton recoils. Calibration of the scale involved an independent experiment which is described in Appendix I. Neutron-gamma ray separation is possible only above some minimum energy depending on the light collection efficiency of the detector and other factors. Fluctuations in the number of photoelectrons received from the slow component, which contain less than one-third the total output charge, result in an inability to resolve the two bands when the light level is low.

C. Logic and Data Storage

Three types of coincidence circuits were used in the electronic logic of the muon capture experiment. Fast coincidences between pairs of beam counters were made in circuits of

the Franzini type[26] adjusted to have resolving times of about 10 nsec. The use of the improved duty-cycle and purified beam eliminated the need for ultra-fast circuitry while the duration of the run made it convenient to use broader resolving times which could tolerate small drifts in photomultiplier voltages, etc. Circuits of the type described by Fitch[27] were used with 30-60 nsec resolving times for making anticoincidences and coincidences between outputs of other circuits. The slow μsec logic needed for making delayed coincidences between muon pulses and electrons and neutrons employed a direct coupled system of modular gates and univibrators developed for general use in the laboratory.[28] Photomultiplier pulses were led from the detectors in the cyclotron experimental area to the laboratory counting area on 125 ohm (RG-63U) cable; pulses to the time-of-flight system, however, were sent via low loss styrofoam filled cable. Intercircuit connections were usually made with 50 ohm cable (RG-58) while long delays were achieved by reshaping the output of 1500 ohm delay line. Fast pulses destined for oscilloscope photography were delayed with RG-63U. Transistorized circuitry was used throughout except for high voltage power supplies and Hewlett-Packard distributed amplifiers used in mixing fast pulses. Figure 14 is a simplified block diagram of the logic. The following eleven logical combinations of detector outputs were formed and recorded on a set of scalers:

Time	a gated train of oscillator pulses
12	a coincidence between first two beam counters
123a3b	the muon beam
123a3b(ΣA_i)	muons not leaving target ="mu stop" = μ
(ΣN_i)(ΣA_i)	decay electrons = e_u
(ΣN_i)$\bar{e}_u$	neutral particles converting in the neutron detector = non-e
(non-e)(Res)	neutrons, (slow component residue is sufficiently large) = n
(mu)e_u	muon gated electrons, real and accidental = e_r, e_a(e_r - e_a = e)
(mu)n	gated neutrons = n_r, n_a = "events".

The notation (ΣA_i) or (ΣN_i) refers to the mixture of the four detector outputs. In addition to the requirements noted above, each "μ" signal had to pass the "beam gate"; that is, it was used only if it occurred during the 8 millisec when the meson beam was being ejected with good duty-cycle. The requirement, $n\bar{1}$, discarding events which are in coincidence with an incoming pion, was omitted from the logic but was enforced when the scanned oscilloscope photographs were analyzed. As will be seen later, there was often a delay between the detection of an incoming pion and the detection of the neutron due to the flight time of the neutron from the point at which it was produced upstream to the detector within the shielding house. A 5 MeV neutron takes 32 nsec to traverse a meter; so that while the

flight time is negligible for neutrons originating in the hydrogen target, it is not when the neutron is produced in the walls of a beam collimator early in the beam path.

To permit careful time and energy measurements as well as to check neutron-gamma ray discrimination and anticoincidence operation, several detector pulses were photographed. A sequence of mirrors was used to record simultaneously the traces of the Tektronix oscilloscopes 517 and 555 on film. Both the oscilloscopes and the film advance mechanism were triggered on the arrival of either an n_r or n_a signal; that is, a muon gated neutron that occurred during a 5 μsec interval beginning either 1/2 μsec after a muon pulse or 15 μsec thereafter. The former interval includes events from muon capture as well as some random background; the latter interval only yields background events since all captures and decays are assumed to have taken place before 15 μsec have elapsed. The background as measured in the second interval can be used to correct the number of events measured in the first interval, as the background is uncorrelated in time with individual muons.

Figure 15 shows typical oscilloscope traces. The "517" oscilloscope trace records the pulse from the neutron detector and a pulse from beam counter #1; these are used to determine whether a pion in the beam might have given rise to the neutron event. The other oscilloscope displays two traces, of which the lower is a record of the neutron detector output (the fast pulse amplitude and the slow residue) used to measure the

neutron energy and to perform neutron-gamma ray discrimination. The upper trace carries the neutron pulse again in attenuated form and a shaped "μ" pulse; it may also display pulses in the anticoincidence counters if there should be any. Near the end of the trace is a pulse whose length identifies one or another of the four neutron detectors as the source of the event.

Simultaneously with data being taken on film, a "digitron" system received pulses representing the muon and electron and stored their time interval distribution in the magnetic core memory of a 400 channel pulse height analyzer, making possible lifetime measurements of very high statistical accuracy.

D. Data Taking Procedure

Because of the low muon capture rate as compared with decay, only 10-20 events were expected per hour, necessitating a run of two weeks to collect sufficient data and to obtain accurate knowledge of the corrections. The "4 inch" geometrical arrangement (Fig. 8b) was used during the first week of running; under these conditions 400 muons per second stopped in hydrogen. Under "3 inch" (Fig. 8a) conditions used during the second week only 280 muons per second could be stopped in hydrogen. Frequent checks were made to ensure the constancy of certain ratios of counting rates, such as e/μ, 12/Time, $\mu/12$, e_a/e_r, etc. These ratios measure the beam purity, changes in the muon stopping distribution, vibrating target efficiency, and general stability of the apparatus. The response of the neutron detectors was periodically checked with a series of gamma ray sources whose energy was in the region of interest: Cs^{137} - 0.67 MeV,

Co^{60} - 1.25 MeV (the detectors are not able to resolve the two closely spaced lines), Na^{24} - 1.35 MeV and 2.76 MeV. The neutron-gamma ray discrimination quality was checked every few hours using a plutonium-beryllium source which emits neutrons of energy up to about 6 MeV and gamma rays of 4.4 MeV.

It was realized during an earlier version of the muon capture experiment that a significant source of background was produced by decay electron bremsstrahlung. Since the effect was electron associated, it was possible to measure it quite accurately by stopping positive muons in the target and looking for neutrons under exactly the same conditions as with the negative beam. It is rather easy to reverse the beam polarity, one has only to reverse the cyclotron magnetic field direction so that mesons of the opposite sign are extracted, the bending magnet and quadrupole magnet polarities are also reversed, but nothing in the geometrical arrangement has to be changed. Frequent alternations of beam polarity also made possible a very precise measurement of the positive and negative muon lifetime ratio confirming the prediction of particle-antiparticle lifetime equality by the TCP theorem. This will be the subject of a separate report.

Whenever data were being accumulated the count scalers and the oscilloscope system were stopped once per hour; the numbers of counts that were registered in each of the eleven channels were recorded and the scalers were reset to zero; a record was made of the film frame number so that a strict correlation

could be established between the photographed events and the scaler record. Three times each day radioactive sources were installed and the oscilloscope "events" trigger was simulated so that photographs could be taken of the neutron counter response to the various sources. Pictures were also taken of decay electron events by relaxing the anticoincidence requirement; these were useful in establishing the pulse size due to minimum ionizing particles in the anticoincidence counters.

V. DATA ANALYSIS

A. Film Scanning and Data Handling

During the course of the muon capture run, about 6000 ft of 35 mm film were used in photography of the oscilloscope traces. This included data taken with the positive and negative beam as well as radioactive source calibration pictures. The film was reprojected; pulse sizes and spacings were measured using a template and the measurements were punched on IBM cards, one card per frame. The following information was recorded: the film frame number, a code denoting the type of data, the number of the neutron detector responsible for the event, the size of the fast output pulse from the neutron detector, the size of the fast pulse which was attenuated by a factor of 4 (to increase the dynamic range of the oscilloscope), the size of the slow component residue, the time between the neutron pulse and the muon trigger, the time between the neutron pulse and anticoincidence counter pulse (if any), the time between the neutron pulse and the pulse from beam counter #1 (if any), and a code denoting whether the event occurred during the "real" gating interval or during the delayed "accidental" interval.

All of the above information except the counter #1 pulse and its time marker appeared on the two traces of the Tektronix 555 oscilloscope with a sweep speed of 1 μsec per centimeter (10 μsec full scale); the 517 oscilloscope displayed 1 μsec of time in the vicinity of the neutron pulse. From time to time segments of the film were rescanned to check scanning efficiency and accuracy; absolute time calibration was made possible by photographing a crystal controlled oscillator output and pulse trains of various amplitudes.

The data cards were sorted according to neutron detector number and the presence or absence of a "pion" pulse (counter #1) at the time of the neutron (or shortly before). The proper time interval to exclude was chosen on the basis of a distribution curve of pion-neutron time intervals plotted from the data. This plot also indicates the fraction of events that were needlessly excluded because of a random pulse in counter #1; these accidentals are taken into consideration in the analysis. The fast trace also pictures real events which occurred near the beginning of the gating interval and can be used to obtain a high resolution time interval distribution of the early neutrons which are largely from captures in the iron walls of the target. Since the gating interval does not begin until about 1/2 μsec after the muon stopping time, the captures in the very high Z materials such as zirconium and silver are not visible in the oscilloscope data; these capture events are clearly observed, however, in neutron time distribution data taken with the digitron. Early time data is used to obtain an accurate estimate

of the number of muons stopping in the target walls; this number while not interesting in itself is important in deducing the number of muons which penetrate the walls and stop in the lower Z coating of the anticoincidence detectors.

Events which contain evidence of a pulse in the anticoincidence counter are excluded for several reasons; a fraction of these events appeared only because the $N\bar{A}$ anticoincidence failed due to the small size of the pulse in the A counter, a fraction appeared because the (mu)$\bar{A}$ anticoincidence failed for the same reason, and finally, some events appeared because of an accidental (random) neutron pulse in conjunction with the actual decay electron of an actual muon. Thus the visual exclusion of events with A-pulses not only increases the efficiency of the electronic anticoincidences, but also eliminates a substantial fraction of random events with the aid of the very large solid angle of the A counters and the 10 μsec of time which are visible on the film. This requirement is analogous to the condition in a bubble chamber experiment that, if a muon is to be captured, there should at least be no decay electron track emerging from its stopping point.

For each individual neutron detector, for the data accumulated during each day of running, a plot was made of the size of the fast pulse in the neutron detector against the size of the slow residue. This plot is analogous to the type of oscilloscope display that was available during the run. An example of such a plot along with similar plots for radioactive sources is given in Fig. 12c, d. By studying these plots one could eliminate all events which fell in the region of gamma rays;

one could also determine, for each detector, the lowest energy that would permit reliable neutron-gamma ray discrimination. Events which passed the tests mentioned thus far could no longer be rejected on an individual basis; each one had the characteristics of muon capture in hydrogen. These events were stored on magnetic tape for subsequent handling on an IBM 1401 Data Processing System, they were still grouped according to neutron detector number and day of running; data from the 3 and 4 inch geometrical situations were kept separate throughout. Muon-neutron time distributions were plotted from these events. These are shown for the two geometries in Figs. 16a, 16b. They are characterized by an approximately 2.2 μsec lifetime component, as is expected from muon capture in hydrogen, and a 0.2 μsec component from iron captures. Accidental events whose time distribution is shown in Fig. 17 were subtracted from the lifetime plot. For both the 3 inch and 4 inch running conditions a time delay was chosen (using the lifetime plots) beyond which the effect of iron captures would be small but not necessarily negligible (since a sufficiently accurate correction is possible). The time distributions were fitted, by minimizing χ^2, by a function of essentially the form $N_1 \exp(-t/0.2) + N_2 \exp(-t/x)$ with N_1, N_2 and x as parameters. Actually the function was modified slightly to take into account the finite resolution of the grouped data. The results of this fit are:

	x(μsec)
3 Inch	2.13 ± 0.15
4 Inch	2.10 ± 0.12

The data from positive beam running were treated similarly, the time distributions are shown in Fig. 18. There is, of course, no short-lived component in the lifetime plot; the results are:

	x(μsec)
3 Inch	2.24 ± 0.17
4 Inch	2.21 ± 0.15

B. Calculation of Capture Rate

The experimental value of the muon capture rate is given by

$$\text{Rate} = \frac{N-c}{E \cdot SA \cdot T} \cdot \frac{1}{M} \cdot \lambda_o$$

where N is the number of detected neutrons, c represents neutrons due to sources other than hydrogen, E is detector efficiency, SA is detector solid angle, and M is the number of muons stopping in hydrogen, T is the time gating factor. Each of these factors will be considered in turn.

1. Muons Stopping in Hydrogen

One can arrive at the number of muons stopping in hydrogen from two directions; the number of (123a3b)$\bar{A}$ counts or the number of (e_r - e_a) decay electrons. Several corrections must be made to the raw number of beam counts to obtain a muon stopping number; these are due to muons stopping in the front wall of the target, the side walls and in the collimator before the target. Experimental runs with a dummy target (see Appendix II)

were carried out in order to measure the muon stopping distribution and to determine the percentage of "μ" counts which are muons entering the target region. It was found that only about three-quarters of the (123a3b)$\bar{A}$ triggers represent muons which leave the last collimator, the rest having trajectories which failed to enter the target. Because of this large loss factor, this method can only serve as a rough check and it was decided to determine the number of muons stopping in hydrogen solely from the number of detected decay electrons. This second method is more reliable in any case. The important advantages are: i) except for a small and known number of accidentals a (mu)e coincidence can only be a decay electron; ii) electrons are required to pass the same time gate as neutrons; iii) electrons are detected with the same neutron detectors (and hence almost the same solid angle) as are neutrons; iv) since the time gate is sufficiently delayed only decay electrons from muons stopping in hydrogen are counted. The number of muons stopping in hydrogen is given by

$$M = (e_r - e_a)/T \cdot SA \cdot L$$

where T is the time gate factor, SA is the solid angle for electron detection, and L is a loss factor for electrons due to target side walls.

Table IV lists the various factors; $(e_r - e_a)$ has been set equal to e. In the negative beam e_a/e_r is 1.5% and 2.1%, respectively, for the 3 and 4 inch geometries. The time factor was deduced from the lifetime plot (Fig. 16) assuming a decay lifetime of 2.2 μsec and remembering that the same muon-generated

univibrator output gates both electrons and neutrons (Fig. 14). The solid angle for detection of an electron assuming the known muon stopping distribution in hydrogen (see Appendix II) was calculated, using the same Monte Carlo code as was used for the neutron detector efficiency calculation (see Appendix III); a small correction was applied to account for edge effects in the neutron detector.

The electron loss factor, L, consists of several effects of which the biggest and most difficult to calculate is radiation in the high Z target walls. A fraction of the decay electrons whose spectrum extends up to 53 MeV will radiate sufficient energy that the remaining electron will not be energetic enough to penetrate the neutron detector, and will therefore not register as an NA coincidence. This effect was directly measured with the dummy target and simulated target walls; the ratio e/mu was recorded with the walls in place and with the walls removed, while the muons maintained the same stopping distribution in the styrofoam pseudohydrogen. It was found that 5% of the electrons were lost by this mechanism. If the energy threshold for electrons in the neutron detector is 0.6 MeV and account is taken of the intervening materials outside the target, then a plot of the decay electron energy spectrum indicates that another 5% of the electrons which are headed toward the detector fail to be counted. Thus a loss factor of 10% $\pm$ 5% is used to correct the observed number of electrons.

2. The Time Gate Factor

From the neutron time distribution plot a time interval was chosen which excluded most of the iron capture events, only the data within this new time interval was analyzed to extract the muon capture rate. Events occurring at earlier times were isolated and used to provide an energy spectrum of neutrons from muon capture in iron. The time intervals used are listed below:

Geometry	Start of Interval (μsec)	End of Interval (μsec)	Gate Factor (T)
3 Inch	1.2	5.2	0.486 ± 1%
4 Inch	1.3	5.1	0.456 ± 1%

3. Solid Angle and Detector Efficiency

The total solid angle for the four neutron detectors was calculated (Appendix III) to be 19.6% given the measured muon stopping distribution. The solid angle in this sense refers to the probability that isotropically directed particles emitted from the muon stopping point will enter the front face of the neutron detector. In the case of neutrons there are several other effects to consider: First, the neutron may be transmitted through the lead surrounding the detectors and enter from an unusual direction; this is particularly unlikely because the muon stopping distribution is peaked in front of the detectors. Second, a neutron has a substantial probability of traversing the entire neutron detector without inducing a proton recoil;

the detector thickness is somewhat less than one mean free path for a collision with the hydrogen in the scintillator volume so that some neutrons will go undetected. Third, even if a collision with a proton occurs, the recoil proton energy may be too small to produce a pulse that can pass the lower energy discriminator threshold.

A complete calculation of neutron detector efficiency was essential; the calculation would not have been difficult if it were not for several complicating conditions:

i) The neutron detectors were surrounded by lead and other materials which might "reflect" neutrons.

ii) The path length in the detector is direction dependent.

iii) Neutron cross sections are energy dependent.

iv) The detectors are thick enough to permit multiple recoils.

v) The hydrogen in the target itself is an excellent scatterer and degrader of neutrons.

vi) The response of the detectors is non-linear for protons of the relevant energies (<5.2 MeV).

vii) The detector contains carbon as well as hydrogen.

For these reasons a complete Monte Carlo calculation, including all of the above effects, was necessary. Appendix III describes the calculation which yielded a distribution of the number of events as a function of pulse height. In the limit of a thin, isolated, hydrogenous, linear detector this would simply be the proton single recoil energy spectrum which would in fact be a flat distribution extending from zero to the incident neutron energy.

Since the calculation gives the final expected yield as a single, but energy cut-off dependent, quantity it is not meaningful to decouple the several effects; but, because the electron yield depends on the solid angle also (which therefore "cancels out" in the final capture rate), it is interesting to list the extent to which each effect determines the final neutron yield. The numbers are approximate and are not needed in the analysis.

Fraction of Neutrons Observed due to Effect of:	
Solid angle	0.20
Hydrogen degradation	0.90
Detector mean free path	0.50
Energy cut-off (1 MeV)	0.36

The corrected observed neutron energy spectrum was computed as will be seen below and the calculated distribution was fitted to it, normalizing it to the total yield above a cut-off energy E_o. The efficiency for this value of E_o was then used to obtain the capture rate. Figure 19 shows the corrected neutron pulse height distributions together with the calculated pulse height spectrum for each of the detectors and each geometrical arrangement. After the expected spectrum was normalized χ^2 was calculated for each case. The errors used to calculate χ^2 are those shown on the graphs, they are a combination of statistical errors and propogation errors due to the subtractions.

4. The Corrected Number of Detected Neutrons

The data on gamma ray sources that were taken during each day of running were plotted and a scale factor (to convert the arbitrary units used in scanning to MeV) was found for each

neutron detector and for each day. The neutron events in the chosen time interval were converted to an MeV scale as were the accidental neutron events and the neutron events accumulated during positive beam running. For purposes of analysis the events were grouped into intervals of 0.2 MeV (as measured on a gamma ray scale). Several corrections were applied to the neutron events.

a) Accidentals: Random background events were accumulated by triggering on neutrons occurring during the 15 μsec delayed time gate. For the 3 and 4 in. geometries the accidental events rate was 0.39 and 0.49 counts per μsec per million muon stoppings, respectively. As has been pointed out, the accidental rate in the real gating interval was reduced by the requirement that no anticoincidence counter pulse (A-pulse) appear on the trace. The effect of this requirement was measured by considering the time distribution of A-pulses relative to neutron pulses and also with respect to muon pulses. A fraction of the A-pulses were correlated in time with neutron pulses, these represent $N\bar{A}$ failures; others appeared earlier in time than the muon pulse, these are random and a correction is to be applied for having discarded these few events; the rest, namely, those that appear after a muon but uncorrelated with a neutron, are the ones of interest here and represent reduction of accidentals.

The integral of the energy spectrum of accidental neutron events (Fig. 17) was corrected for the length of the "real" time interval and for the above reduction, and the normalized energy spectrum was subtracted point by point from that of the real neutron events.

b) Neutron Events in the Positive Beam: In order to evaluate possible spurious events due to the high flux of decay electrons entering the neutron detectors, it was desirable to count decay electrons in the absence of muon capture neutrons. This situation is readily obtainable by stopping positive muons in the hydrogen target. Positive muons have essentially no probability for nuclear interactions, but their decay electron energy spectrum and angular distribution are identical with those of negative muons. It was found that a non-negligible rate of neutron events persisted under positive beam running conditions. These events were found to have the time distribution of decay electrons and an explanation for them was found in photonuclear processes occurring in the neutron detectors.

The photonuclear reactions C^{12} (γ, n) C^{11} and $C^{12}(\gamma,p)$ B^{11} show large increases in cross section between 20 and 30 MeV, the region of the giant dipole resonance.[29,30,31] Somewhat less probable are similar reactions involving three particle final states. The photoproton reaction has a higher but narrower peak in its cross section than does the photoneutron reaction which reaches a maximum at 22 MeV and falls off slowly. Between zero and 50 MeV the average cross section for the two processes are approximately equal. The energy distribution of the proton peaks at 5.5 MeV and has a width at half maximum of 2.8 MeV. While it is difficult to estimate the number and energy spectrum of gamma rays from electron bremsstrahlung that are available, the observed rate of neutron events in the positive beam is roughly consistent with photonuclear processes occurring in the thick neutron detectors.

The possibility of stopping positive muons in the hydrogen, where the physical situation is identical except for the absence of capture neutrons, allows an accurate correction to the data independent of knowledge of the source of events. A further confirmation of the legitimacy of the method of correction is obtained by considering the neutron events in the energy spectrum which lie above the muon capture cut-off energy. Such events in the spectrum obtained from the negative beam are exactly subtracted by similar events in the positive beam data; it follows that the subtraction at lower energies must also be of the correct size.

That the positive beam neutron events are electron associated is further confirmed by the time distribution of these events which can be seen in Fig. 18 to be a 2.2 μsec exponential. The neutron events were subdivided into the usual 0.2 MeV intervals and were corrected for positive beam accidentals; they were then normalized to take into account the number of decay electrons counted during negative beam running and to take into consideration differences in the gating time and were subtracted point by point from the neutron events accumulated during the negative beam experiment. The approximate rate of positive beam events is one event per 10,000 detected decay electrons, where an event is defined as a proton recoil of between 1 and 9 MeV. The rate within the energy interval of interest is of course lower.

c) Wall Capture Events: The neutron time distribution reveals a contribution from muon capture in iron; it will be shown later that there is no reason to expect a substantial contribution from any material other than iron. The energy spectrum of neutrons from muon capture in iron was determined in two ways. In a preliminary measurement a study was made of the neutron yields and spectra from muon capture in various materials including carbon, iron, silver, zirconium and lead. Figure 20 shows the spectra obtained from these materials using a neutron detector and muon beam similar to the ones used for the principal experiment. An additional determination of the iron spectrum was obtained by considering only the early time segment of the actual data and subtracting from this the appropriate number of accidentals and of events with 2.2 μsec lifetime. The energy distribution so obtained is shown in Fig. 21; it is fitted by an exponential distribution as would be expected for an evaporation source but is even more closely approximated by an exponential at low energies and a slowly decreasing function at the upper end. This shape is expected on the basis of models of muon capture in heavy nuclei. The neutron yield from iron was normalized to the number obtained from the time distribution and the gating interval location and was subtracted from the neutron events spectrum. The gating interval was chosen so as to keep the subtraction small; iron events would soon overwhelm the data at earlier times and the subtraction is insufficiently reliable.

d) Scanning and Statistical Corrections: The maximum film advance rate in the oscilloscope photography system was 1 frame per second. It was considered undesirable to employ a blocking time of this magnitude for the oscilloscope trigger since this would make it impossible to count directly those events which fell within the dead time. Instead, during film scanning an IBM card record was made of events which overlapped and which were unmeasurable.

The number of neutron events were corrected for the number of events lost because of confusing overlap of pulses on the trace and because of superimposed traces; correction was also made in the categories of accidentals and positive beam events. The percentage correction that was applied, together with its uncertainty, is tabulated below for each type of loss.

	3 In.	4 In.
Events with 2 mu pulses	2.1% ± 0.2%	4.5% ± 0.3%
Events with 2 neutron pulses	6.2% ± 0.3%	9.6% ± 0.3%
Superposed frames	2.2% ± 0.2%	4.8% ± 0.3%
Accidental pion pulse	2.0% ± 0.4%	1.6% ± 0.3%
Accidental electron pulse	0.5% ± 0.1%	0.8% ± 0.1%
Total Correction	13.0% ± 0.6%	21.3% ± 0.6%

This correction contributes only a negligible error to the final result by virtue of a complete tabulation and record of lost events.

The scanning efficiency demands no correction since essentially every film frame was accounted for on an IBM card, and rejection of events took place during analysis of the cards.

Electronic dead times are all too short to have an appreciable effect on the rate of "events" triggers and, since detector pulses are displayed directly, can have no effect on the pulses appearing on the traces.

The neutron pulse height spectrum was plotted for each detector in each geometrical arrangement. Detector N_3 was eliminated from detailed consideration early in the analysis since the quality of neutron-gamma ray discrimination was doubtful for a large fraction of the data. The calculated detector response was fitted to each energy spectrum by equalizing the areas above some chosen energy (on the gamma ray scale); no scale change or other adjustment was needed beyond the original conversion of arbitrary pulse height units to energy (MeV) using source data. Figure 19 shows the six plots along with the χ^2 calculated after the expected curve was fitted.

For purposes of presentation and to calculate the capture rate the neutron data, as well as the corrections, were grouped into two energy blocks, one beginning at a low energy depending on the detector and ending at 2.8 MeV (corresponding to 5.8 MeV proton recoils), and the other entirely above the expected neutron energy from 3.2 to 4.2 MeV (gamma scale). The data in the first block was used to obtain the capture rate as in Table V, while the second block in Table VI demonstrates the cancellation of events above the expected energy.

5. Small Modifications to the Capture Rate

a) The presence of deuterium in the hydrogen: The fraction of muons being transferred to the deuterium branch of the diagram in Fig. 1 is

$$F = \frac{c\lambda_e}{\lambda_{pp} + \lambda_o + c\lambda_e}$$

the concentration of deuterium in the target is less than one part per million. Assume the measured values for the constants

$$\lambda_o = 0.455 \times 10^6 \text{ sec}^{-1}$$

$$\lambda_e = 1.400 \times 10^{10} \text{ sec}^{-1}$$

$$\lambda_{pp} = 1.900 \times 10^6 \text{ sec}^{-1}$$

then $F = 0.007$.

Actually, not all the muons which transfer to deuterium fail to give a measured neutron; in any case the effect of deuterium is negligible.

b) Other impurities in the hydrogen: Assume a transfer rate to higher atomic number impurities equal to 5×10^{10} sec^{-1}; the concentration of these impurities is $\sim 10^{-12}$, certainly less than 10^{-9}. In this case $F = 25 \times 10^{-6}$, but the capture rate is higher than that of hydrogen by ~ 200; then the fraction of neutrons from capture in these impurities is 0.005 at most; again negligible.

c) Captures in carbon (outside the target): There are only three possible sources of carbon capture; great efforts were made in the construction of the target to eliminate all low Z material, and plastic scintillator was the only remaining potentially dangerous material.

i) Muons stopping in counter #3a: The accidental rate of the (123a)3b coincidence is 10 per minute. These accidentals could very likely represent stoppings in the #3a counter. Including the ratio of solid angles of this detector to the hydrogen (0.06) and the ratio of capture rates (100), the fractional yield due to this mechanism is 2.5×10^{-3}; this is completely negligible

ii) Muons stopping in counter #3b: The differential stopping distribution curve for muons (Fig. 9) indicates that in the vicinity of counter #3b the stopping rate is 500 per gram, while in the peak of the distribution the rate is 3000 per gram. The counter is 0.05 grams thick so that the ratio of muons stopping in the counter to those stopping in hydrogen is 0.002. The ratio of solid angles is 0.07, the extra length of hydrogen causes further attenuation of the neutron yield by about a factor of 2, so the percentage neutron yield from this source is 0.7%.

iii) Muons penetrating the anticoincidence detectors: This case is an important one to study carefully since the solid angle for detection of any neutrons produced in the anticoincidence detectors is not smaller than that for hydrogen neutrons. It will be possible to obtain a sufficiently accurate estimate of this source of background by considering the number of muons stopping in the target walls. The latter number can be obtained in the following ways: First, the iron in the target wall comprises 0.495 grams while the higher Z components together comprise 2.69 grams (with an average Z of 42).

Analysis of the neutron data taken on film gives the following result for the ratio of muons stopping in iron to those stopping in hydrogen:

4 Inch geometry	0.78% ± 0.11
3 Inch geometry	0.55% ± 0.08.

The neutron time distributions as recorded on the digitron clearly show both a high Z component and an iron component in the lifetime. From this data one can obtain, independently of solid angle and efficiency, the ratio of muon stoppings in high Z to the stoppings in iron:

4 Inch	3.6 ± 0.4
3 Inch	6.1 ± 0.6

while the ratio of densities is 5.45. One then has for the percentage of muons stopping in the higher Z component of the walls:

4 Inch	2.8% ± 0.7
3 Inch	3.4% ± 0.8

Second, an independent estimate of the number of muons stopping in high Z materials comes from a comparison of the yield of decay electrons per muon in the positive and negative beams; from this source one obtains:

4 Inch	5.5% ± 2.2
3 Inch	3.5% ± 1.4

This is in rough agreement with the previous estimate. Analysis of the time distribution of decay electrons at early times shows an apparent 11% stopping in high Z component; however, this number should be reduced by a factor of 2 or 3 because it includes neutrons which have scattered in both the anti-coincidence detector and the neutron detector thus simulating electrons; this is important in the case of high Z materials only since there are twenty times as many neutrons as electrons per muon stopping.

The above determinations of wall stopping yield a stopping ratefor muons in the vicinity of the target walls of 1.4% of the muons per gram of wall material. Since muons are at the end of their range having penetrated much hydrogen, etc., the rate of stopping is surely decreasing with increasing thickness and, therefore, is expected to be somewhat lower than 1.4% at the position of the anticoincidence detector; nevertheless, this number will be used to obtain an upper limit. A further check on the above estimate is the observation that the electronic requirement (123a3b)$\bar{A}$ reduces the counted number of muons by (1 ± 0.3)% below the (123a3b) rate; since the anticoincidence detector is 1 gram thick, the estimate of muons penetrating it is verified.

Analysis of film taken of decay electron events shows that one can easily measure pulses whose size is one-fifth the size of the pulse due to a minimum ionizing particle passing through the detector (Fig. 22). For the anticoincidence detectors of the thickness used, one-fifth minimum ionizing corresponds to an energy loss of 0.5 MeV. A stopping muon which leaves 0.5 MeV in the plastic comes to rest after 0.0035 grams. The mylar and aluminum coating on the counters are 0.007 grams thick. Assuming a total low Z thickness of 0.011 grams wherein a stopping muon would go undetected, one has a ratio of carbon stopping muons to muons stopping in hydrogen 1.5×10^{-4}. Including a solid angle enhancement factor and a capture rate factor, we have as an upper limit on

the neutron yield ratio 1.8%. A more realistic estimate is probably 1%. Although it is much smaller than the quoted error, it is included as a correction factor: $(-1 \pm 0.5)\%$.

d) The admixture of (μp) atomic capture in the data: The (μp) atomic system converts to the $(p\mu p)$ molecular ion with a rate $\lambda_{pp} = 1.9 \times 10^6$ sec^{-1} or a partial lifetime of about 0.5 μsec. The data that were used in the analysis were taken in a time interval beginning at 1.2 μsec so that the admixture of (μp) is quite small; nevertheless, it is easy to calculate the exact effect on the capture rate. Using the usual coupling constants, the capture rate in the molecular state is expected to be 560 sec^{-1} while the singlet atomic capture rate is about 640 sec^{-1}. The rate in a mixture of the two which is observed from $t = t_o$ to infinity is:

$$R = \lambda_{(p\mu p)} + \frac{\lambda_o}{\lambda_o + \lambda_{pp}} \left[\lambda_{(\mu p)} - \lambda_{(p\mu p)}\right] e^{-(\lambda_{pp}) t_o}$$

t_o (μsec)	$\lambda_{(\mu p)}$	$\lambda_{(p\mu p)}$	R
0.0	640	560	580
1.2	640	560	562

In the present experiment the effect is very small but in a bubble chamber experiment ($t_o = 0$) the rate is expected to be higher by about 4%. Of course, such a correction presupposes knowledge of the actual rate.

e) Possible molecular ortho-para conversion: The rate of transition of the ortho state to the para is expected to be quite negligible on the scale of muon lifetimes.[12] One can obtain an upper limit to the decay rate from the neutron-muon time interval distribution curves (Fig. 16) by noting that the capture rate in the para state is expected to be about 220 sec^{-1} as opposed to 560 sec^{-1} in the ortho molecular state. The experimental upper limit to the ortho-para conversion rate λ_{op} is then 0.05×10^6 sec^{-1}, corresponding to a partial lifetime of 20 μsec. In the unlikely circumstance that this were in fact the conversion rate the apparent capture rate would be reduced to about 525 sec^{-1}.

6. Summary

The final estimate for the capture rate is 464 ± 42 sec^{-1}, a small correction has been applied for the effects mentioned in the last section. It can be seen (Table V) that the error is principally due to three sources: i) The various subtractions to the spectrum, ii) The number of muons stopping in the hydrogen, and iii) The detector efficiency calculation. The statistical error in the raw number of detected neutrons is rather small but the above three categories contribute roughly 4%, 5% and 5%, respectively.

Further improvement in the precision of such an experiment would clearly require reduction of uncertainties in a multitude of areas and is likely to be very difficult.

VI. PION CAPTURE: A CONFIRMING MEASUREMENT

A. Introduction

It is extremely desirable to apply the target, detector geometry, and efficiency calculation to a similar experiment which is somewhat easier to carry out and whose result is predictable. A natural choice for the check experiment is pion capture which proceeds by two almost equally likely modes. When a negative pion comes to rest in hydrogen it immediately interacts with a proton. Recent measurements[32] show that the time interval between a pion velocity of 0.006 C and nuclear interaction is about 2.3×10^{-12} sec in liquid hydrogen. No molecular effects take place in the case of pions. The interaction modes that occur are

(a) $\pi^- + p \rightarrow n + \pi^o$

(b) $\pi^- + p \rightarrow n + \gamma$

Mode (a) is inhibited by lack of phase space and by the s-state interaction to the point that mode (b) can compete with it. The neutron energy in mode (b) is 8.88 MeV while the one emitted in mode (a) has 0.4 MeV and is undetectable in this experiment. The Panofsky ratio which has been measured many times is defined as the ratio of probabilities $a/b = P$. The quantity measurable in this experiment is $b/(a + b) = R$. The expected value of R is then $R = 1/(1 + P) = 0.396$ using the recent value for P.[33]

B. Description of Experiment

The pion capture experiment can be performed with no change in the experimental arrangement other than that needed to stop a known number of pions in the target. This was accomplished by reverting to the normal unpurified meson beam situation and installing the time-of-flight system. The output of the time-to-height converter was sent to a pulse height window which selected pions in the beam; the signal from the window output was then put in coincidence with the usual "muon stopping" pulse, providing a trigger which was free of muons and, more important, of electrons. Since pion capture is a prompt process the muon triggered delayed gate was shortened in length and its delay was decreased so as to be in prompt coincidence with the pion stopping pulse (Fig. 23). Because of the relatively high "events" rate, it was possible to take data on a kicksorter as well as on film. On two occasions during the muon capture run the pion experiment was set up; the "real events" trigger gated a pulse height analyzer on which was displayed the neutron detector pulse height output. Data were recorded on film in exactly the same way as during the muon capture experiment; during scanning a prompt pion stopping pulse was required to identify an event.

Neutron-gamma ray discrimination was checked using the pion capture neutrons and gamma rays themselves, rather than a radioactive source, to ensure that the correct energy interval would be considered. Energy calibration was possible using the 4.4 MeV carbon gamma ray from a plutonium-beryllium source

(α + Be → n + C^* → C + γ) and the Na^{24} source for the lower end of the scale. The high energy point was fixed using the 6.14 MeV gamma ray from the following reaction: n + O^{16} → N^{16} + p, N^{16} → e^- + O^{16*} + $\bar{\nu}$, O^{16*} → O^{16} + γ (6.14 MeV). O^{16} (water) is irradiated inside the cyclotron shielding wall; since the beta decay has an 8 sec half-life, a high-speed pump is used to send the water out to the detector house and back.

There is such an abundance of pion capture neutrons that even if the detector energy response were unknown, it would be self-determining at the 8.9 MeV point. In fact, the high energy point obtained in this way helps to confirm the earlier independent measurement of the scintillator energy response (see Appendix I). Only a single neutron detector was used for the pion capture measurement in order to reduce the events rate to a tolerable level and to simplify the pulse height normalization problem on the kicksorter (Fig. 24).

C. Data and Results

To calculate the fraction of pions captured in the one observable mode it was necessary to obtain the actual number of pions stopping in hydrogen. Since the (123a3b) signal was gated on pions alone (on time-of-flight criterion) it was sufficient to apply the same factor (the ratio of muons stopping in hydrogen to beam counts) as was used in the muon experiment.

Only one correction to the neutron spectrum data was needed; it is expected that the same number of pions stop in wall materials as did muons in the principal experiment. However, wall captures here are coincident in time with pion arrival, as also are the captures in hydrogen. Thus wall captures play a

relatively larger role in pion capture where the device of delayed counting is not effective. A crude estimate of the number of neutrons expected from wall interactions was made and agrees with the actual correction which was performed in a self-determining manner. In the neutron energy spectrum plot a flat low level of counts persisted beyond the clearly visible cut-off energy of hydrogen events. The low background level was extrapolated back toward zero with the appropriate exponential-like rise. The total subtraction in the energy region of interest amounted to 12.8 ± 3%. The neutron energy distribution obtained from analysis of the film was plotted and fitted (by normalization only) with the calculated detector response curve (Fig. 25). Only a change in one parameter (the initial neutron energy) was needed to convert the Monte Carlo calculation of detector response from the muon capture to the pion capture situation. Table VII lists the data and results of three independent runs of the pion capture experiment.

TABLE VII

Calculation of Pion Capture Branching Fraction

Run	Detected Neutrons	Corrected Neutrons	Pion Stops(10^6)	Actual Neutrons(10^3)	Branching Fraction R
a	720	628±6.4%	0.192±5.5%	77.8±8.2%	0.405
b	1468	1280±5.4%	0.387	159.0±7.4%	0.411
c	685	597±7.3%	0.185	74.1±8.9%	0.401
				Average	0.407±0.035
				Expected	0.396

The error of the mean is 8.5%. The weighted average branching fraction is 0.407 ± 0.035. The branching fraction implied by the accepted value of the Panofsky ratio of 1.53 is 0.396. It should be pointed out that while the statistical errors are independent for the three runs, the errors assigned to the number of pion stoppings and to the efficiency calculation are not. This was taken into account in the calculation of the error of the mean.

The good agreement between the measured value of the branching fraction and the one expected on the basis of more precise experiments lends credibility to the assertion that in the muon capture experiment the muon stopping number and wall effect were assessed correctly, and that the detector efficiency calculation represented the physical situation to within the error assigned.

VII. RESULTS AND CONCLUSION

The present muon capture experiment yields a single experimentally determined number; the capture rate in the (pμp) molecular. If it were not for iron capture neutrons appearing at early times it would have been possible to extract a meaningful value for the (μp) atomic capture rate. An experiment free of high Z capture could, in principle, extract the triplet capture rate independently of efficiency and some backgrounds by observing the time variation of the capture rate at early times (assuming the singlet rate).

The corrected experimental result for the molecular capture rate is

$$464 \pm 42 \text{ sec}^{-1}.$$

In the basis of the best estimates for the coupling constants the expected molecular capture rate is

$$562 \pm 60 \text{ sec}^{-1},$$

where the error reflects the uncertainty in the molecular wave function as well as in the calculation of the capture rate (see p. 13).

There are several possible interpretations of a discrepancy between the observed and predicted rates.

i) The present value of the molecular wave function overlap could be in error by as much as 10%. A calculation with improved wave functions is now under way.[21]

ii) The equality of the electron and muon axial vector coupling constant is implied by the observation of the ratio of the reactions $\pi \rightarrow e + \nu$ and $\pi \rightarrow \mu + \nu$. At the momentum transfer of muon capture, the axial vector coupling constant is modified by a term of order (m_μ^2/M_p^2) which has a negligible effect on g_A. Anomalous behavior of the momentum dependence is possible but is considered unlikely.

iii) The conserved vector current theory identifies the momentum dependence of the vector coupling constant with that of the nucleon form factor. This identification allows the coupling constant g_V^μ to be evaluated at the muon capture momentum transfer. Effects of the conserved vector current have recently been clearly observed in the beta decay of the B^{12}-N^{12} multiplet.[34] Experiments on the decay $\pi^+ \rightarrow \pi^o + e^+ + \nu$ are in

progress, and some have already measured a rate in rough agreement with the prediction of the conserved vector current theory.[35] In view of the success of this hypothesis it is unlikely that either the vector coupling constant or the so-called weak magnetism terms (Eqs. 15 and 16, Sec. II) differ from the predicted values.

iv) It is conceivable that time reversal invariance fails in muon capture.[36] If this is the case, then the vector and axial vector coupling constants could have a relative phase factor (see Sec. II) and the capture rate in the singlet state is reduced below what would be expected if $g_V = -g_A$. In the vicinity of 180° the phase factor is quite insensitive to the measured capture rate since the rate is at a maximum there.

v) The calculation[18] of the induced pseudoscalar coupling g_p could be in error. The usual result is $g_p/g_A = 8$, but there are several indications that this is in disagreement with observation. The large angular asymmetry of neutrons observed in the capture of polarized muons by spin zero nuclei is consistent with a larger g_p/g_A ratio.[37] The recent observation[5c] of muon capture induced transitions in O^{16} is also consistent with a larger ratio but the interpretation depends on nuclear wave functions.

Using the expression for the muon capture rate (Eq. 23, Sec. II) with g_p/g_A and g_A/g_V as independent variables the molecular capture rate was computed. A band was plotted (see Fig. 26) in the plane of these variables that includes those points consistent with the results of the present experiment.

This experiment can be interpreted as providing a direct measurement of g_A/g_V assuming that g_V is given by beta decay experiments and the Conserved Vector Current theory. It can be seen that if the expected pseudoscalar term is retained then $g_A/g_V = -1.05 \pm 0.08$. But if the expected ratio of A to V is used, then a ratio of $g_p/g_A = 15.5 \pm 3.5$ is required in order to fit the data. In a hydrogen experiment the triplet capture rate is far more sensitive to the pseudoscalar term than is the molecular rate which is largely singlet.

It is clear that the experiments on muon capture that have been performed up to this time (see Table VIII) do not yield conclusive evidence for a universal V-A theory.

TABLE VIII

Muon Capture Results

Experiment	Result (sec^{-1})	Expected (sec^{-1})
Columbia [a]	515 ± 85	562
Chicago [b]	435 ± 100	580
CERN [c]	420 ± 75	580
This Experiment	464 ± 42	562

[a] See Ref. 7.

[b] See Ref. 22.

[c] See Ref. 23.

VIII. ACKNOWLEDGEMENTS

The experiment described in this report was performed in conjunction with L. M. Lederman, J. Rosen, S. Meyer, E. Bleser, W. Anderson and I-T. Wang. E. Zavattini participated in earlier stages of the experiment. The advice, guidance and encouragement of Professor Lederman throughout the course of the work are greatly appreciated.

We would like to thank Walter O. LeCroy for the design of the time-of-flight system and for continual assistance in instrumentation. Dr. M. Kalos assisted in the design and planning of the Monte Carlo efficiency calculation; conversations with him were very helpful. S. Meravy assisted in the construction of the hydrogen target; he was responsible for its trouble-free operation during the experimental run.

We are greatly indebted to Professor J. Rainwater for the use of the Nevis Neutron Velocity Selector facilities.

The experiment could not have been carried out were it not for the dedicated and continual assistance of the entire Nevis Laboratory staff.

APPENDIX I

Proton Response in NE 213

A. Introduction

When minimum ionizing particles, that is particles for which $\frac{dE}{dx}$ is independent of energy, traverse a scintillating material the light output per centimeter, $\frac{dS}{dr}$, is constant. One might expect that the generalization of the above observation to non-relativistic particles would be the following:

$$\frac{dS}{dr} = A \frac{dE}{dr} .$$

This is not the case however; the correct expression[39] is given by

$$\frac{dS}{dr} = \frac{a(dE/dr)}{1+b(dE/dr)} .$$

An oversimplified picture for the extra "saturation" term in the denominator requires the heavily ionizing particle to create around its path in matter a very densely ionized "column" in which recombination with subsequent light output is quenched by the strong local electric fields. The more heavily ionizing the particle the more severely quenched is the initial ($\sim$ 2 nsec) light output from the vicinity of the column. Recombination and de-excitation at later times ($\sim$ 100 nsec), characteristic of drift velocities and column diameter, always occur and are responsible for the slowly decaying component of light which remains linear with energy loss. Particle detection systems employing fast phototubes and high frequency components (distributed amplifiers, fast discriminators, oscilloscopes, etc.) are likely to be sensitive primarily to the fast nonlinear

component of light output. Therefore, the use of organic scintillators as energy spectrometers for heavy particles (e.g., protons) requires that the non-linearity of response of the scintillator be accurately known for the particle of interest. It has recently become clear that the scintillation efficiency or light output, at least in inorganic scintillators, depends on the mass of the particle as well as on dE/dx. This has been explained by considering the ionization produced by delta-rays which are able to escape from the primary column. In the case of heavy ions a substantial fraction of the total energy available goes into delta rays. Unfortunately no calculations are available at this time for organic liquids.

B. Description of Experiment

Experiments were carried out using the Nevis Neutron Velocity Selector to determine the response of the organic liquid scintillator, NE 213, to neutron induced proton recoils in the range 2 to 6 MeV. In this energy range, in a hydrogenous substance, ionization due to incident neutrons is entirely from elastic hydrogen collisions (at least at times short compared to thermalization time). The mean free path for 4 MeV neutrons in NE 213 (density = 0.88, composition = $CH_{1.2}$) is roughly 4 in. Thus, if one must measure the proton response function, a thin detector, in which multiple collision events are improbable, should be used; otherwise the observed response function contains an implicit dependence on detector geometry and initial neutron direction.

A glass cylinder 1/2 in. thick and 4 in. in diameter was filled with oxygen-free NE 213 and oriented coaxially with the neutron beam; it was viewed by a 5 in. phototube (EMI 9530 B) in direct contact with the 4 in. face. The detector was placed at the end of a helium pipe 100 meters from the source of a pulsed neutron beam. The beam is obtained by deflecting the cyclotron proton beam into a target once every cyclotron cycle (1/60 sec). The uncertainty in the initial time is at the very worst 4 proton rotation times, or about 200 nsec; at best it is one cycle, or 50 nsec. The use of "time-of-flight" techniques permits the convenient measurement of neutron energy and the elimination of gamma ray background. A similar experiment performed near the neutron target of a Van de Graaf generator, for example, would require efficient neutron-gamma ray discrimination and a knowledge of the discrimination efficiency as a function of energy. Pulses directly obtained from the phototube were displayed on an oscilloscope and photographed. The oscilloscope was triggered by the beam deflection pulse; neutron time of arrival was measured from the time of arrival of gamma rays. The pulse height output was calibrated using the Compton recoils from gamma ray sources of known energy, and checked with cosmic rays traversing the detector parallel to the cylinder axis (being minimum ionizing, they leave a calculable amount of energy in the detector).

C. Procedures

1) The sinusoidal output of a 5 Mc crystal controlled oscillator was displayed on the 1 μsec/cm. Tektronix 555 oscilloscope sweep and photographed to calibrate the sweep. A pulse train consisting of one fast pulse per μsec was photographed

to check that the vertical deflection sensitivity was not a function of horizontal position on the sweep; this was the case to better than 3%. These photographs were scanned under exactly the same conditions as the data, and thus furnished a check on the reprojection system and measuring technique.

2) With the detector in precisely the same position and attitude as during the data-taking run, it was exposed to the gamma radiation from Na^{24} source which was prepared by irradiating $Na^{23}Cl$ with a high flux of neutrons in the cyclotron. The gamma ray energies from this source are 1.38 MeV and 2.76 MeV. Several hundred Compton recoils were photographed and scanned, and a pulse height spectrum was plotted. The interpretation of the spectrum in a thin detector presents some difficulty since total absorption of energy is very unlikely. In fact, a single Compton collision is most probable and the upper end of the spectrum is the "Compton edge"; the secondary gamma ray is left with at least 0.2 MeV which might not be converted in the detector. As a check on the procedure for obtaining gamma ray energy points the pulse height spectrum from cosmic rays, which were selected by a coincidence requirement to be directed within 10° of the vertical, was displayed in a pulse height analyzer and compared with the spectrum from Na^{24}; the energy loss of the cosmic rays was calculated using the density of the scintillator, etc., and the point was located with respect to the spectrum of the source, providing an extra fiducial energy.

3) The tenth dynode of the photomultiplier was matched to 125 Ω cable through an emitter follower, the signal was led directly to the input preamplifier of the oscilloscope. No

intermediate circuitry was present to introduce non-linearities. The possibility of space charge saturation in the photomultiplier itself was avoided by studying the Na^{24} spectrum as a function of photomultiplier high voltage and observing that the relationship between the two "edges" of the spectrum as well as the shape at the upper end remained constant for at least 150 volts above the 1200 volts chosen as an operating point. These saturation tests were performed using a 400 channel RIDL pulse height analyzer of proven linearity. The gamma ray energies of the source encompass the neutron energy region of interest.

4) Data consisted of about 4000 photographs of the oscilloscope sweep showing about 6 μsec of time after gamma arrivals. On a second sweep the beam deflection trigger pulse was displayed but was used only as a trigger and as a crude reference point for the "zero-time" gamma pulse with respect to which neutron times were measured. Pictures were taken at the rate of 1 per second, a limitation of the camera film advance system. Source pictures were also taken at 1 per second selected at random from a much higher source rate. Sufficient D.C. current was available at the photomultiplier dynodes to ensure that there were no rate dependent effects on the pulse height.

The fundamental equation of the time-of-flight technique is $dE/E = -2\ dt/t$ so that is one wants 10% energy resolution at 5 MeV ($t = 3.2$ μsec) the time has to be measured to 5% or 0.16 μsec. By measuring pulse times on film, at the sweep speeds used, dt is about 0.05 μsec, so that the limitation in

neutron energy resolution is due to initial time jitter (0.2 μs) and the necessity of grouping data to improve statistics (from 0.35 MeV to 0.7 MeV, depending on energy).

D. Data Analysis

The scanning of the film yielded a time and pulse height coordinate for each neutron pulse recorded. The useful energy range was broken up into eight sub-intervals, and the pulse height spectrum in each of these was plotted.

The spectrum of proton recoils from a single hydrogen collision is $1/E_o \, dE$ for $E < E_o$. Since the light output is nonlinear with proton energy, there is a rise in the spectrum toward low energies. A very good approximation to the proton response function is

$$R(E) = AE + BE^2 \quad ,$$

at least below about 6 MeV. In the above equation E is the proton energy in MeV; the analagous response to electrons would be

$$R_e(E) = E \quad .$$

This means that a proton of energy E gives as much light as an electron of energy $(AE + BE^2)$. On the basis of this type of response, one can calculate the expected proton recoil spectrum shape in the approximation of a single collision. The universal spectrum for arbitrary initial neutron energy E_o is

$$\frac{1}{E_o} (A^2 + 4BE)^{-\frac{1}{2}} = N(E)$$

where the variable E is now the linear pulse height, or gamma ray energy. This function is plotted in Fig. 27a.

In conjunction with a Monte Carlo calculation of detector efficiencies the problem of a thin (1/2 in. thick) counter exposed to a parallel beam of 5 MeV neutrons was run. As expected the results indicated about 10% multiple collisions; the calculated and expected spectra are shown in Fig. 27. Reasonable assumptions were made about the response function; detector resolution was included in the next phase of the calculation. Thus in principle one can determine the response function by fitting the experimental points corresponding to a fixed neutron energy and determining the parameters A and B. Data of high statistical quality would be needed to obtain the parameters in this way. What is done in practice is to determine the end points of the spectra for each of the eight energy blocks separately, and to plot these against the incident neutron energies; this gives directly the parabolic response curve. This method is valid because above 2 or 3 MeV the recoil spectra are almost flat so that when resolution is folded in, as it already is in the experimental data, the position of the point at half height determines the end point very well. If more data were available a combination of both methods would increase the reliability of the low energy points. In that case one would also first "unfold" the resolution, which was hard to measure accurately in the detector used. Its excellent light collection and small volume made the resolution as measured with gamma rays different from that characteristic of proton recoils.

Figure 28 shows the response function obtained in this experiment as well as that used by Brooks.[25] These two agree within the errors of measurement. They are both in disagreement with response curve for NE 213 recently published;[39] that measurement used a cylindrical detector with the neutrons incident perpendicularly to the axis and viewed with a 6810A photomultiplier. The rise time of that tube is about 2 nsec while that of the 9530B is about 25 nsec but that difference should have little effect on the pulse height measured. That measurement is in the direction of decreased light output or increased saturation. It is known that the coefficient b in the equation

$$\frac{dS}{dr} = a(dE/dr)\left(1 + b\,\frac{dE}{dr}\right)^{-1}$$

increases as the amount of Terphenyl in the scintillator decreases. It may be that differences in composition account for the discrepancy.

Additional data of high statistical accuracy were obtained by gating the input to a pulse height analyzer and displaying the proton recoil spectrum. The delay of the narrow time gating pulse determined the neutron energy that was being analyzed; its width determined the energy resolution. A series of energy points up to about 6 MeV were analyzed; at each energy setting gamma ray sources were used to check the linearity of the gating system. An oscilloscope was used to monitor the time interval between the arrival of the gamma ray burst from the cyclotron and the position of the gating pulse which selects neutrons assuring accurate energy measurement. The response points obtained in this way are shown on the plot (Fig. 28) along with those obtained from analysis of the film.

E. Conclusion

The proton response curve obtained in this experiment agrees rather closely with that of Brooks[25]. A simple analytic fit to the curve is obtained by assuming a parabolic shape below 6 MeV and linear above that. The functions that were used were:

$$R = 0.28\,E + 0.033\,E^2 \qquad E < 6.\ \text{MeV}$$

$$R = 0.70\,E - 1.330 \qquad E > 6.\ \text{MeV}$$

The response curve determines the shape of the recoil spectrum in two principal ways; mainly it determines the upper energy fall-off point, that is, the response to a neutron which loses all its energy in a single collision; secondly it determines the curvature of the response spectrum near the low energy end. When fitting actual data the first characteristic is essentially self-calibrating, this means that even a small error in the end-point would result in a large deviation of the curve from the data. This statement is weakened somewhat by the finite resolution of the detectors, nevertheless a 5% error in the endpoint would be apparent. The second characteristic of the response curve causing the spectrum to rise near zero energy is difficult to measure, but if the data to be fitted do not extend down into the region where the response is rising sharply then the integrated yield is not sensitive to a precise knowledge of the energy scale in the low energy region. In the muon capture experiment the lower energy cut-off that was chosen did in fact eliminate the steeply rising part of the spectrum; it should be noted also that in the case of the hydrogen experiment part

of the spectrum increase near zero is due to neutron degradation in the hydrogen target, so that the actual shape is somewhat less sensitive to the response curve than normally. A second feature of the hydrogen experiment that affects the rise in the spectrum near zero is the necessity of subtracting iron events and accidental events from the neutron spectrum; both of these corrections are characterized by the fact that their spectrum increases sharply at low energies.

APPENDIX II

Measurement of Muon Stopping Distribution

Both the solid angle subtended by the neutron detectors and the counting efficiency for neutrons (due to hydrogen self-absorption) depend on the spatial distribution of muons that have come to rest in the hydrogen target. Upon the completion of the muon capture experiment, using the identical geometrical arrangement and beam, a study was made of the muon distribution to bring up to date preliminary measurements that had been made earlier.

A dummy target consisting of a detachable replica of the front target window, a replica of the side walls and a series of alternating layers of styrofoam and polystyrene (which simulated the stopping power of liquid hydrogen) took the place of the actual target. The pseudo-hydrogen could be inserted or removed in multiples of 1/2 in. thichnesses, so that the beam could be scanned at various positions along the target axis. Scanning was accomplished with a 1" x 1" plastic scintillator mounted on a 1" diameter RCA (6199) photomultiplier which was mounted on a delicately balanced engine. This allowed the detector to move in two directions perpendicular to the beam as well as along the beam axis. A 1/16 in. aluminum cap was provided to fit over the plastic scintillator; at each setting of the detector position the beam was counted with the cap alternately on and off to obtain the number of muons stopping per centimeter of hydrogen.

Horizontal and vertical scans were recorded with the detector at the front of the "target" and with the front window removed. The total number of mesons entering the target region was determined by computing

$$2\pi \int_0^R r\rho(r)dr$$

where $\rho(r)$ is the average radial distribution of the beam obtained from the two scans. This number was compared with the number of muon stopping signals as defined in Sec. V-B-1. The ratio of actual muons to "mu stops" in the 4 in. geometry was found to be 0.75 ± 0.05 which is in rough agreement with the ratio as determined from decay electrons (see Sec. V-B-1). The error due to the finite resolution of the scanning counter was estimated to be small (2%) compared to statistical errors.

Scans were performed at various axial positions (Z) in order to determine the radial distribution as a function of depth and to obtain the stopping distribution along the axis. In order to improve statistical accuracy it was necessary to use the total number of muons $[N(z) = 2\pi\int r\rho(r)dr]$ at each axial point; the distribution obtained in this way is then equivalent to the one obtained by range measurement.

The radial distributions obtained along the target axis are shown in Fig. 29. No differences in distribution were observed in the 3 in. and 4 in. geometrical situations. It is known that the number of wall stopping muons is different in the two cases (see Sec. V-B-5) but the statistical accuracy was insufficient, especially in the wings of the distribution, to determine that number from the scanning data.

For use in the neutron detector efficiency calculation several simplifying assumptions about the distributions were made. The spatial stopping distribution was taken as the product $F_1(r) \cdot F_2(z)$ and both functions were assumed to be gaussian. The standard deviations (σ_γ and σ_z) were obtained from the experimental curves and range curves: $\sigma_r = 2"$, $\sigma_z = 3.3"$.

APPENDIX III

Calculation of Detector Efficiency and Solid Angle

A Monte Carlo calculation designed to run on the IBM 7090 was performed in order to calculate the neutron detector efficiency. It traced neutron trajectories from their starting point in the hydrogen target through the walls and anticoincidence counter and into the neutron detector where proton recoils were tabulated to yield the detector response.

The geometrical features that were built into the calculation included the cylindrical hydrogen target, high Z target wall, anti-coincidence counter, neutron detector walls, neutron detector volume, lead shielding surrounding detectors and gaps where appropriate. To specify the geometry and to make the calculation manageable the entire domain was subdivided into 80 contiguous convex regions bounded by natural surfaces whenever possible. The material composition of each region was specified by the atomic weight of each component and by the atomic density of each. Neutron elastic and inelastic cross sections (supplied by NDA[40]) were tabulated at energy intervals of 0.05 MeV for all the relevant elements and were used to tabulate neutron mean free paths for each type of material present. Additional parameters were tabulated as a function of energy and material; these specified the probabilities of scattering on a given element within a material and the relative probability of inelastic and elastic collisions. It was assumed that when a neutron undergoes an inelastic collision it is lost.

The distribution of neutron starting points was taken to be the product of gaussians discussed in Appendix II; a gaussian distribution was simulated by noting that the average of a large number of independent randomly distributed numbers on a finite interval tends to a normal distribution. The starting neutrons were given a random direction in space and a specified initial energy. A random number was chosen according to an exponential distribution by a technique discussed by Von Neumann[41]; this number represented the number of mean free paths the neutron would traverse before undergoing a collision. The mean free path in the region was then compared with the distance to the region boundary along the direction of particle motion to determine whether the neutron was going to leave the region or suffer a collision. In the former case the new region to be entered was found and the process was repeated; in the later case the collision type was decided and the outgoing energy and direction were calculated. If the neutron energy were above a certain lower cutoff usually taken as 0.1 MeV, then the original process was repeated; if not, the total neutron detector response for the event was calculated and a new history was begun. When a hydrogen collision occurred in the neutron detector region the proton recoil energy as well as the neutron energy were recorded; at the end of a history when the neutron either fell below the cut-off energy or left the domain of interest, the responses to the proton recoils of that history were summed and the resulting response was tabulated. Knowledge of the

proton response function for the liquid scintillator used was needed to combine in a meaningful way the individual proton recoils of a given history. After a determined number of histories was completed a gaussian energy resolution was folded into the detector response. The gaussian width was taken to vary as $1/\sqrt{E}$ in accordance with the assumption that resolution broadening is due to statistical fluctuations in photo-electron number. Also tabulated were histories in which the neutron produced a proton recoil in the anticoincidence detector; these were subtracted from the final expected yield since they would be electronically rejected.

It was possible to improve the statistical accuracy of the Monte Carlo calculation of detector response by a device called "splitting". Since only about 20% of the starting neutrons were destined to enter the neutron detectors the remaining 80% of the histories in no way contribute to a knowledge of the actual response; they only serve, in a manner of speaking, to specify the solid angle and the interactions within the hydrogen target. It is wasteful to spend too great a fraction of the calculation time on those lost neutrons so when a neutron is about to enter the detector region 5 "latent neutrons" (for example) are produced with the energy and spatial properties of the parent neutron. These latent neutrons are followed in turn through the detector and any response that might occur is weighted by one-fifth when it is added to the total; thus improved statistics are obtained on the random

processes which take place in the detector. Neutrons which have entered the detector and which then leave are not split if they happen to return a second time.

The statistical accuracy of the calculation was estimated by tabulating results at the end of each of a series of short calculation runs (with independent random numbers) and using the fluctuation as a measure of the accuracy. The accuracy of the total yield is of course greater than the accuracy of the spectrum shape. The main calculation was performed with 15,000 starting neutrons; the statistical accuracy of the integrated yield was about 2%, which is smaller than the estimated error due to uncertainties in other calculational parameters.

The calculation was performed with several initial neutron energies from 2.5 MeV to 8.9 MeV in order to check behavior and for possible use in related experiments. The relative efficiency is plotted in Fig. 30 as a function of neutron starting energy and detector energy cut-off. The curve shapes are typical of those of similar detectors despite the presence of the hydrogen and the shielding materials.

The calculation was performed under a variety of conditions to test the effect of various features of the problem. Tests were made with various source distributions to check the sensitivity to error in the muon stopping distribution. It was found that if the width of the axial distribution is decreased by about 12%, then the yield changes by about 3%; the yield is about half as sensitive to increases in axial width. For a change in the radial width of about 20% the yield changed by

less than 2%. Uncertainty in measurement of the geometrical arrangement might account for 2% or 3% error; fortunately the symmetry of the detector locations results in some cancellation of position errors. Geometrical approximations have little effect.

Although the presence of the liquid hydrogen does not change the integrated neutron yield very much (about 10% reduction) it has an important effect on the neutron pulse height spectrum. Only about 45% of the neutrons leave the hydrogen unscattered; the remainder have an almost flat energy spectrum from zero to the maximum energy. Thus the original 5.2 MeV monochromatic neutron is badly degraded and there is a pile-up of events with small pulse heights many of which are lost below the lower energy threshold. The 8.9 MeV neutrons from pion capture are degraded to a lesser extent and their pulse height spectrum shows the characteristic plateau.

The calculated neutron pulse height spectrum was folded with several resolution functions; if the energy cut-off point is not too near the end of the spectrum different resolution widths have a negligible effect on the integrated yield.

The calculation that has been described was carried out on an IBM 7090 Digital Computer. The computer code was written in the form of a logical control program with sixteen smaller sub-programs to carry out specific calculations and routines. Most of the programs were written in the Fortran language but several frequently used segments involving random number calculations were coded in the computer language (FAP). The geome-

trical specifications and the element cross section tables were stored on magnetic tape; parameters such as initial energy, starting distribution widths, cut-off energy, total number of histories, etc. were specified each time the calculation was performed. While it was impossible to store the details of each history, tabulations of intermediate stages in the neutron history were available as were the neutron detector response without resolution broadening.

By letting the materials in all regions except the neutron detectors be replaced by vacuum one could approximate the solid angle subtended for the detection of decay electrons; in addition the tabulation of electron path lengths in traversing the neutron detectors gave an estimate for the edge effects in counting electrons. The mean depth of the neutron detector is about 3.4 in. for particles which enter the detector and which originated with the muon stopping distribution in the target; the most probable depth is about 4.6 in. These numbers indicate that the mean inclination for particles which enter the detector is about 30 deg from the perpendicular to the target axis and that the effective wall thickness is about 15% larger than the actual thickness.

The calculated solid angle for the four neutron detectors was 19.6%. The effective solid angle for electrons was taken to be 18.5%; the reduction was made to exclude electrons which traversed less than 1/2 cm of scintillator and, therefore, deposited less than 1 MeV of energy in the detector.

APPENDIX IV

Molecular Spin States

The (μp) atom is in a singlet state by the time it is likely to form a ($p\mu p$) molecule. It has been shown that it is most probable that an ortho molecule, with spin and orbital angular momentum equal to 1 is formed rather than the ground state para molecule. The ($p\mu p$) system then has the following properties:

Total angular momentum (j) = 1/2, 3/2

Proton spin (S_p) = 1

Total spin (S) = 1/2

It has been shown by calculation that there is no appreciable interaction between the total spin and the orbital angular momentum, and that the total spin is 1/2. Under these conditions one can calculate the relative amounts of (μp) singlet and triplet.

Consider the system of the three spins s_μ, s_p, and s_p and label them by j_1, j_2, and j_3. Define $j' = j_2 + j_3$ and $j'' = j_1 + j_2$, then the ortho molecular state is characterized by $j' = 1$ and it is desired to convert to the representation where j'' is either 0 or 1. A unitary transformation connects these representations[42]:

$$\Psi_{jm}(j') = \Sigma_{j''} R_{j''j'} \Psi_{jm}(j'')$$

where the R's are related to the Racah coefficients W as follows:

$$R_{j''j'} = [(2j'' + 1)(2j' + 1)]^{\frac{1}{2}} W(j_1 j_2 j j_3 ; j' j'')$$

$$j = j_1 + j_2 + j_3 \quad .$$

The coefficients needed are $W(\frac{1}{2}\frac{1}{2}\frac{1}{2}\frac{1}{2}; 10)$ and $W(\frac{1}{2}\frac{1}{2}\frac{1}{2}\frac{1}{2}; 11)$; these are tabulated and one ends with

$$(R_{01})^2 = 3/4 \quad \text{and} \quad (R_{11})^2 = 1/4$$

which are the relative weights of the two states. In the case of the para molecule $(R_{0j'})^2$ is given by $(2j' + 1)/4$. Then $(2j' + 1)/4 = 1/4$ or $3/4$ for the singlet and triplet states, respectively.

These results could actually have been obtained with more elementary techniques, but Racah coefficients furnish a natural means of changing representations when three spins are coupled.

REFERENCES

[1] R. P. Feynman and M. Gell-Mann, Phys. Rev. 109, 193 (1958).

[2] Ya. B. Zel'dovich and S. S. Gershtein, Usp. Fiz. Nauk 71, 581 (1960); (Translation: Soviet Physics Uspekhi 3, 593 (1961).

S. Cohen, D. L. Judd and R. J. Riddell, Jr., Phys. Rev. 119, 384 (1960).

[3] R. Klein and L. Wolfenstein, Phys. Rev. Letters 9, 408 (1962).

For a review of the experimental situation see V. L. Telegdi, Proceedings of the 1960 Annual International Conference on High Energy Physics at Rochester (Interscience Publishers, Inc. 1960) p. 713.

[4] L. Wolfenstein, Proceedings of the 1960 Annual International Conference on High Energy Physics at Rochester (Interscience Publishers, Inc. 1960) p. 529.

[5a] G. Culligan, J. F. Lathrop, V. L. Telegdi, R. Winston and R. A. Lundy, Phys. Rev. Letters 7,458 (1961); R. Winston, Phys. Rev. 129, 2766 (1963).

[5b] V. S. Evseev, V. S. Roganov, V. A. Chernogovova, M. M. Szymczak, Chang Run-Hwa, Proceedings of the 1962 Annual International Conference on High Energy Physics at GENEVA (CERN Scientific Information Service, Geneva, Switzerland, 1962) p. 425.

[5c] R. Cohen, S. Devons, A. Kanaris, Private communication.

[5d] O. A. Zaimidoroga, M. M. Kulyakin, B. Pontecorvo, R. M. Sulya'ev, A. I. Filippov, V. M. Tsupko-Sitnikov, Yu A. Scherbakov, JETP 41, 1805 (1961).

[6] R. H. Hildebrand, Phys. Rev. Letters 8, 34 (1962).

[7] E. Bleser, L. Lederman, J. Rosen, J. Rothberg and E. Zavattini, Phys. Rev. Letters 8, 288 (1962).

[8] H. Primakoff, Revs. Modern Phys. 31, 802 (1959).

[9] E. Fermi and E. Teller, Phys. Rev. 72, 399 (1947).

[10] E. Bleser, L. Lederman, J. Rosen, J. Rothberg and E. Zavattini, Phys. Rev. Letters 8, 128 (1962).

[11] E. Bleser, E. W. Anderson, L. Lederman, S. L. Meyer, J. Rosen, J. Rothberg and I-T. Wang (to be published).

[12] S. Weinberg, Phys. Rev. Letters 4, 585 (1960).

[13] A. Halpern and N. Kroll, private communication.

[14] S. L. Meyer, E. W. Anderson, E. Bleser, L. Lederman, J. Rosen, J. Rothberg and I-T. Wang, Bull. Am. Phys. Soc. 8, 34 (1963).

[15] A. Fujii and H. Primakoff, Nuovo cimento 12, 327 (1959).

[16] M. T. Burgy, V. E. Krohn, T. B. Novey, G. R. Ringo and V. L. Telegdi, Phys. Rev. 110, 1214 (1958).

[17] Lectures on Weak Interactions, C. Fronsdal, Editor (W. A. Benjamin, Inc., New York, New York, 1963).

[18] M. L. Goldberger and S. B. Treiman, Phys. Rev. 110, 1178 (1958). M. L. Goldberger and S. B. Treiman, Phys. Rev. 111, 354 (1958).

[19] R. K. Bardin, C. A. Barns, W. A. Fowler and P. A. Seeger, Phys. Rev. 127, 583 (1962).

[20] J. B. Adams, Phys. Rev. 126, 1567 (1962).

[21] A. Halpern, Private communication.

[22] R. H. Hildebrand and J. H. Doede, Proceedings of the 1962 Annual International Conference on High Energy Physics at Geneva (CERN Scientific Information Service, Geneva, Switzerland, 1962) p. 418.

[23] E. Bertolini, A. Citron, G. Gianlanella, S. Focardi, A. Mukhin, C. Rubbia, S. Saporetti, Proceedings of the 1962 Annual International Conference on High Energy Physics at Geneva (CERN Scientific Information Service, Geneva, Switzerland, 1962) p. 421.

[24] J. Rosen, Columbia University Nevis Report 92 (1960).

[25] F. D. Brooks, Progr. in Nuclear Phys. 5, 252 (1956); F. D. Brooks, Nuclear Instruments and Methods 4, 151 (1959).

[26] P. Franzini, Rev. Sci. Inst. 32, 1222 (1961).

[27] V. Fitch, Techniques of High Energy Physics, D. M. Ritson, Editor (Interscience Publishers, New York, N. Y. 1961).

[28] The analog time-to-height converter and the logic modules were designed by W. LeCroy.

[29] W. Barber, W. George and D. Reagan, Phys. Rev. 98, 73 (1955).

[30] W. E. Stephens and A. K. Mann, Bull. Am. Phys. Soc. 29, 26 (1954).

[31] J. Halpern and A. K. Mann, Phys. Rev. 83, 370 (1951).

[32] J. H. Doede, R. Hildebrand, M. H. Israel and M. R. Pyka, Phys. Rev. 129, 2808 (1963).

[33] J. Ryan, University of California Radiation Laboratory Report No. 9884 (1962).

[34] C. S. Wu, Y. K. Lee, L. Mo, Phys. Rev. Letters 10, 253 (1963).

[35] P. Depommier, J. Heintze, A. Mukhin, C. Rubbia, V. Soergel and K. Winter, Proceedings of the 1962 Annual International Conference on High Energy Physics at Geneva (CERN Scientific Information Service, Geneva, Switzerland, 1962) p. 411.

[36] G. Feinberg, Private communication.

[37] See Ref. 5b.

[38] J. B. Birks, Phys. Rev. 84, 364 (1951).

[39] R. Batchelor, W. B. Gilboy, J. B. Parker and J. H. Towle, Nuclear Instruments and Methods 13, 70 (1961).

[40] We are indebted to United Nuclear Corporation (Nuclear Development Associates) for their most recent neutron cross section data.

[41] J. Von Neumann, Monte Carlo Method (National Bureau of Standards, Washington, D. C., 1951).

[42] M. E. Rose, Elementary Theory of Angular Momentum (John Wiley and Sons, Inc., New York, New York, 1957).

TABLE II

Target Wall Composition

Material	Z	Side Wall		
		Thickness (in.)	Thickness (gm/cm^2)	Thickness in Radiation Length
Silver	47	0.020	0.535	0.060
Stainless Steel	26	0.025	0.495	0.033
Silver	47	0.020	0.535	0.060
Zirconium	40	0.100	1.620	0.155
Total			3.185	0.308
		Front Window		
Stainless Steel	26	0.013	0.258	0.017
Silver	47	0.001	0.027	0.003
Stainless Steel	26	0.010	0.198	0.013
Total			0.483	0.033

TABLE III

Properties of Beam Counters

Number	Photo-Multiplier	Size (in.)	Thickness (in.)	Purpose
0	56AVP	6 x 6	0.2500	Time-of-flight only
1	6810A	8 x 8	0.0625	Beam telescope
2	56AVP	6 x 6	0.3750	Time-of-flight and Beam
3a	6810A	5 x 5	0.0625	Beam telescope
3b	6810A	5 x 5	0.0200	Final Beam Counter
4	6810A	12 x 12	0.3750	Anticoincidence for Range Study Only

TABLE IV

Determination of Muon Stoppings

Geometry	$e(10^6)$	T	Ω	L	$M(10^6)$	M/N_μ	Obs. e/N_μ
3 In.	8.62	0.774	0.185	0.9	67.0	0.670	0.0863
4 In.	11.40	0.732	0.185	0.9	93.6	0.645	0.0786
Uncer-tainty	~ 0	±1.0%	±1.8%	±5.0%	±5.5%	±5.5%	±1.0%

TABLE V

Calculation of Capture Rate

Counter	4 In. Geometry N1	4 In. Geometry N2	4 In. Geometry N4	3 In. Geometry N1	3 In. Geometry N2	3 In. Geometry N4
Energy Interval (Mev)	0.8 to 2.8	1.0 to 2.8	1.4 to 2.8	1.2 to 2.8	1.0 to 2.8	1.2 to 2.8
Neutrons	547.0±26.2	441.5±23.1	264.4±17.7	288.2±18.1	340.1±19.5	227.2±16.3
Accidentals	39.0± 6.9	17.1± 4.6	9.0± 3.3	39.6± 6.7	19.2± 4.6	11.5± 3.4
Positive Beam Events	116.1±13.5	140.7±15.0	65.1±10.0	62.0± 8.6	48.8± 7.6	29.0± 5.9
Iron Captures	14.8± 4.2	9.9± 3.5	5.7± 2.6	8.0± 3.0	8.1± 3.0	5.8± 2.4
Corrected Events	377.1±30.4	273.8±28.1	184.6±20.9	178.6±21.5	264.0±21.8	180.9±17.9
Percentage Error	8.05%	10.3%	11.4%	12.0%	8.3%	9.9%
	rms Error	4.1%				
$(eff)^a \times (10^{+4})$	320.9(±5.0%)	274.6	181.2	227.8	274.6	227.8
eff x Ω	75.5(±5.4%)	74.1	46.0	51.5	73.3	59.5
$N_\mu' \times (10^{-6})$	43.2(±5.6%)	43.2	43.2	32.6	32.6	32.6
$(eff)(\Omega)(N_\mu')(10^3)$	326.0	320.0	198.5	167.8	238.0	194.0
$Rate^{-1}$ (N_μ/n)	865	1171	1072	940	902	1071
Rate (sec^{-1})	527±11.2%	388±13.0%	425±13.9%	485±14.4%	505±11.4%	425±12.7%
	wt. Av.	469 ± 9.0% = 469 ± 42				

[a] In the above Table "eff" is detector efficiency; "Ω" is individual solid angle for each detector determined from electrons; "N_μ'" is (N_μ) x (gate factor). The 6 values for the capture rate considered as a distribution about their mean have a χ^2 of 7.4. The final error of the mean includes contributions from the 6 independent errors as well as the errors in muon stopping rate and in detector efficiency which are the same for all 6 cases. The average capture rates in the 4 In. and 3 In. situations are 464.0 and 475.0, respectively.

TABLE VI

Calculation of Rate of Events above Muon Capture

Neutron Energy

Energy Interval - 3.2 - 4.2 MeV (gamma ray scale)

Neutron Counter	4 In. Geometry			3 In. Geometry		
	N1	N2	N4	N1	N2	N4
Neutrons	17.0 ± 4.6	12.1	17.0	18.1	15.9	13.6
Accidentals	2.9	1.7	1.2	2.2	2.8	0.9	0.0
Positive Beam Events	23.8	6.0	5.9	18.5	14.6	8.2	14.8
Iron Captures	1.0		0.6	0.8	1.0	0.7	1.0
Corrected Events	10.7 ± 7.8	4.4	-4.5	-0.3	6.1	-2.2
Average	-1.2 ± 3.0					

FIGURE CAPTIONS

Fig. 1 - A diagram showing the history of a muon after coming to rest in pure liquid hydrogen. λ_o is the free muon decay rate, λ_{cap} is the muon capture rate in the μp atom λ'_{cap} is the molecular capture rate. λ_{pp} is the molecular ion formation rate. When a small amount of deuterium is present (concentration c) then the process indicated by a dashed line can occur.

Fig. 2 - a) The four fermion interaction responsible for muon capture ignoring strong interactions.

b) An intermediate pion state diagram identified by the conserved vector current theory as due to a basic pion-lepton interaction.

c) The contribution to the "induced pseudo-scalar" term. Part of the diagram is responsible for pion decay.

d) A correction term to the axial vector current.

Fig. 3 - A diagram of the hydrogen target and associated purification system. The deuterium is used for the experiment that measures molecular constants.

Fig. 4 - The hydrogen target and some local shielding showing locations of detectors.

Fig. 5 - Cyclotron floor plan showing shielded "house" and beam detectors.

Fig. 6 - Differential beam stopping distributions in the normal mode of operation (114 MeV/c) and in the purified muon beam (132 MeV/c). The pion range is between 1 and 2 in. of carbon; the muon range is 3 to 4 in.

Fig. 7 - Pulse height distribution of time to height converter output. Beam particles traverse a 6 meter flight path. Lowest curve shows the unpurified beam with electrons on the left, muons, then pions. Upper curve is purified muon situation.

Fig. 8 - a) and b) Beam path before hydrogen target showing beam detectors, collimators, and moderator. The "3 in." and "4 in." geometries were used in successive weeks of running.

Fig. 9 - Stopping distribution of purified muon beam, showing number stopping per gram of carbon as a function of moderator thickness; and total number of stopping particles.

Fig. 10- Counting rate in decay electron telescope as beam stopping point is shifted within hydrogen target. Number of muons in beam telescope is shown also as a function of moderator thickness (in inches of carbon).

Fig. 11- Circuit used for neutron-gamma ray discrimination. Typical pulse shapes are shown; pulses due to gamma rays are shown as dashed where they differ from those due to neutrons.

Fig. 12- a) Photograph of live oscilloscope display of neutron or gamma ray pulse height versus slow component residue. Horizontal axis is energy, increasing toward the right. The neutron residue is displayed on the vertical axis increasing downward. Upper photograph shows gamma ray and neutron "bands" due to a Pu-Be source.

Lower picture is "band" due to pure gamma ray source (Cs^{137} - 0.67 MeV).

b) Neutron and gamma ray "bands" for a Pu-Be source. Lower picture shows effect of a residue discriminator used to select only neutrons.

c) and d) Plots of pulse height versus residue for neutron and gamma ray radioactive sources. Increasing energy is downward; neutron residue increases toward the right. The plots were generated from data taken from measurements of oscilloscope traces photographed during the experimental run. The numbers in the plot refer to the number of events in each "bin". Source types are indicated on each plot.

e) Plot of sample of raw neutron detector data taken during run.

Fig. 13 - Time distribution of neutron events shortly after muon stopping time, taken with 30 nsec/channel digitron. Early part of data is fitted with exponentials with decay times characteristic of Ag, Zr, and Fe capture.

Fig. 14 - Simplified block diagram of electronic logic used in muon capture in hydrogen experiment. The block marked "logic" refers to the μsec muon triggered gating system used to gate "real" and "accidental" neutrons and electrons.

Fig. 15 - Typical oscilloscope traces photographed during run.
a) and b) Upper trace (right to left) shows a neutron detector pulse (negative) and a muon stopping signal (positive) and the neutron detector identification pulse at the left. Center trace shows the neutron detector pulse used for energy measurement and the slow residue pulse used for particles discrimination. The lower trace (high sweep speed) shows the neutron pulse and would display pulse from detector #1 if it were present.
c) Upper trace shows an "accidental" neutron event due to a second beam particle present at the time of the neutron pulse. The fast trace therefore displays a pulse (positive) from #1.
d) A negative pulse from the anticoincidence detector is visible on the upper trace.

Fig. 16 - a) and b) Time distribution of neutrons from $\mu^- + p \rightarrow n + \nu$. Time interval measurements were obtained from scanning of film; accidental events have been subtracted but iron capture neutrons are in evidence at early times. Figs. 16-a and 16-b are independent plots of "4 Inch" and "3 Inch" data, respectively.

Fig. 17 - a) Neutron pulse height distribution; all "accidental" events from two different neutron detectors.

Fig. 17 - b) Time distribution of all "accidental" events as measured on film. The distributions are flat (as they should be) except for statistical fluctuations.

Fig. 18 - a) and b) Time distribution of neutron events occurring during positive beam running. Data from "4 Inch" and "3 Inch" geometries are presented separately.
c) Pulse height distributions of neutron events recorded during positive beam running.

Fig. 19 - a), b), and c) Pulse height distribution of corrected neutron events from $\mu^- + p \rightarrow n + \nu$. Each neutron detector and each geometrical arrangement is plotted individually. The horizontal scale is in MeV as calibrated with gamma ray sources. The results of a Monte Carlo calculation of detector response are shown as a solid curve. It was fitted by normalization.

Fig. 20 - Pulse height distribution of neutrons from muon capture in carbon, iron, zirconium and silver. These curves were measured in an independent run. The horizontal scale is in MeV as calibrated with gamma ray sources. The vertical scale is arbitrary and does not reflect the yield factors for each of the elements. The yields and spectrum shapes shown here are not needed in the analysis of the data and were only used to estimate the effect of wall stopping muons.

Fig. 21 - Pulse height distribution of neutrons from muon capture in iron. These points were obtained from the "early time" part of the actual neutron data taken during the run. The dashed curve shows how poor a fit ($\chi^2 = 58.3$) is obtained if the iron neutrons are fitted with the expected distribution from hydrogen. A much better fit is obtained ($\chi^2 = 15.1$) if an exponential energy distribution is assumed $[N_o \exp(-E/0.9)]$.

Fig. 22 - The solid curve is the pulse height spectrum in the anticoincidence detectors due to decay electrons which trigger an (NA) coincidence. There are 210 decay electrons contained in this plot. The "broken" curve is the size distribution of pulses in the anticoincidence detectors observed on film during actual data taking. The electronic anticoincidence requirements are in effect. In the case of very small pulses the electronic anticoincidence fails and the pulses appear on the film. The pulses which fall below the main peak of the solid curve are decay electrons which appear on the film together with an "accidental" neutron event. The "broken" curve was obtained from data which corresponds to 1.2×10^6 detected decay electrons.

Fig. 23 - A simplified block diagram of the part of the electronic logic peculiar to the pion capture experiment (see Fig. 14 for notation and rest of logic). The

pulse height analyzer (PHA) shown was used to monitor pion beam purity. A second PHA was gated on "events" and displayed the neutron pulse height spectrum.

Fig. 24 - a) Gamma ray pulse height distributions as measured on a PHA used to set energy scale of neutron events. The sources are Na^{24} (2.76 MeV), C^{12} (4.4 MeV) and O^{16} (6.14 MeV).

b) Uncorrected pulse height distribution of neutron events from pion capture ($\pi^- + p \rightarrow n + \gamma$). This energy spectrum was taken on a PHA; it was not used in the final analysis except as a check.

Fig. 25 - Pulse height distribution of pion capture neutrons taken from analysis of oscilloscope photographs. The results of a Monte Carlo calculation of detector response are shown as a solid curve. The calculated response is fitted by normalization and χ^2 is computed afterwards.

Fig. 26 - Muon capture rates in the ($p\mu p$) molecular ion with the axial-vector coupling constant and the induced pseudo-scalar coupling constant as independent variables. The point marked with a capture rate of 560 sec^{-1} corresponds to the usual choice of coupling constants. The band indicates the region consistent with the results of the present experiment.

Fig. 27 - a) The universal single neutron collision energy response curve $(A^2 + 4BE)^{-\frac{1}{2}}$ showing spectrum rise at low energies due to non-linear detector response.

Horizontal scale is in MeV as calibrated with a gamma ray source.

b) Results of a Monte Carlo calculation for a thin neutron detector with incident 5 MeV neutrons compared with the theoretical response curve. Actual response measurements were also made with a thin detector. These fit the curve shown.

Fig. 28 - The pulse height response of scintillator NE213 to protons. Experimental points were obtained using the Nevis Neutron Velocity Selector (see text) and one point was obtained from pion capture measurements. The solid curves are those of Brooks and Batchelor. The dashed curve was the one used in the analysis.

Fig. 29 - Radial distribution of muon trajectories in the styrofoam dummy target at several positions along the target axis (Z).

Fig. 30 - Relative efficiency of the neutron detectors for neutrons originating within the hydrogen target. The relative efficiencies (as determined with a Monte Carlo calculation) are plotted as a function of starting neutron energy. The several curves show the effect of the different choices of a lower energy threshold (E_{co}). The curves are plotted for E_{co} = 0, 1/2, 1, and $1\frac{1}{2}$ MeV on a gamma ray scale.

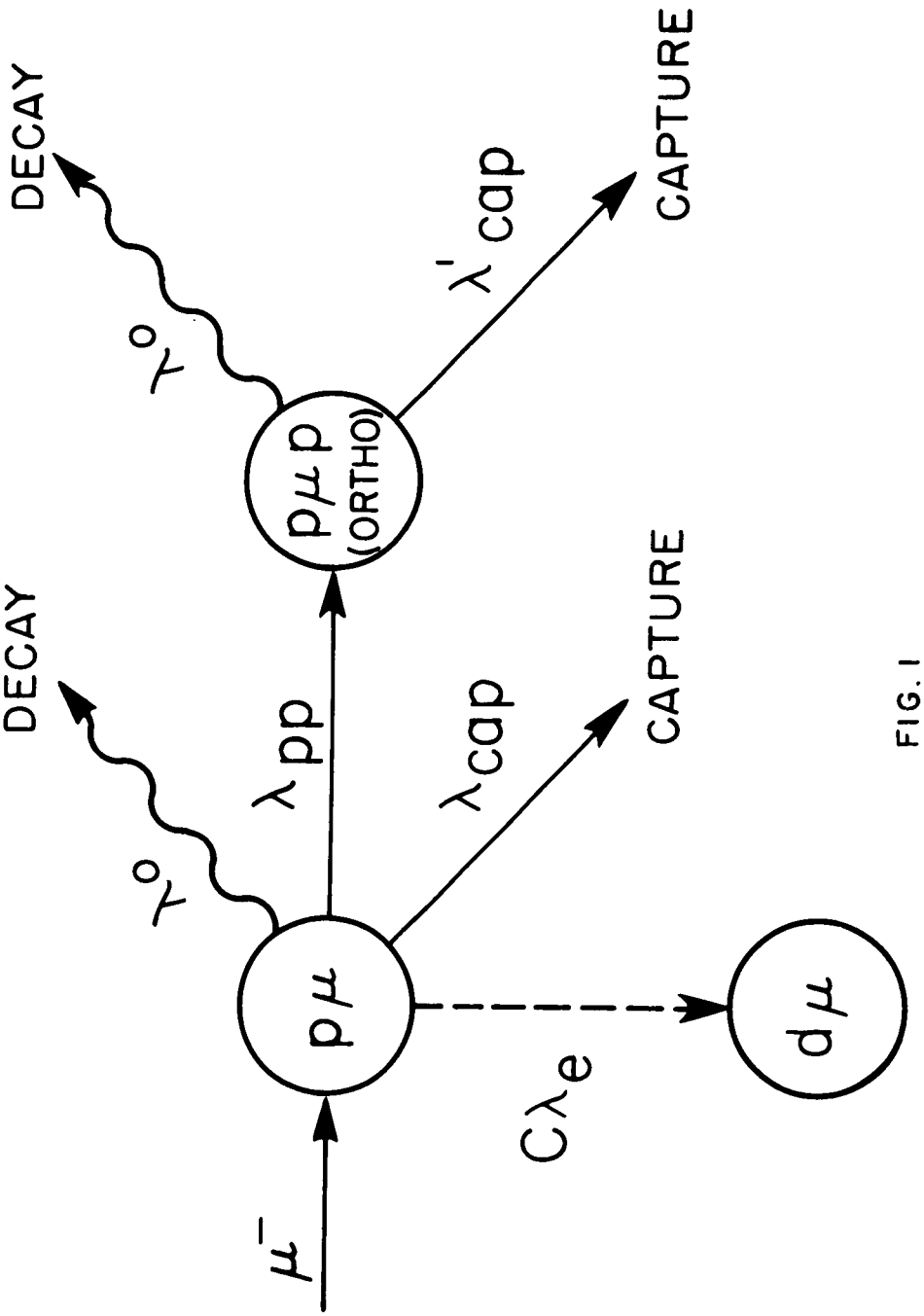
DECAY
γ^o
$p\mu p$ (ORTHO)
λ' cap
CAPTURE
DECAY
γ^o
λ pp
λcap
CAPTURE
$p\mu$
$C\lambda_e$
$d\mu$
μ^-

FIG. 1

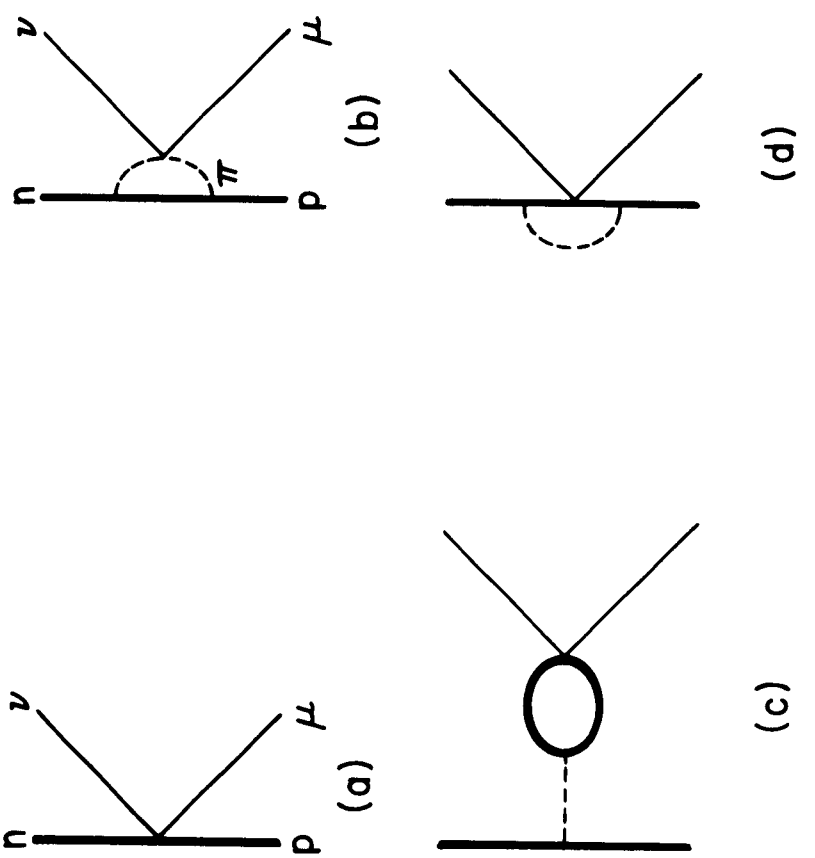

FIG. 2

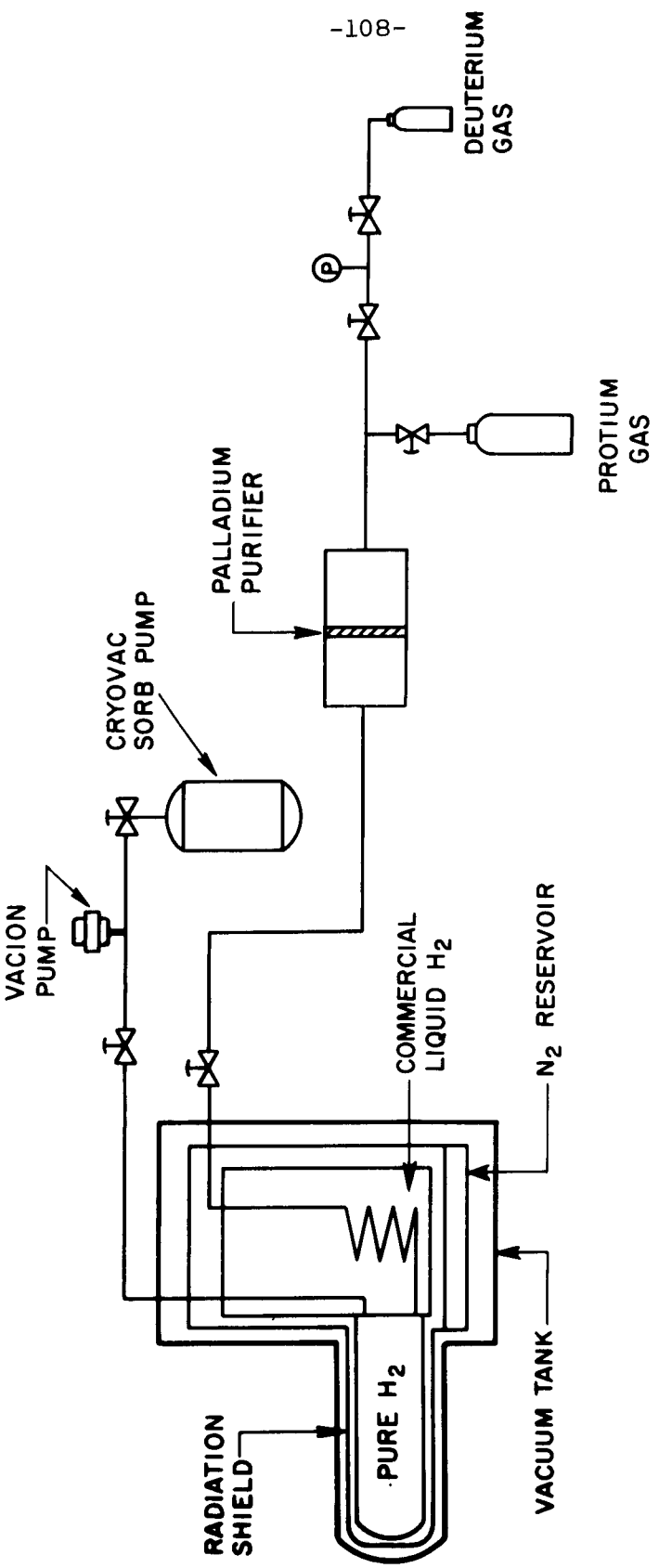
DEUTERIUM GAS
PROTIUM GAS
PALLADIUM PURIFIER
CRYOVAC SORB PUMP
VACION PUMP
COMMERCIAL LIQUID H_2
N_2 RESERVOIR
PURE H_2
RADIATION SHIELD
VACUUM TANK

FIG. 3

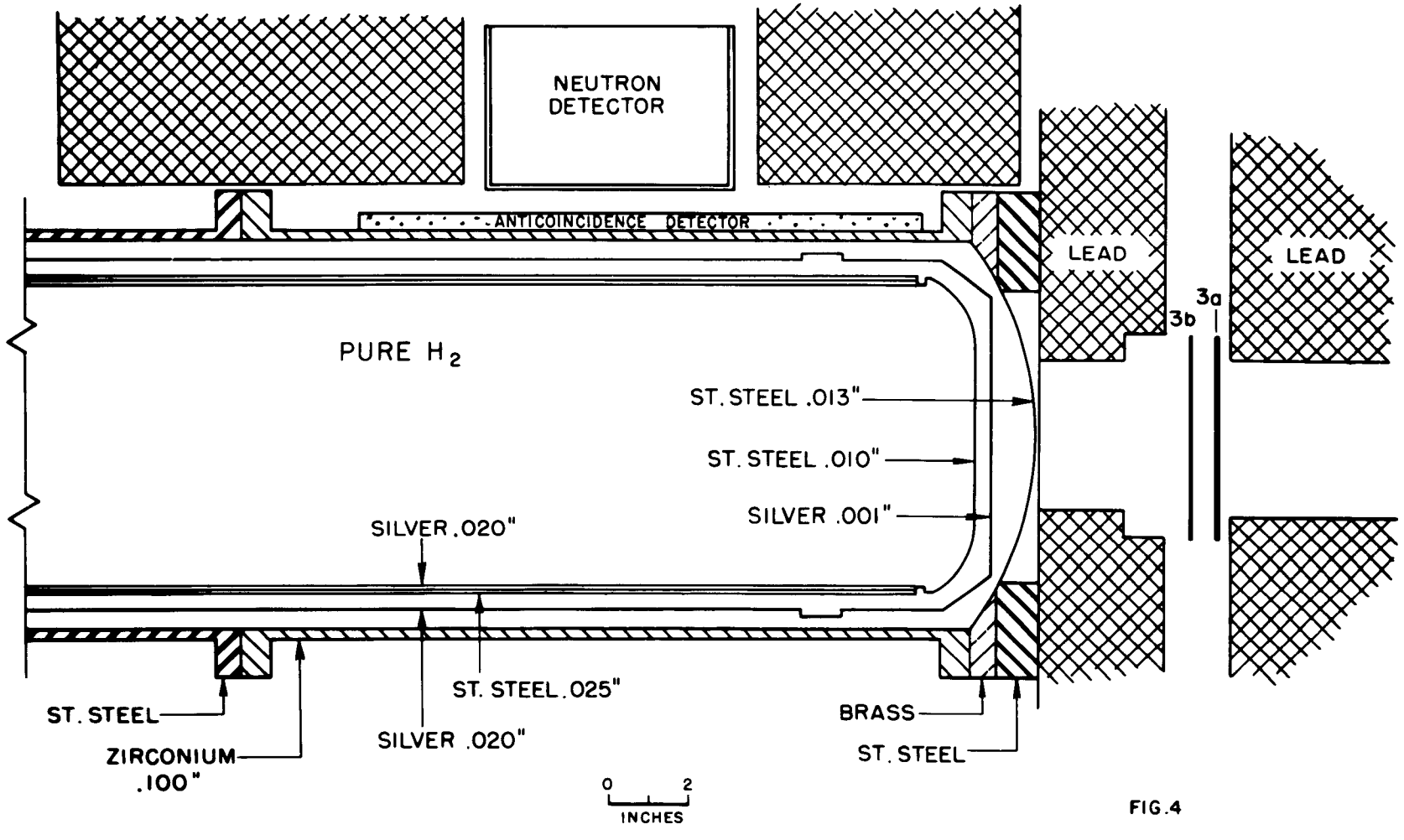
NEUTRON DETECTOR
ANTICOINCIDENCE DETECTOR
LEAD
LEAD
3a
3b
PURE H_2
ST. STEEL .013"
ST. STEEL .010"
SILVER .001"
SILVER .020"
ST. STEEL .025"
SILVER .020"
ST. STEEL
ZIRCONIUM .100"
BRASS
ST. STEEL
0 2
INCHES

FIG.4

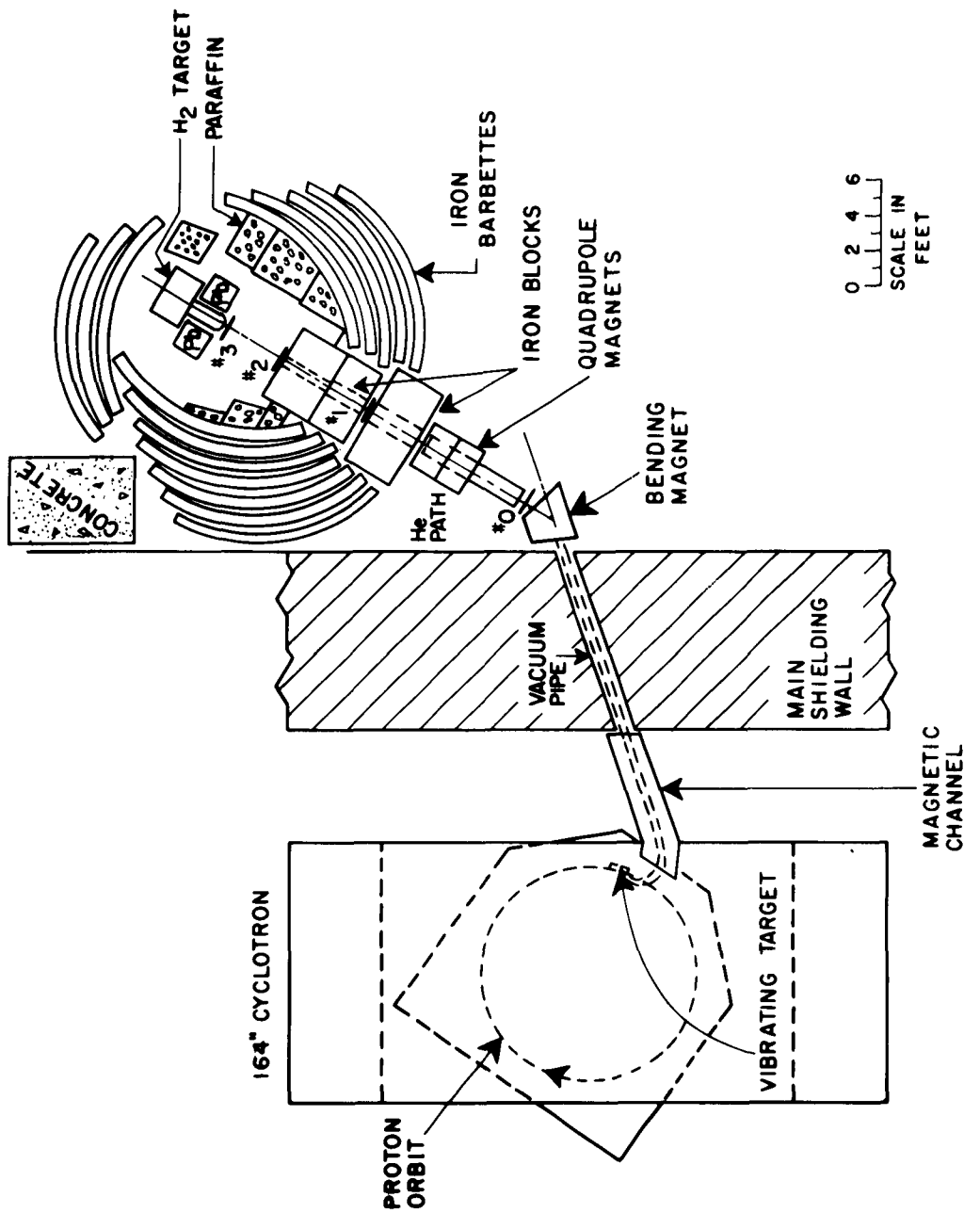
H2 TARGET
PARAFFIN
IRON BARBETTES
IRON BLOCKS
QUADRUPOLE MAGNETS
BENDING MAGNET
He PATH
CONCRETE
#0
#1
#2
#3
0 2 4 6
SCALE IN FEET
VACUUM PIPE
MAIN SHIELDING WALL
MAGNETIC CHANNEL
164" CYCLOTRON
VIBRATING TARGET
PROTON ORBIT

FIG. 5

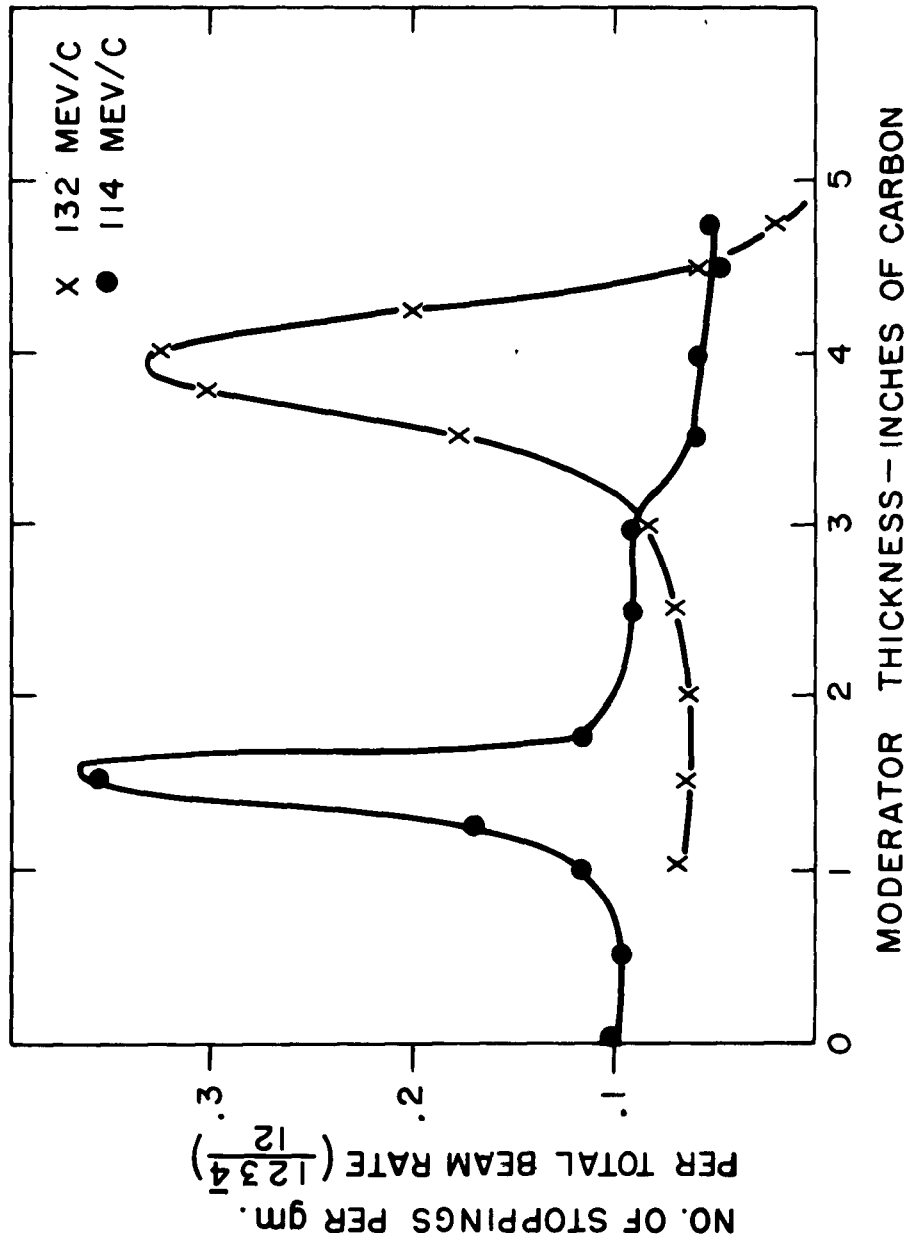
NO. OF STOPPINGS PER gm.
PER TOTAL BEAM RATE $(\frac{123\bar{4}}{12})$
.3
.2
.1
0
1
2
3
4
5
MODERATOR THICKNESS—INCHES OF CARBON
X 132 MEV/C
● 114 MEV/C

FIG. 6

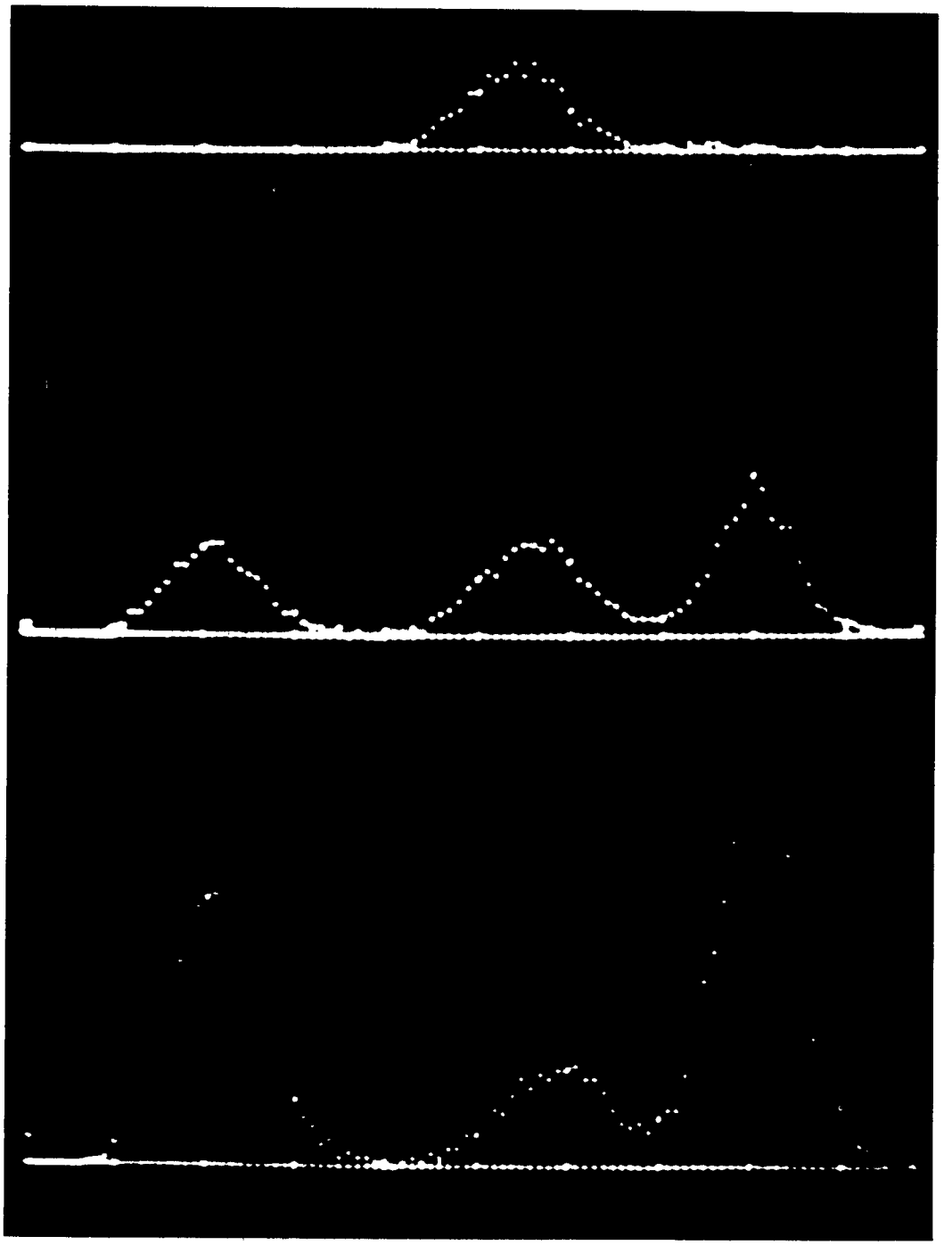

FIG. 7

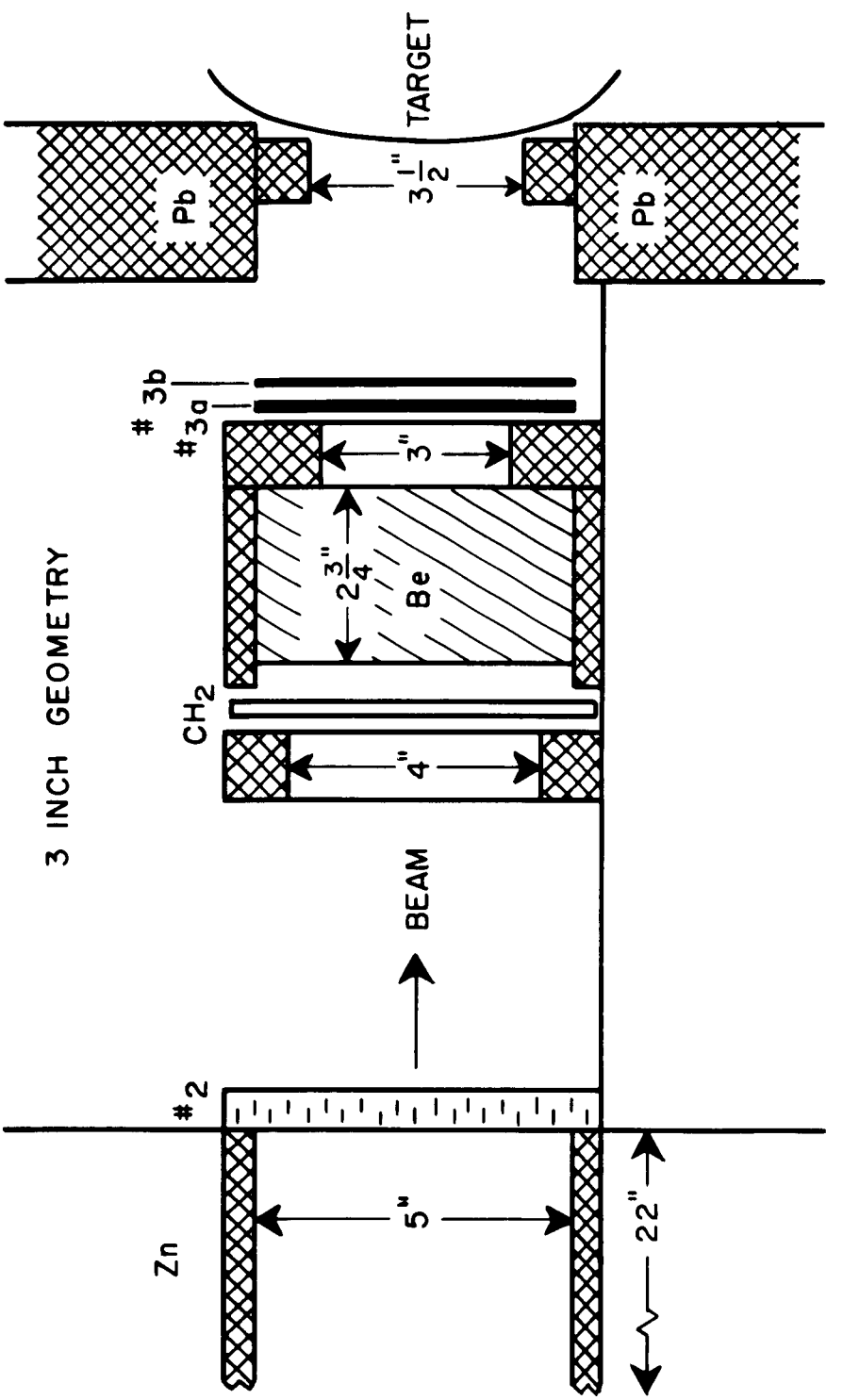
TARGET
Pb
Pb
3 1/2"
3b
#3a
3"
2 3/4"
Be
CH2
4"
3 INCH GEOMETRY
BEAM
#2
Zn
5"
22"

FIG. 8a

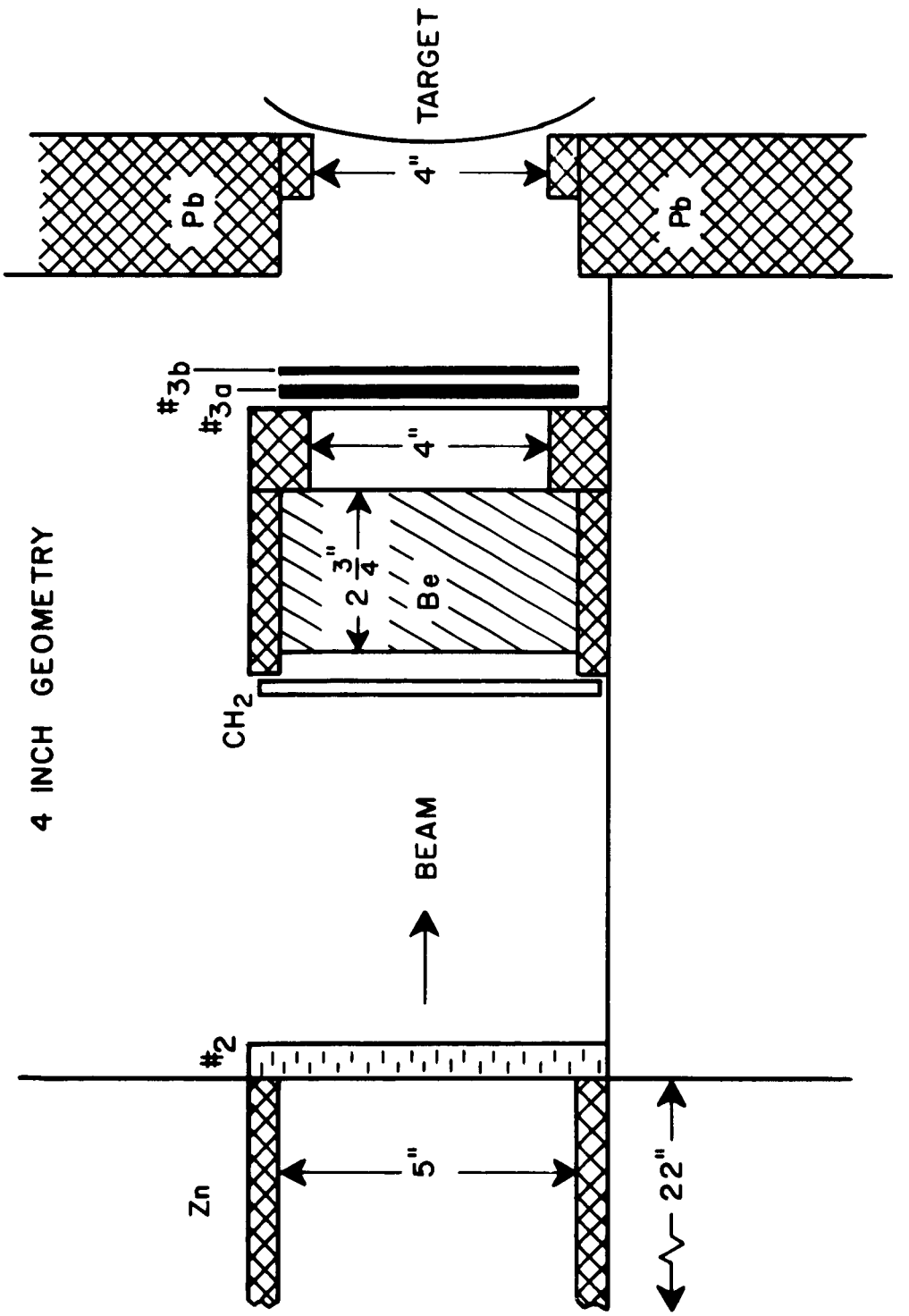

FIG. 8 b

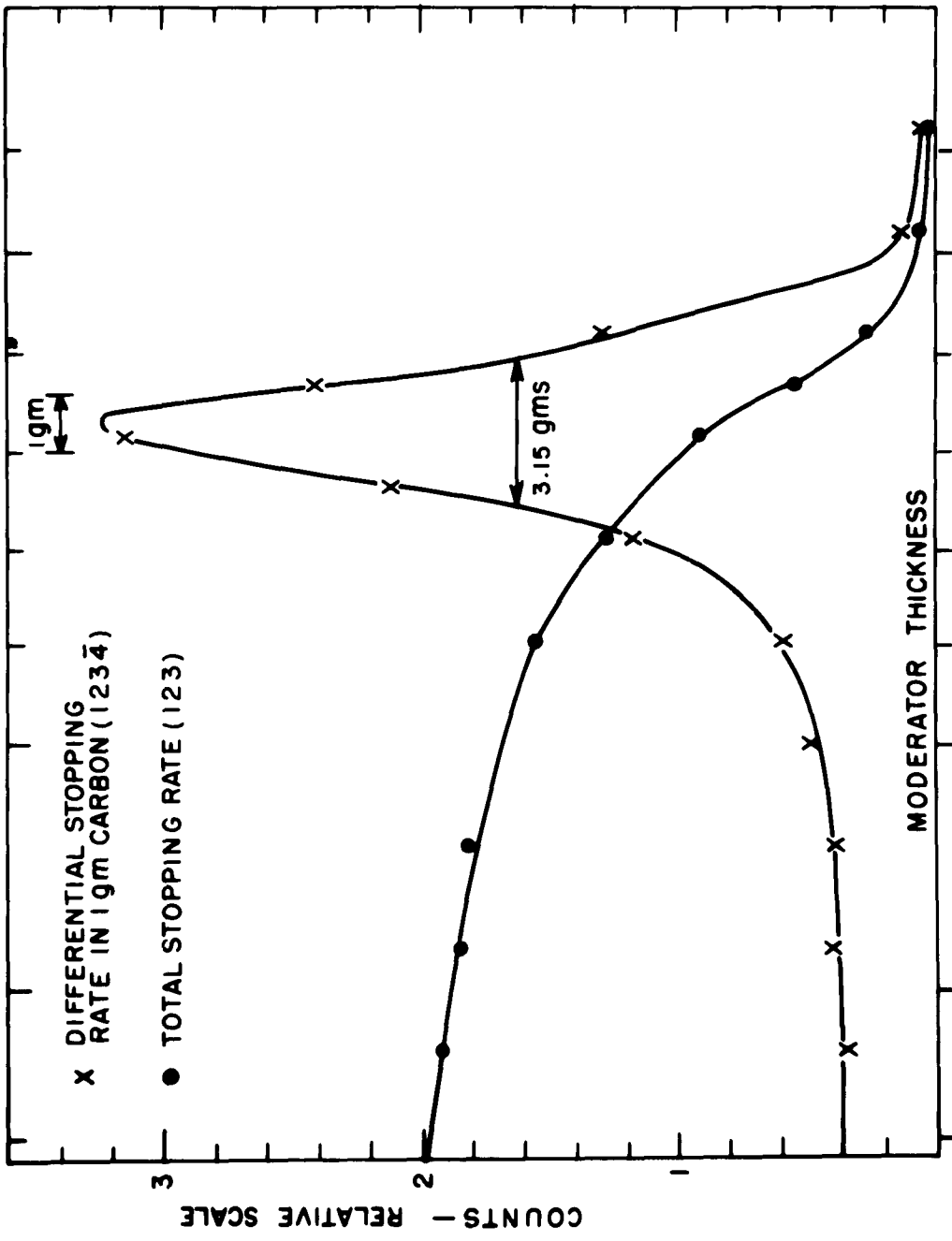
COUNTS — RELATIVE SCALE
3
2
1
2
5
10
20 GMS
MODERATOR THICKNESS
1gm
3.15 gms
X DIFFERENTIAL STOPPING RATE IN 1 gm CARBON (1234)
● TOTAL STOPPING RATE (123)

FIG. 9

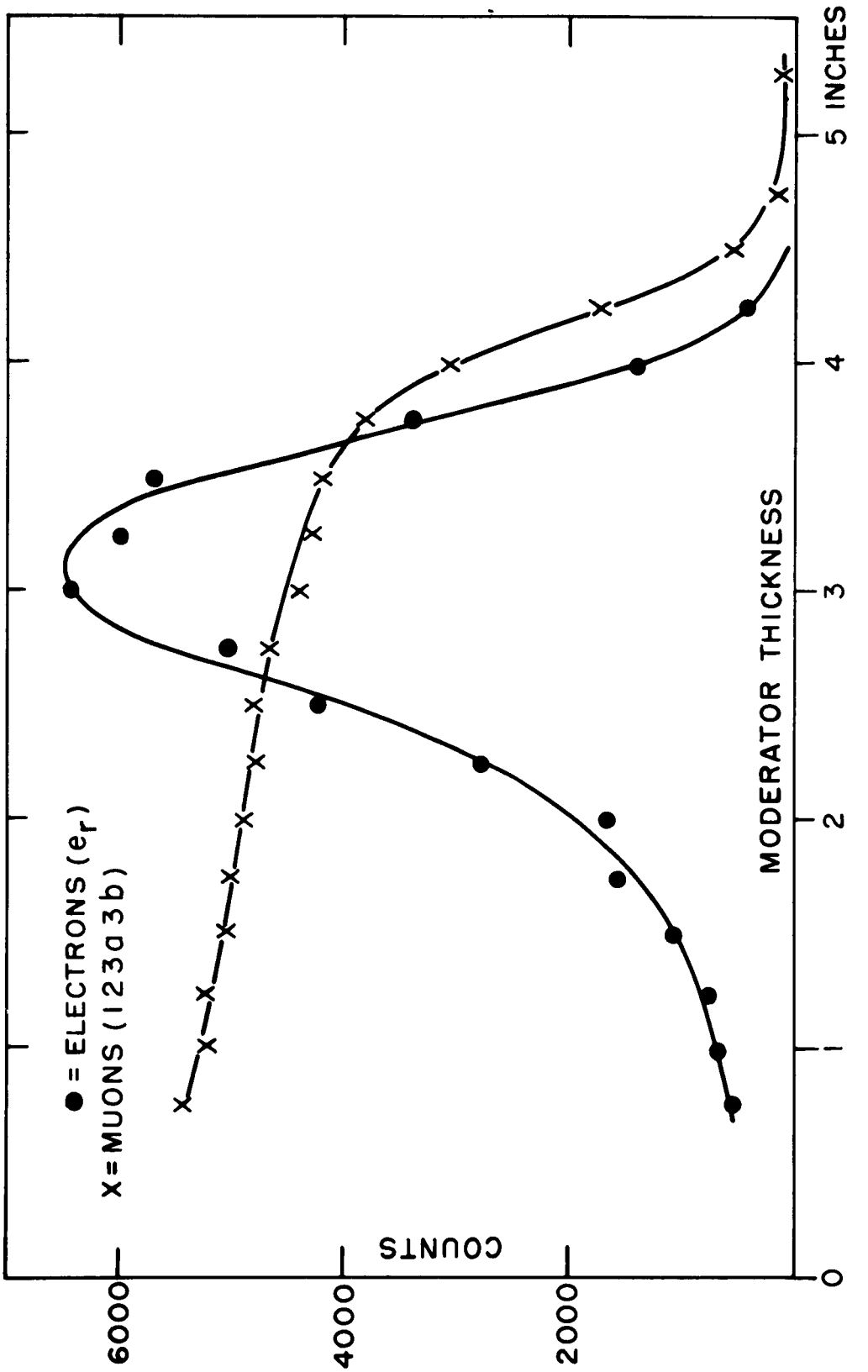
● = ELECTRONS (e_r)
X = MUONS (123a3b)
COUNTS
6000
4000
2000
0
1
2
3
4
5 INCHES
MODERATOR THICKNESS

FIG. 10

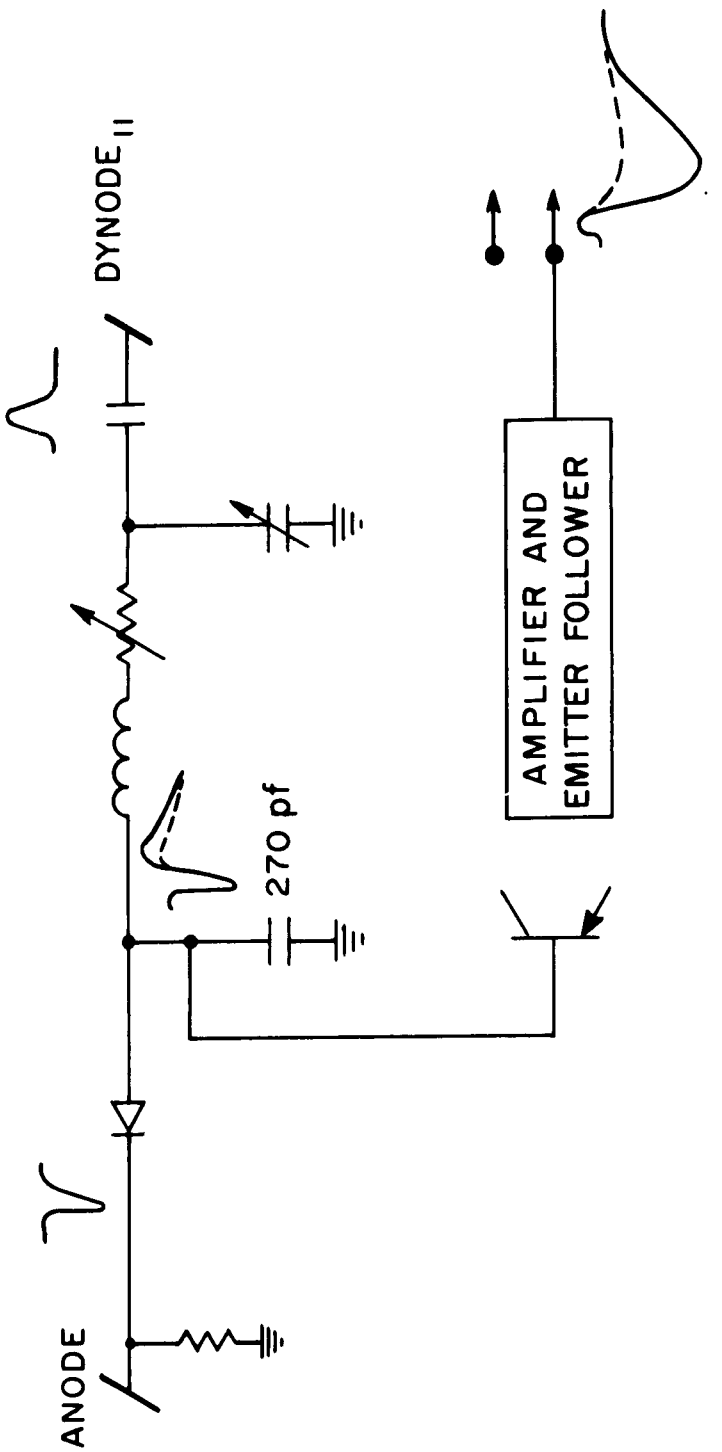

FIG. 11

FIG.12a

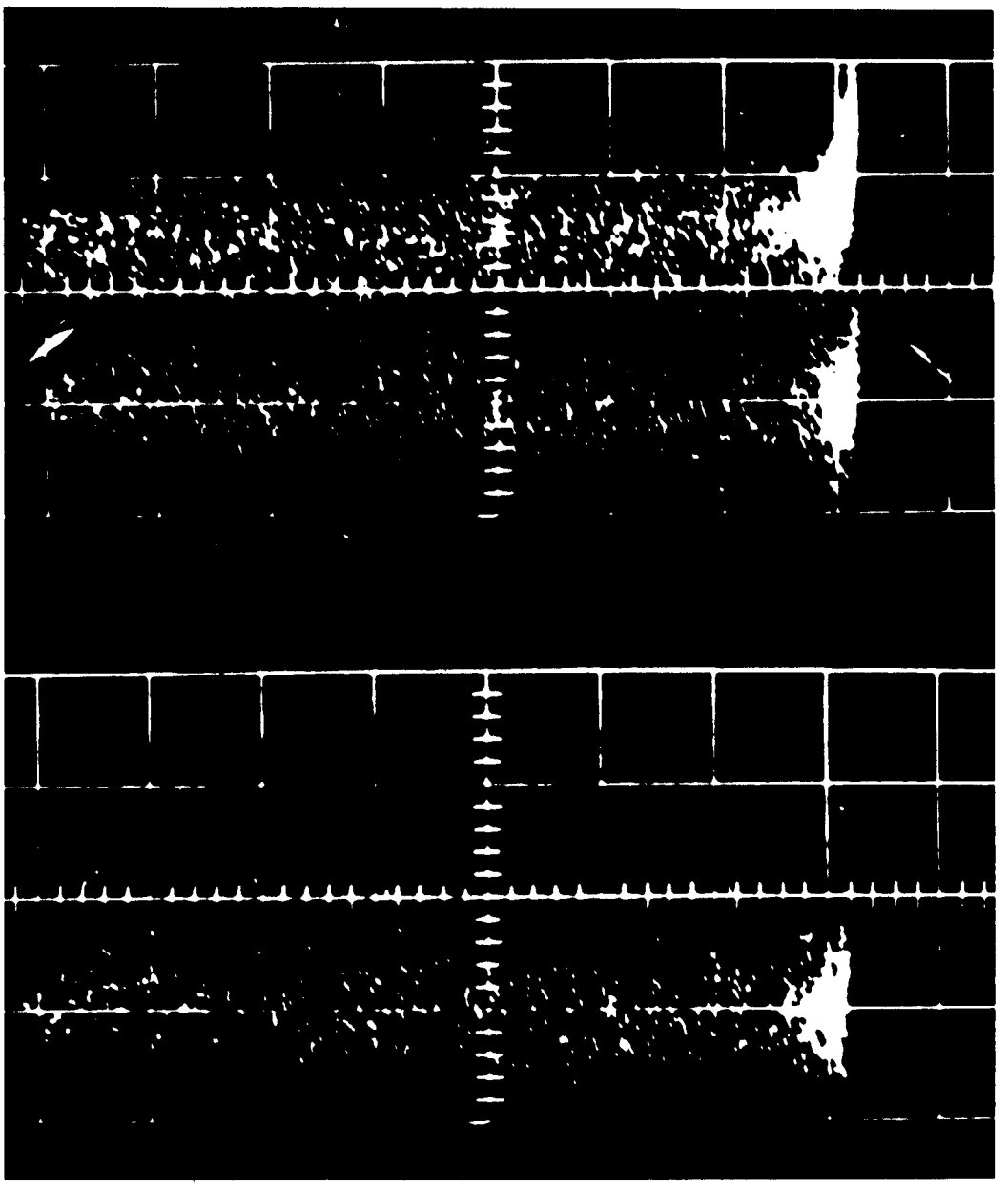

FIG.12b

ROLL 42 CO 60 N1

14652
1163061 1
12508384 1
36379521
2657031
125926
58591
2510321
132812
227632
142511
122
1 1

ROLL 39 N1 NA 24

31242 1
20100 1
2 145384 1
1165844 1
15224
2485811
43221
1 2264 1
1136811
323841
133322 1
13141
12 211
121111
211 1
111211
111 11
3 22
211
122
1 2 1
11
21
1
1113
223
1111 1
111 1 2

111

FIG. 12c

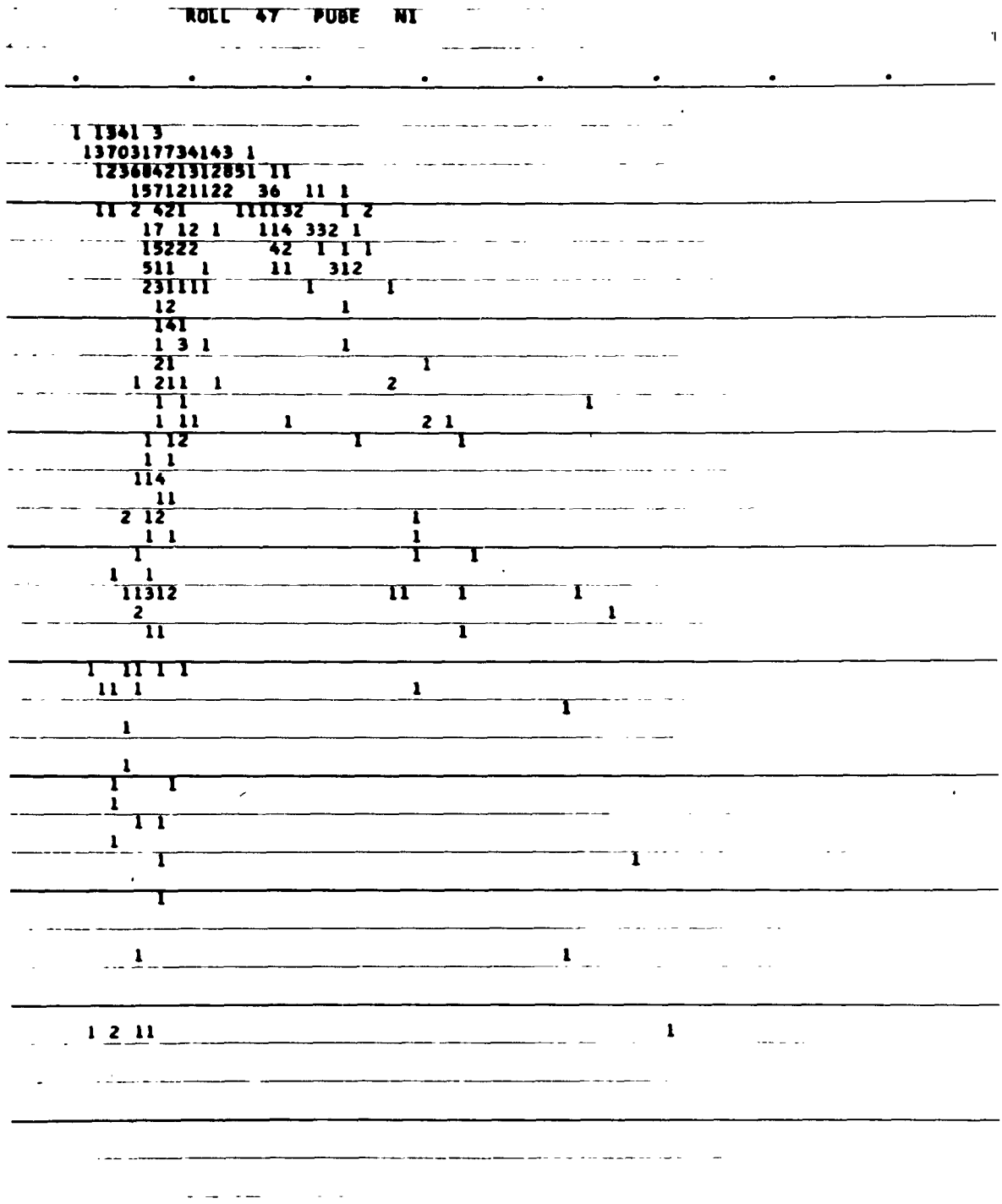

FIG.12d

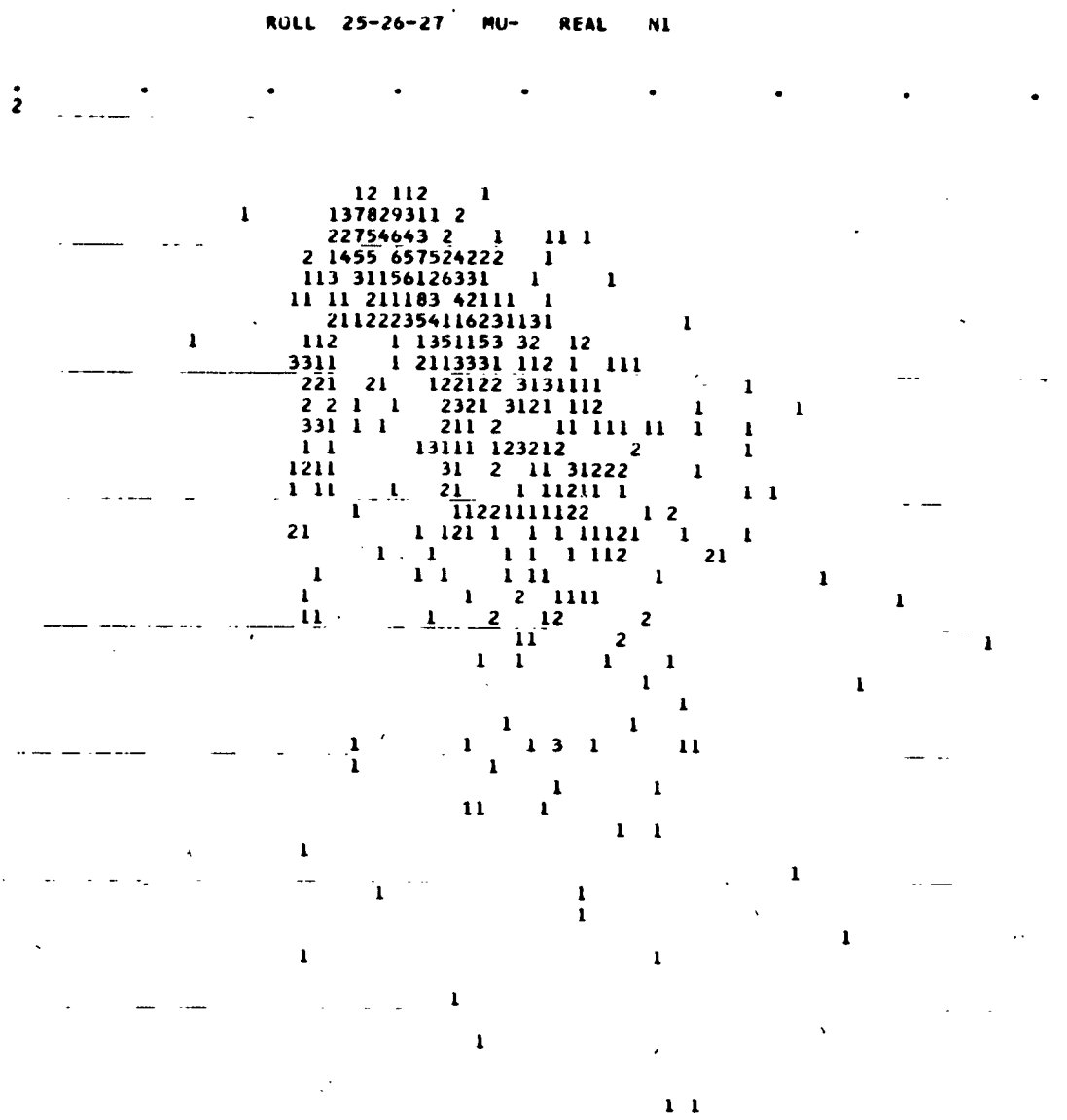

FIG.12e

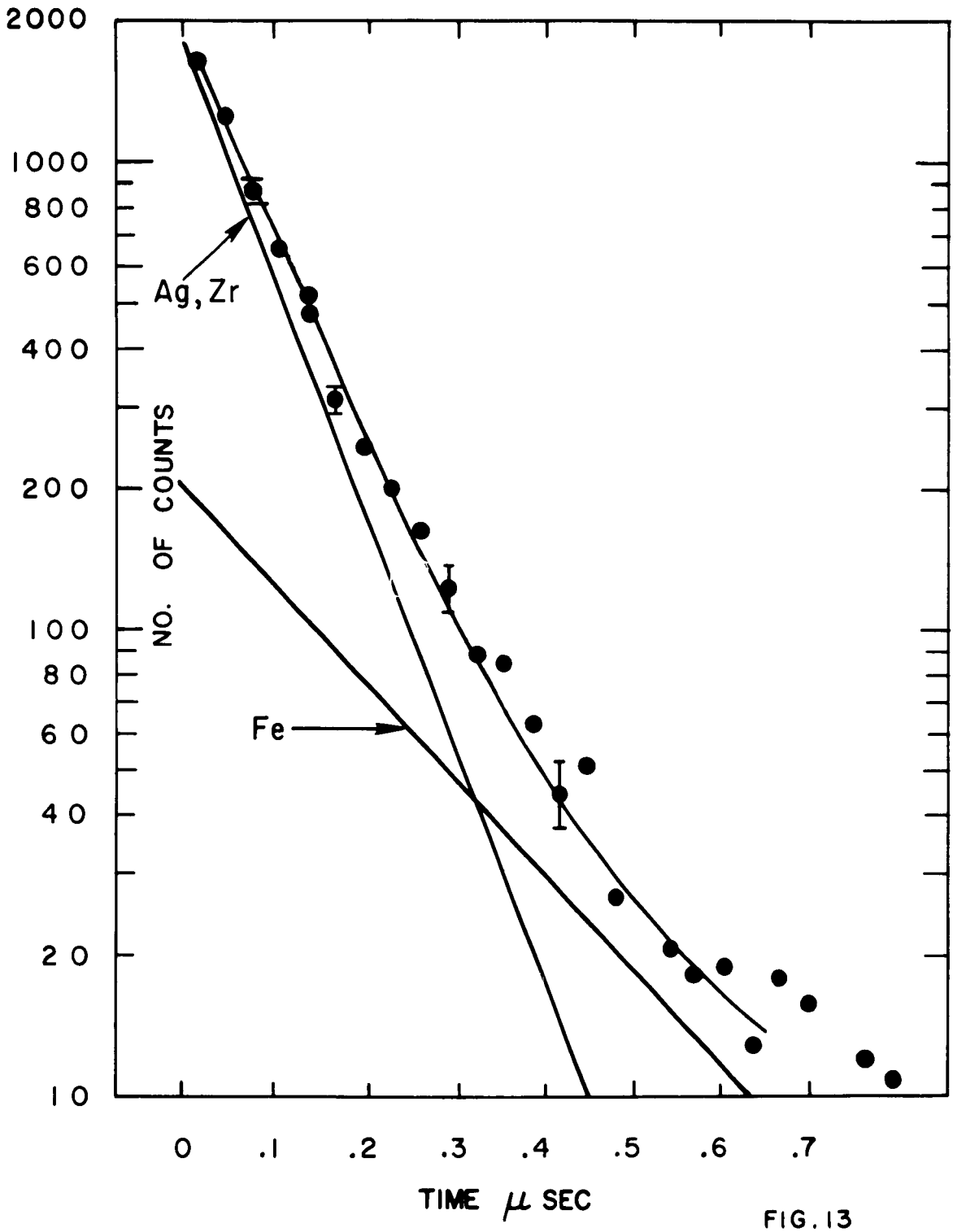
2000
1000
800
600
400
200
100
80
60
40
20
10
NO. OF COUNTS
Ag, Zr
Fe
0
.1
.2
.3
.4
.5
.6
.7
TIME μ SEC

FIG. 13

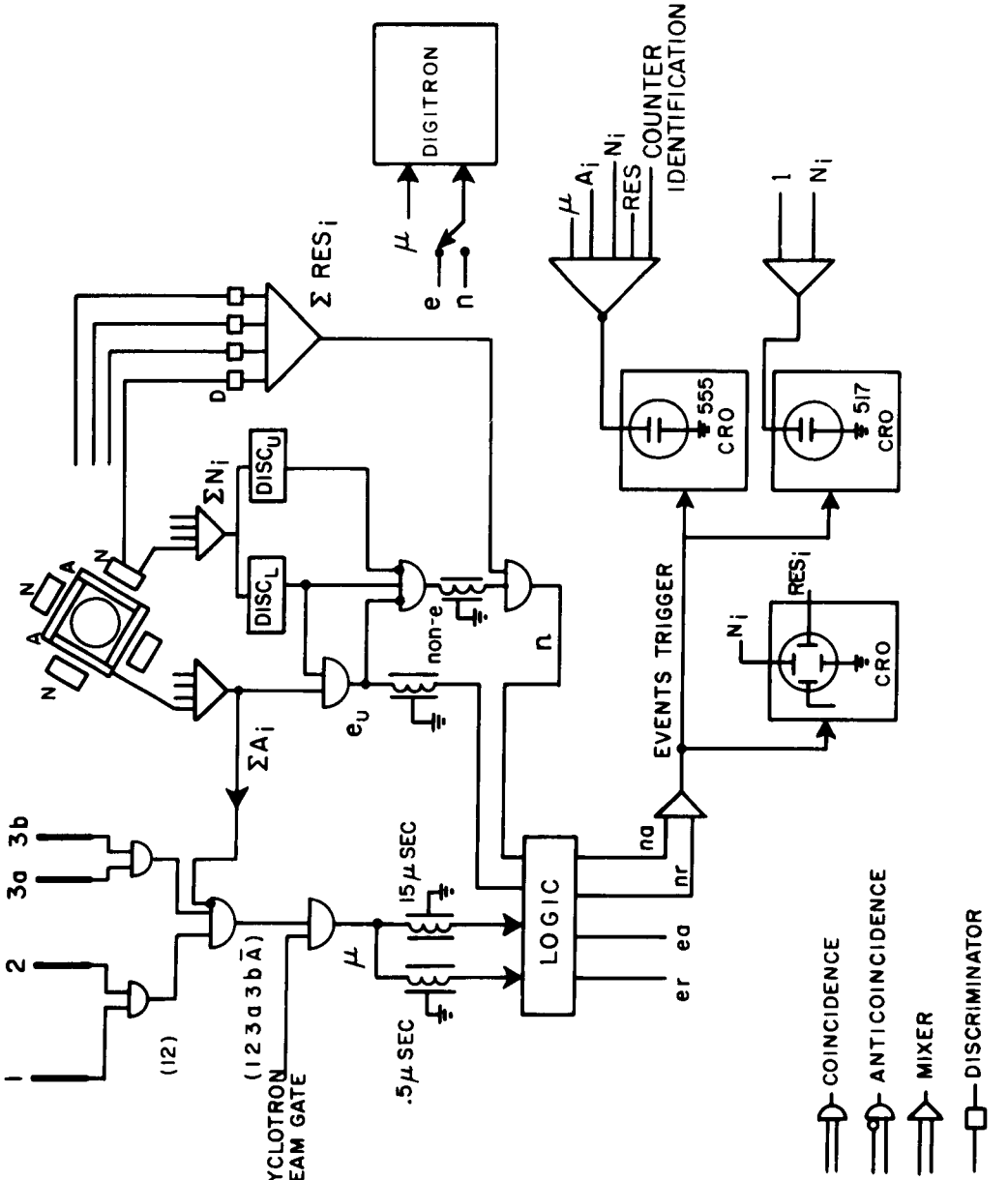
1
2
3a
3b
(12)
(123a3bĀ)
CYCLOTRON BEAM GATE
.5μ SEC
15μ SEC
μ
LOGIC
na
nr
er
ea
ΣAi
ΣNi
ΣRESi
DISCU
DISCL
eU
non-e
n
D
A
N
DIGITRON
e
n
EVENTS TRIGGER
μ
Ai
Ni
RES
COUNTER IDENTIFICATION
555 CRO
517 CRO
CRO
RESi
1
COINCIDENCE
ANTICOINCIDENCE
MIXER
DISCRIMINATOR

FIG. 14

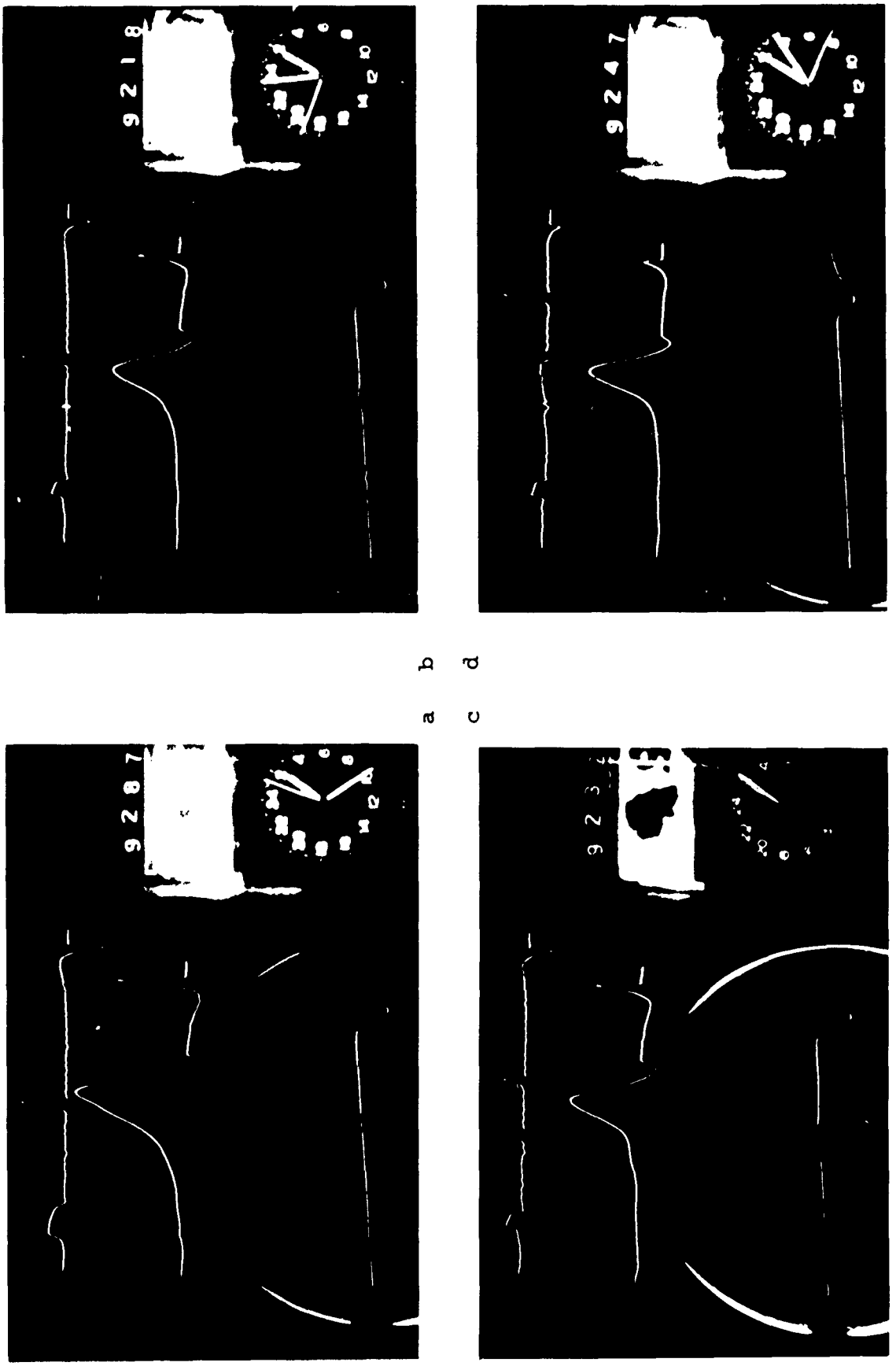

FIG. 15

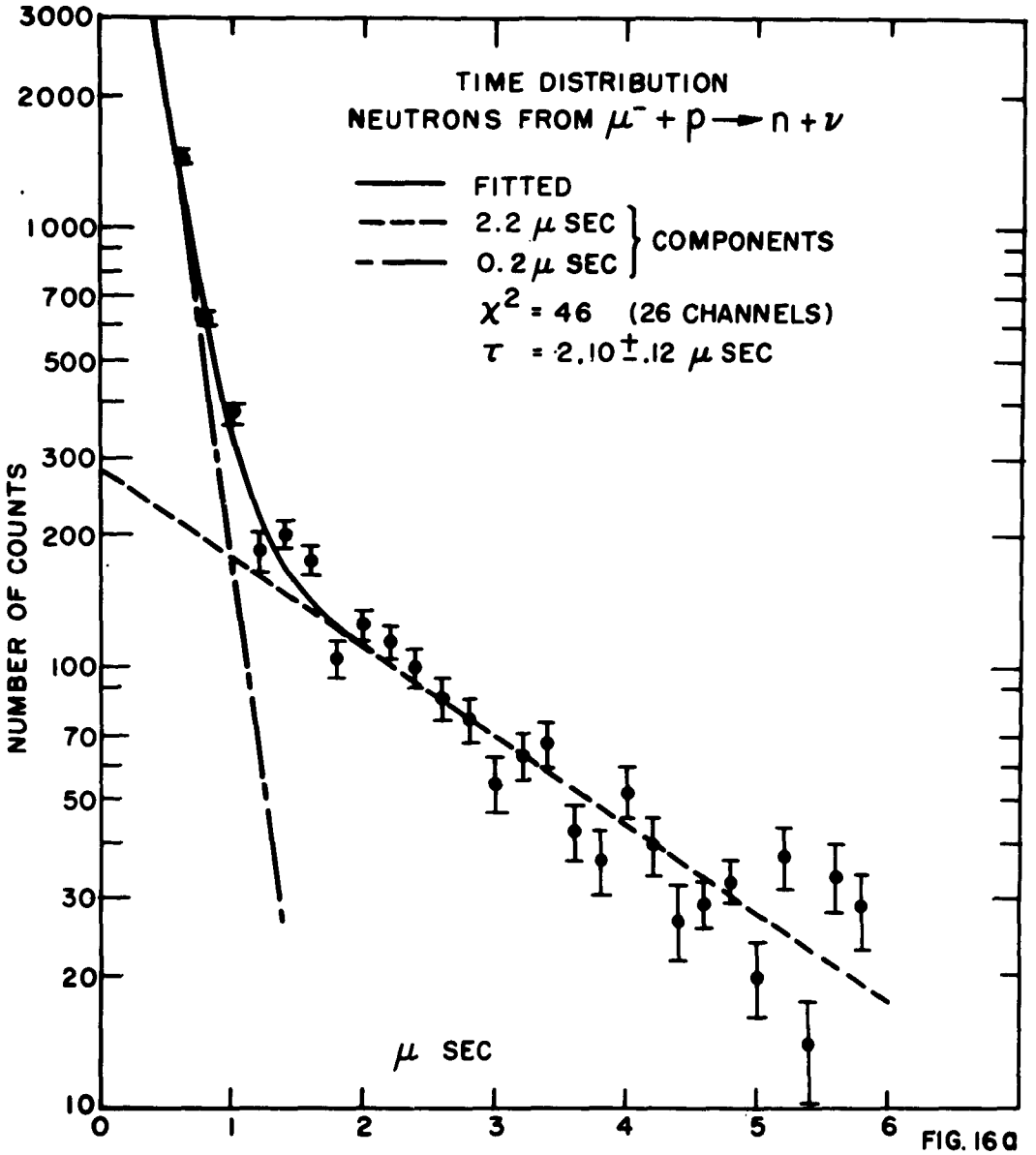
TIME DISTRIBUTION
NEUTRONS FROM $\mu^- + p \rightarrow n + \nu$
FITTED
2.2 μ SEC
0.2 μ SEC
COMPONENTS
$\chi^2 = 46$ (26 CHANNELS)
$\tau = 2.10 \pm .12$ μ SEC
NUMBER OF COUNTS
μ SEC
3000
2000
1000
700
500
300
200
100
70
50
30
20
10
0
1
2
3
4
5
6

FIG. 16a

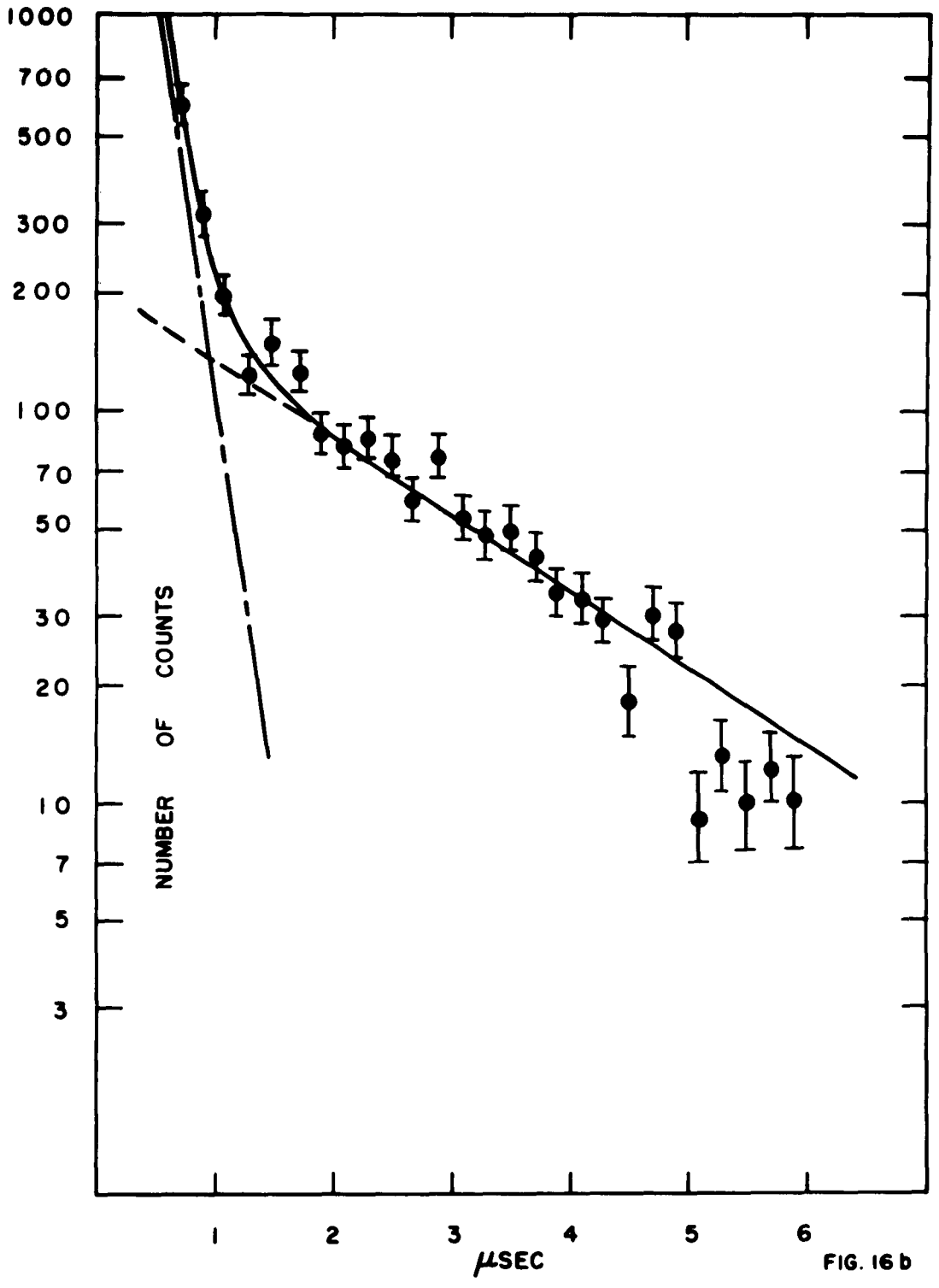
1000
700
500
300
200
100
70
50
30
20
10
7
5
3
NUMBER OF COUNTS
1
2
3
4
5
6
μSEC

FIG. 16 b

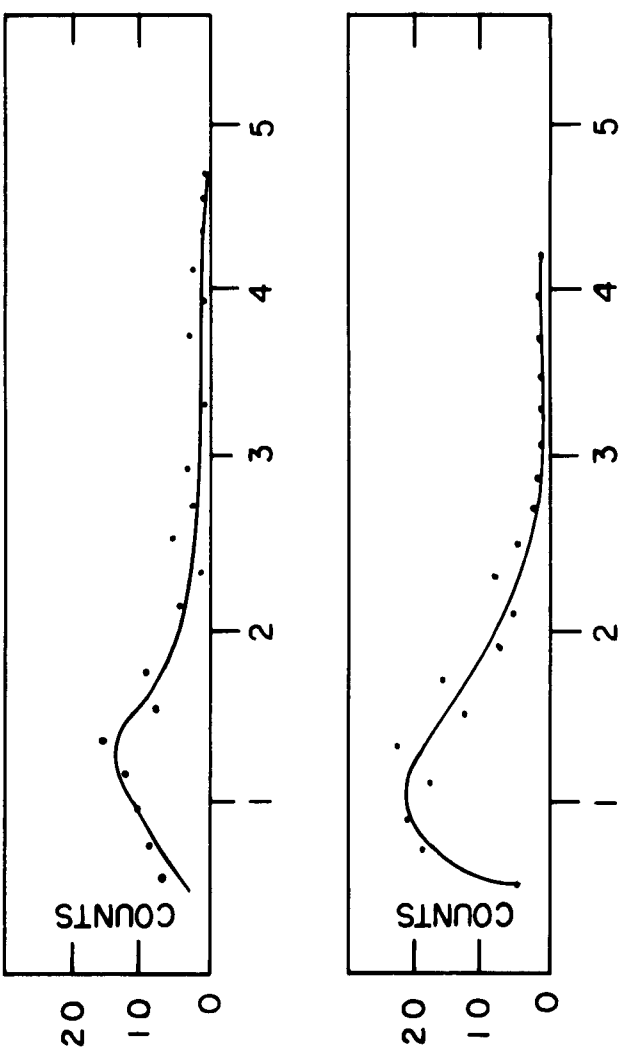

FIG. 17 a

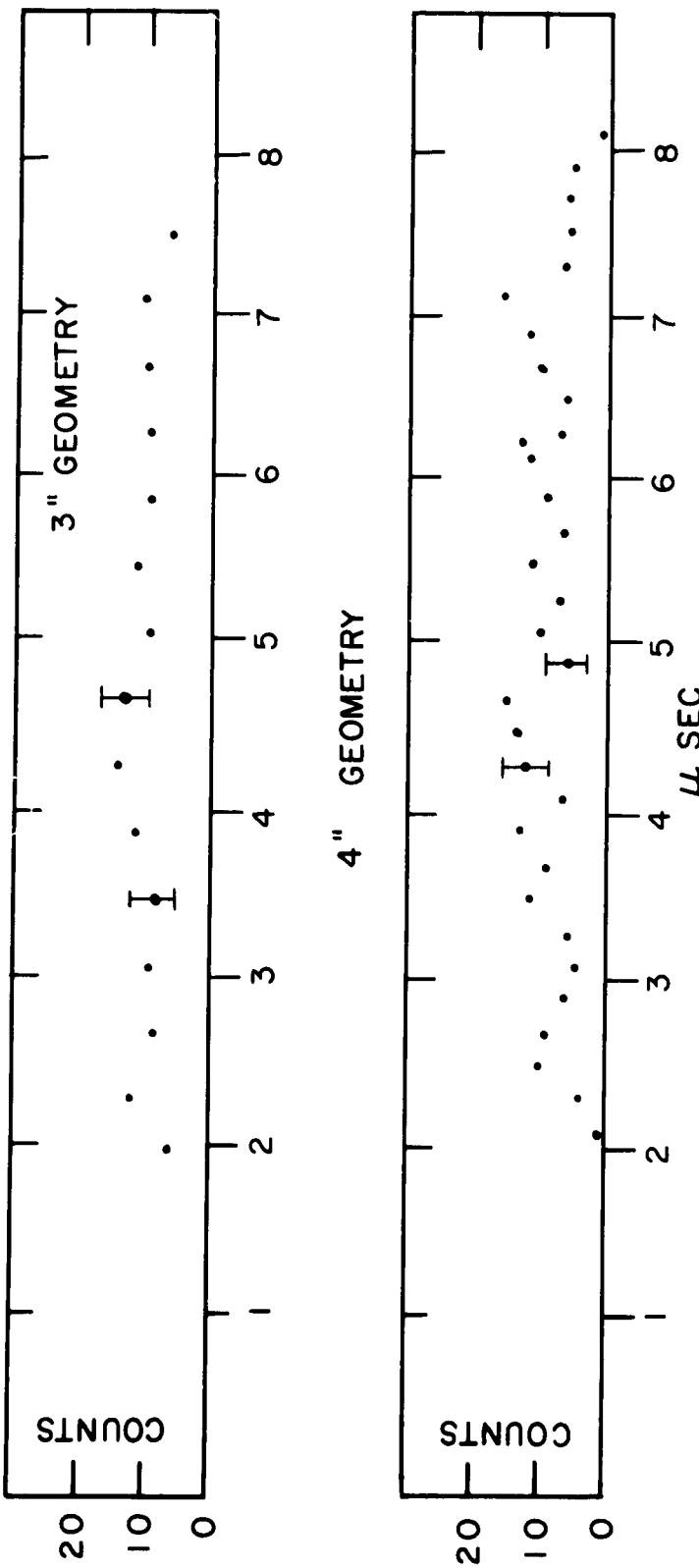
3" GEOMETRY
4" GEOMETRY
COUNTS
20
10
0
1
2
3
4
5
6
7
8
μ SEC
TIME DISTRIBUTION OF ACCIDENTALS

FIG. 17 b

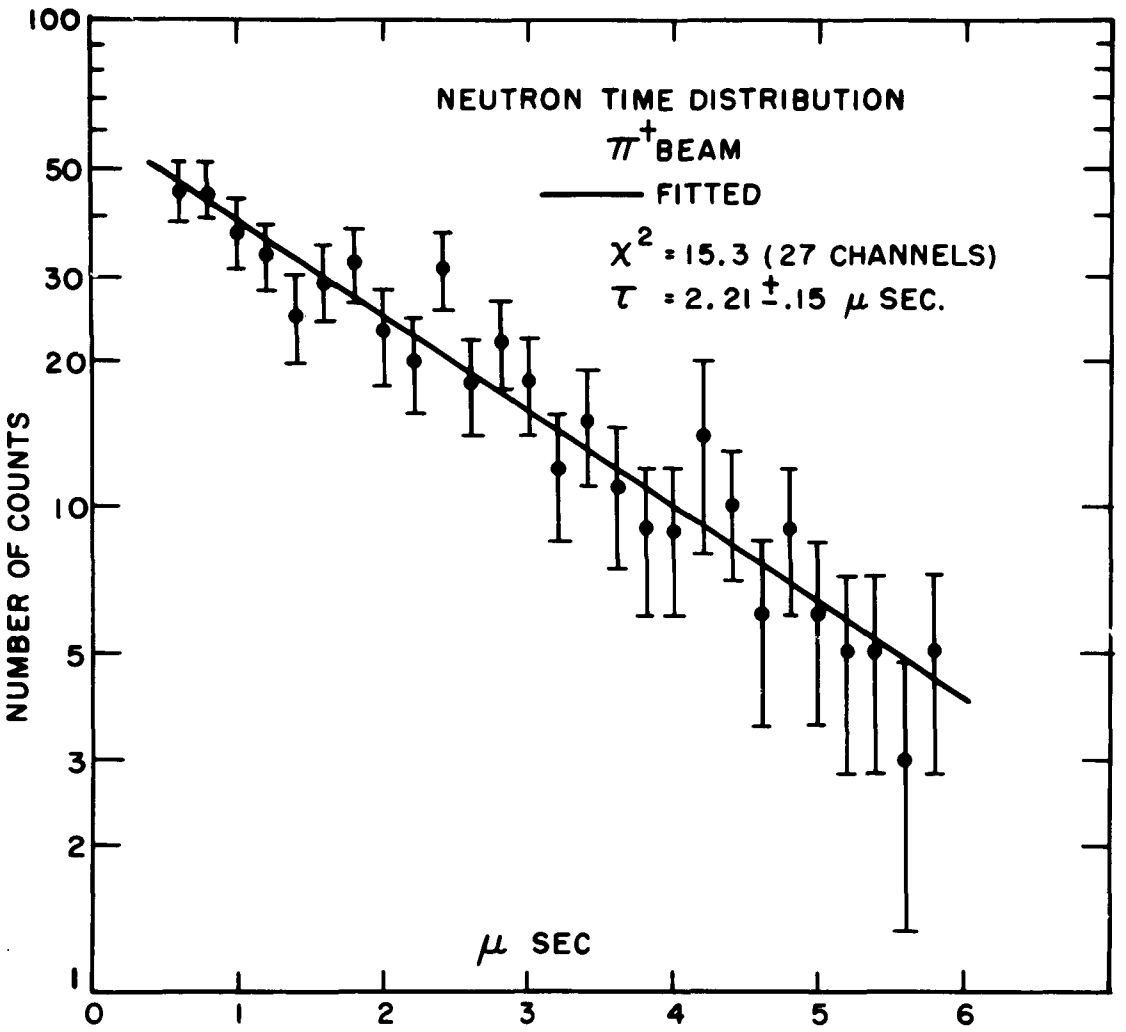
NEUTRON TIME DISTRIBUTION
π^+ BEAM
FITTED
χ^2 = 15.3 (27 CHANNELS)
τ = 2.21 ± .15 μ SEC.
NUMBER OF COUNTS
μ SEC
100
50
30
20
10
5
3
2
1
0
1
2
3
4
5
6

FIG. 18 a

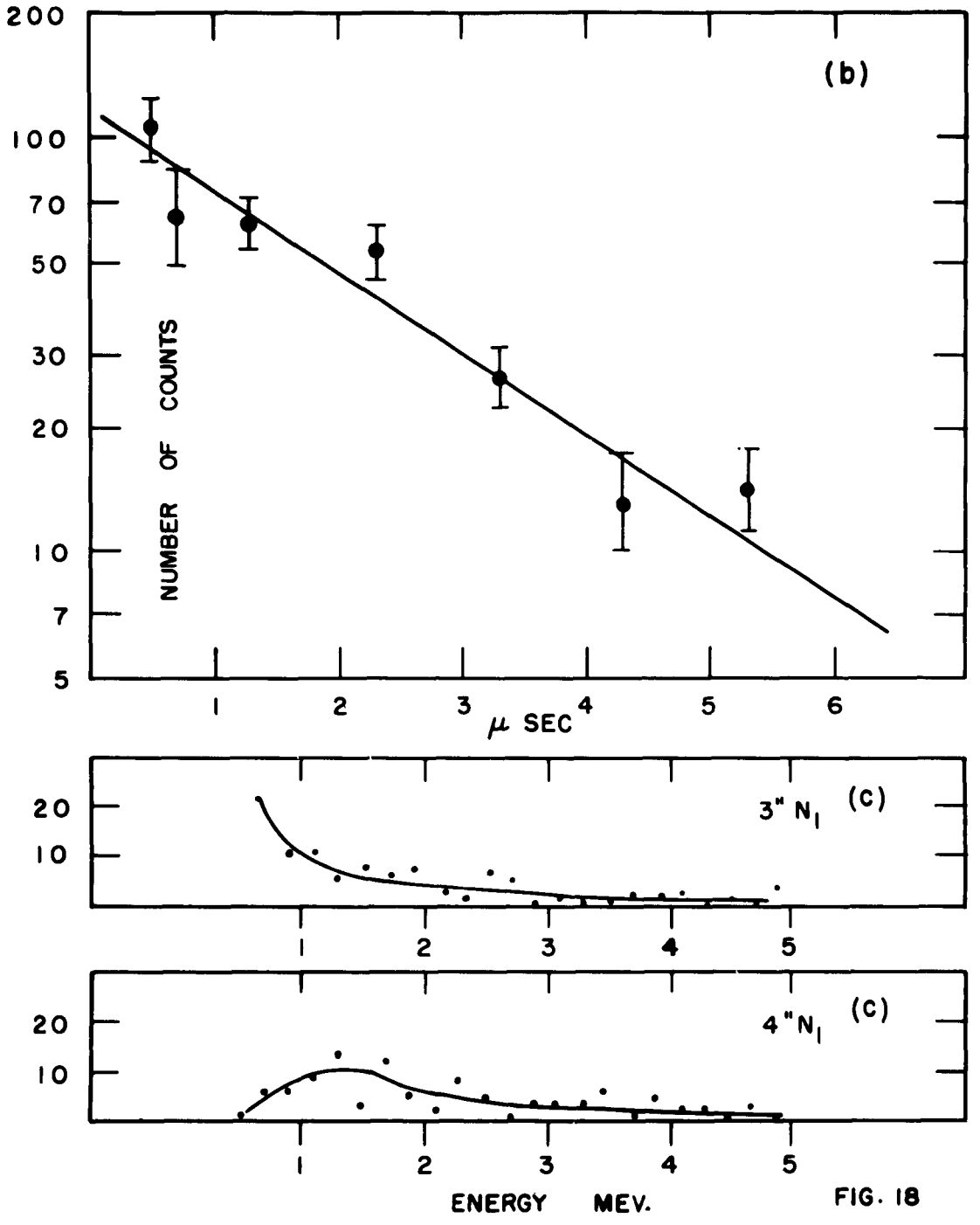
200
100
70
50
30
20
10
7
5
(b)
NUMBER OF COUNTS
1
2
3
4
5
6
μ SEC
20
10
3" N1
(C)
1
2
3
4
5
20
10
4" N1
(C)
1
2
3
4
5
ENERGY MEV.

FIG. 18

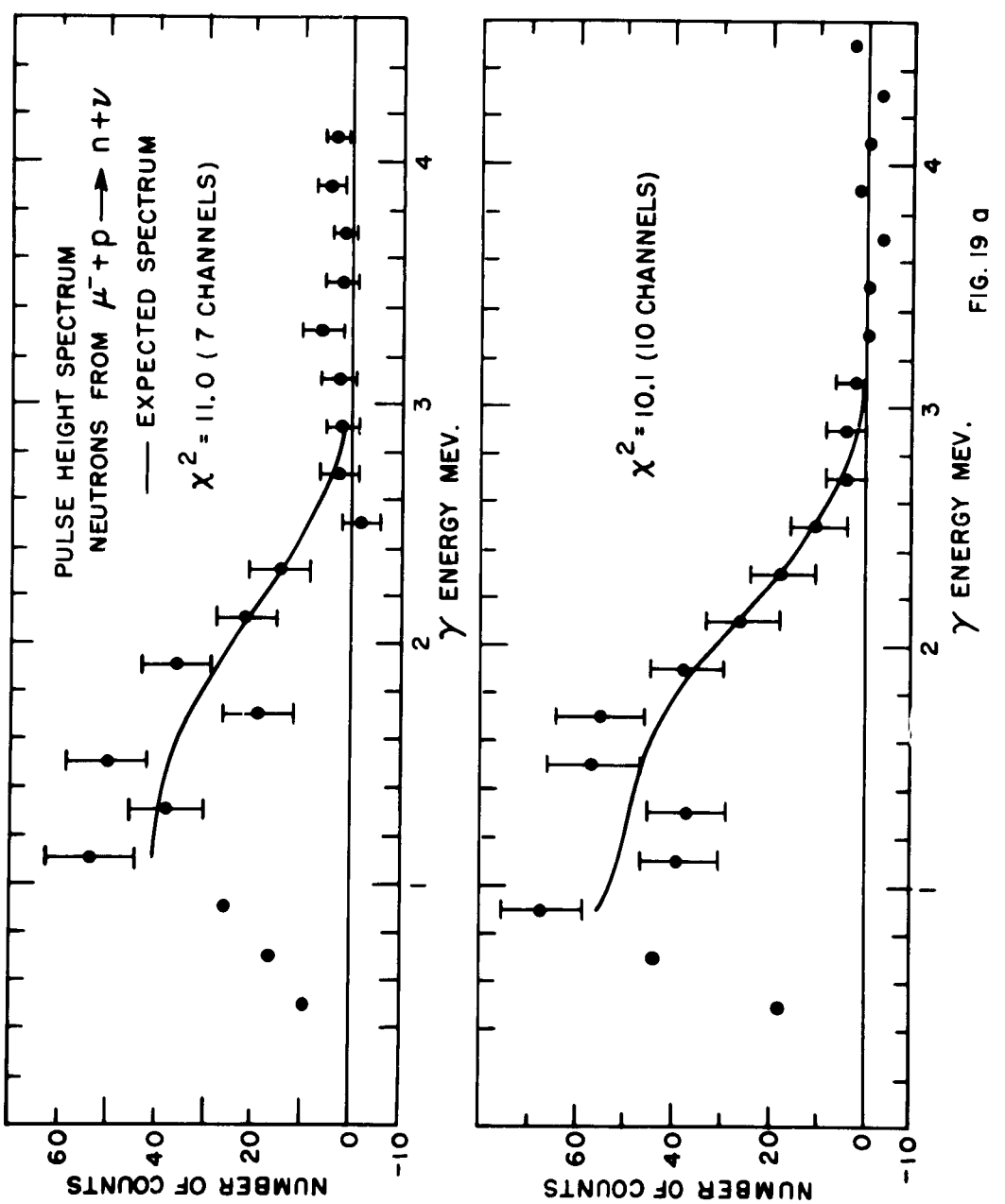
PULSE HEIGHT SPECTRUM
NEUTRONS FROM $\mu^- + p \rightarrow n + \nu$
— EXPECTED SPECTRUM
χ^2 = 11.0 (7 CHANNELS)
NUMBER OF COUNTS
60
40
20
0
-10
1
2
3
4
γ ENERGY MEV.
χ^2 = 10.1 (10 CHANNELS)
NUMBER OF COUNTS
60
40
20
0
-10
1
2
3
4
γ ENERGY MEV.

FIG. 19 a

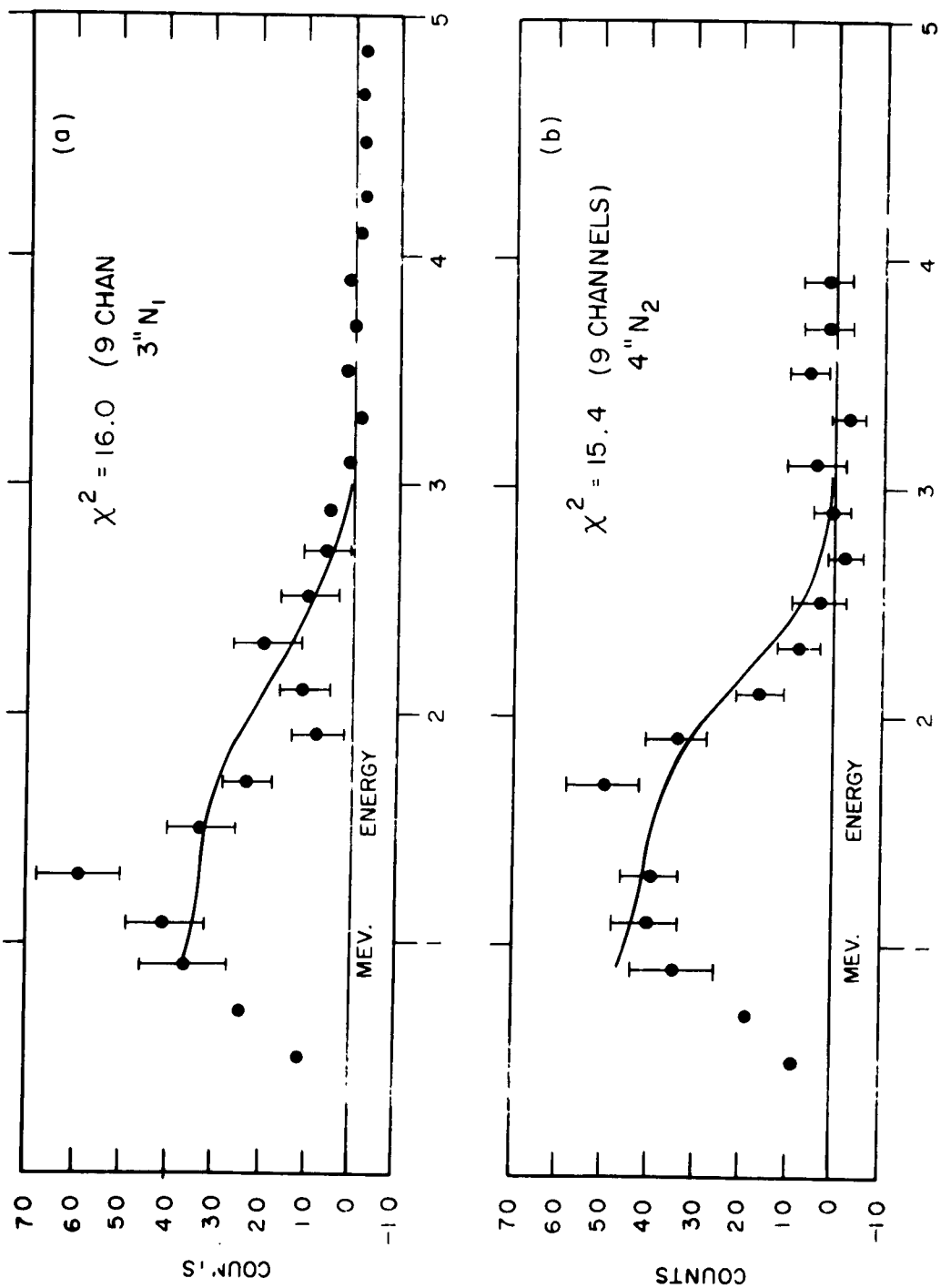
(a)
χ^2 = 16.0 (9 CHAN
3" N_1
(b)
χ^2 = 15.4 (9 CHANNELS)
4" N_2
COUNTS
MEV. ENERGY
70
60
50
40
30
20
10
0
-10
1
2
3
4
5

FIG. 19 b

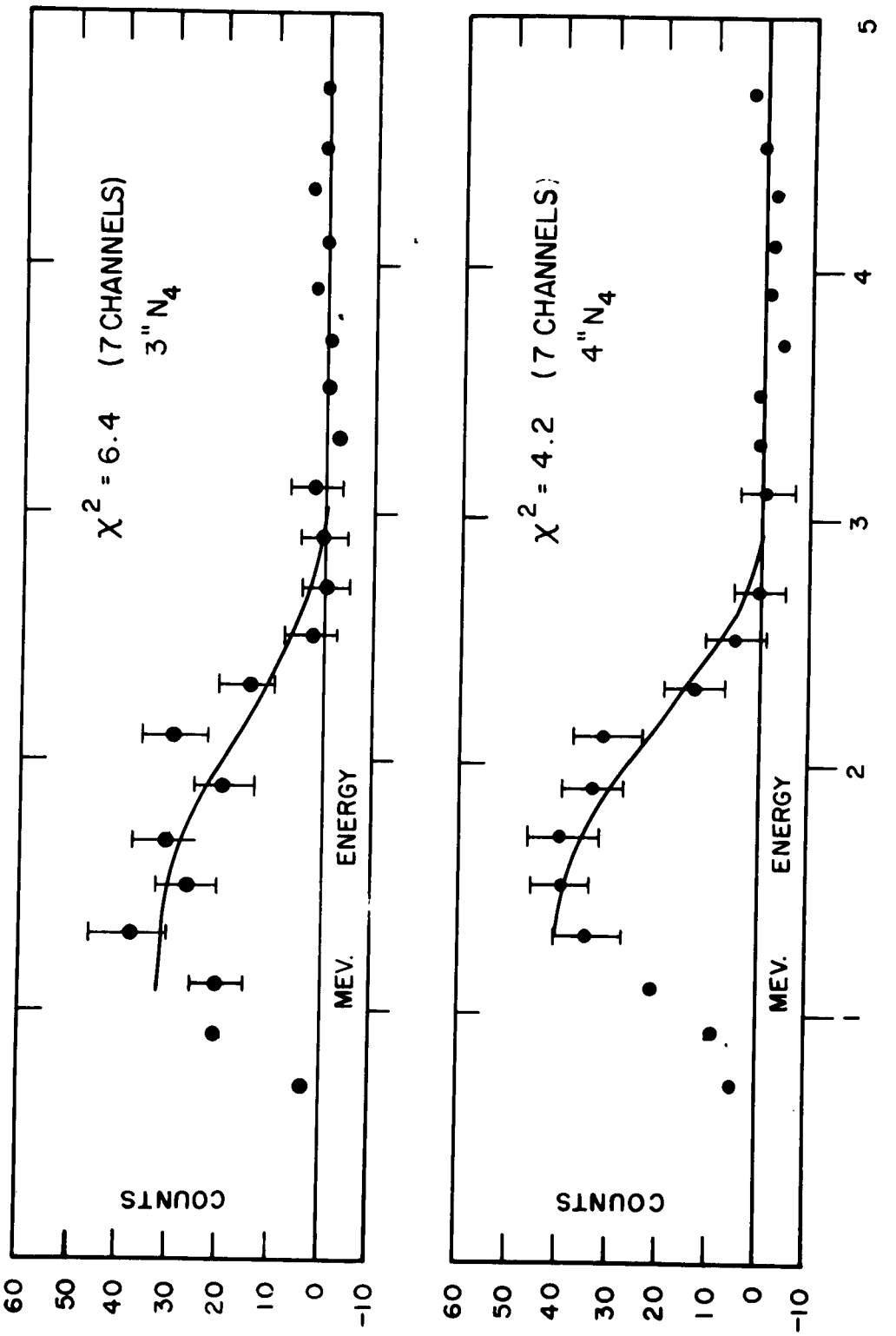
$\chi^2 = 6.4$ (7 CHANNELS)
$3"N_4$
$\chi^2 = 4.2$ (7 CHANNELS)
$4"N_4$
COUNTS
MEV. ENERGY
60
50
40
30
20
10
0
-10
1
2
3
4
5

FIG. 19 C

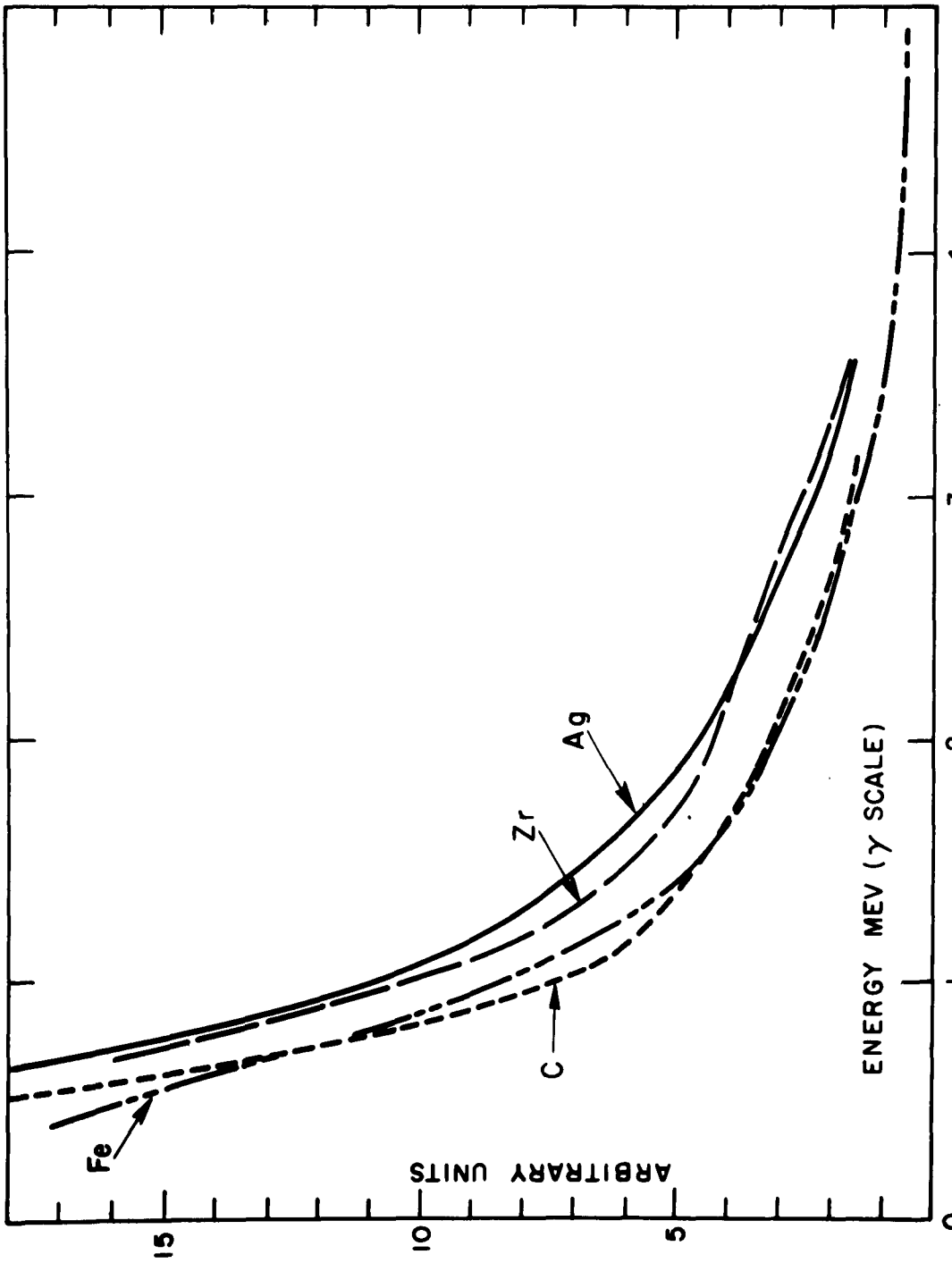

FIG. 20

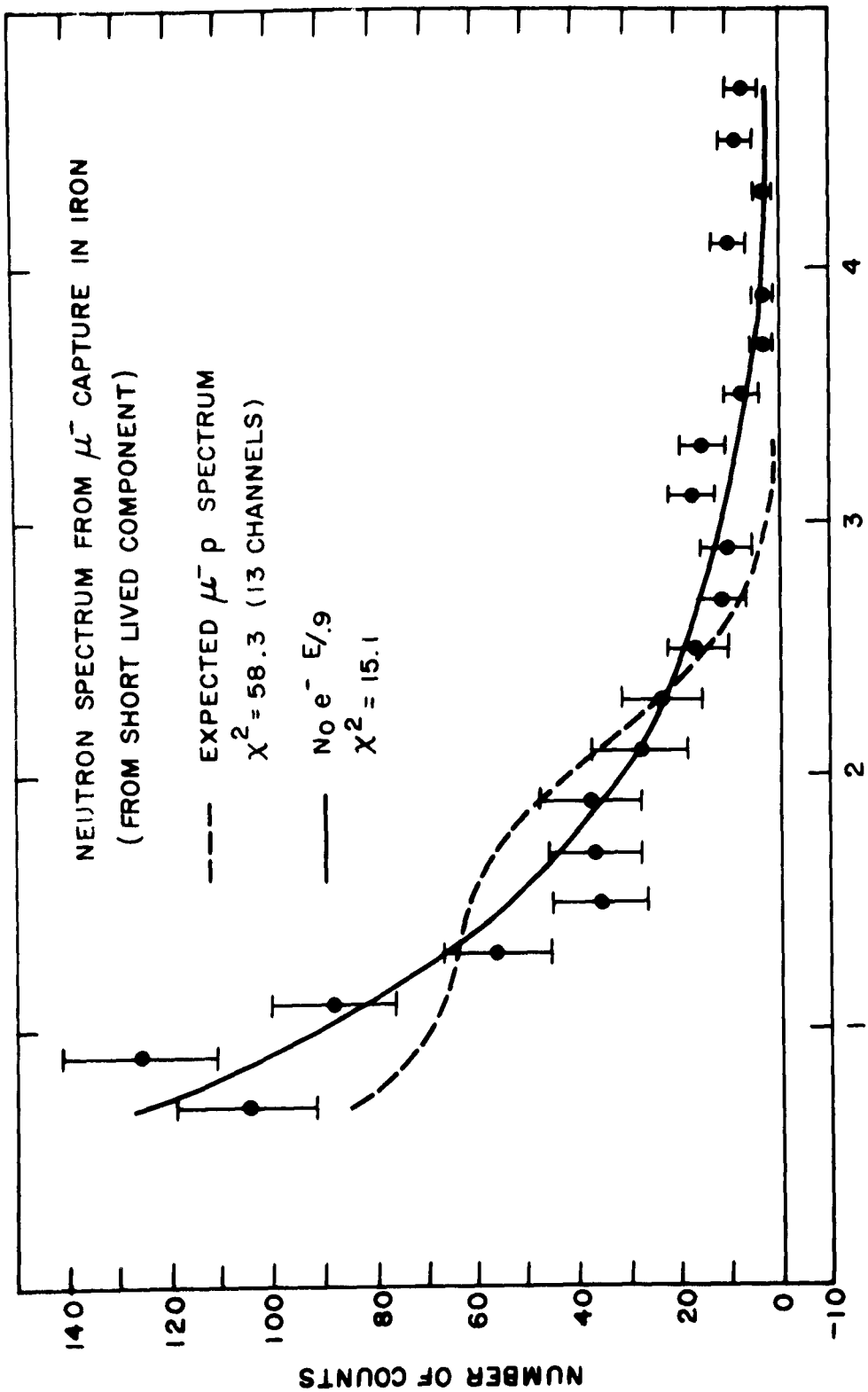
NEUTRON SPECTRUM FROM μ^- CAPTURE IN IRON
(FROM SHORT LIVED COMPONENT)
---- EXPECTED μ^- p SPECTRUM
χ^2 = 58.3 (13 CHANNELS)
—— $N_0 e^- E/.9$
χ^2 = 15.1
NUMBER OF COUNTS
140
120
100
80
60
40
20
0
-10
1
2
3
4
γ ENERGY MEV

FIG. 21

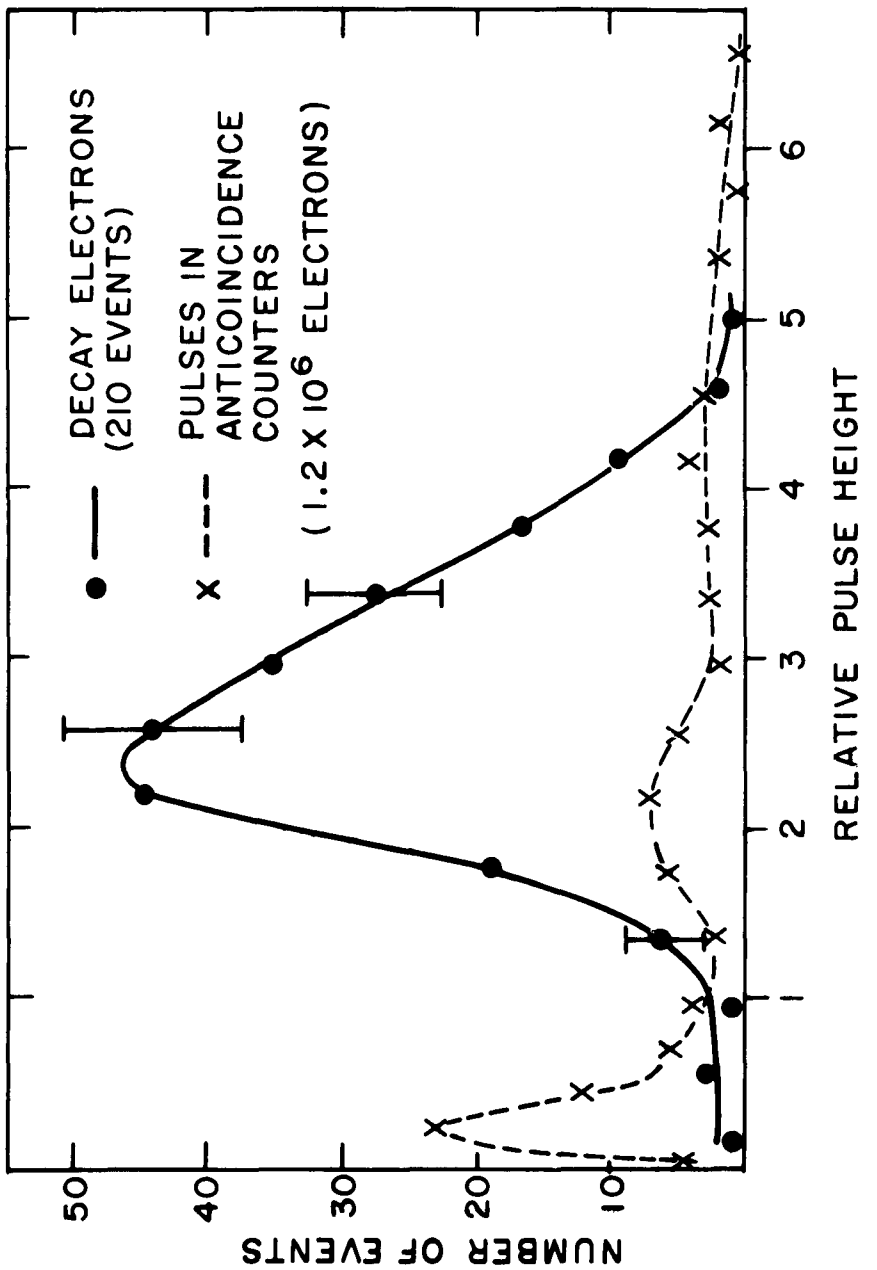
DECAY ELECTRONS
(210 EVENTS)
PULSES IN
ANTICOINCIDENCE
COUNTERS
(1.2 X 10⁶ ELECTRONS)
NUMBER OF EVENTS
RELATIVE PULSE HEIGHT
10
20
30
40
50
1
2
3
4
5
6

FIG. 22

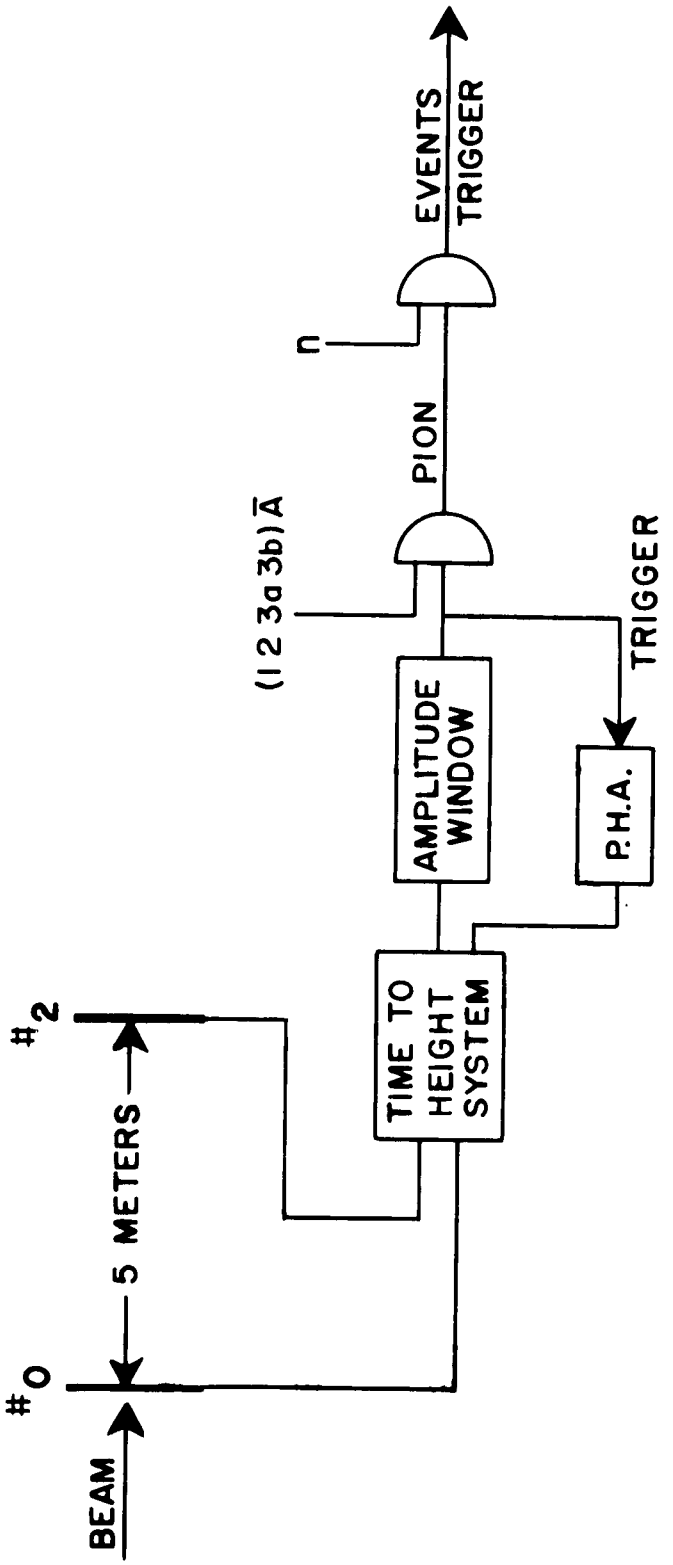

FIG. 23

PION CAPTURE LOGIC

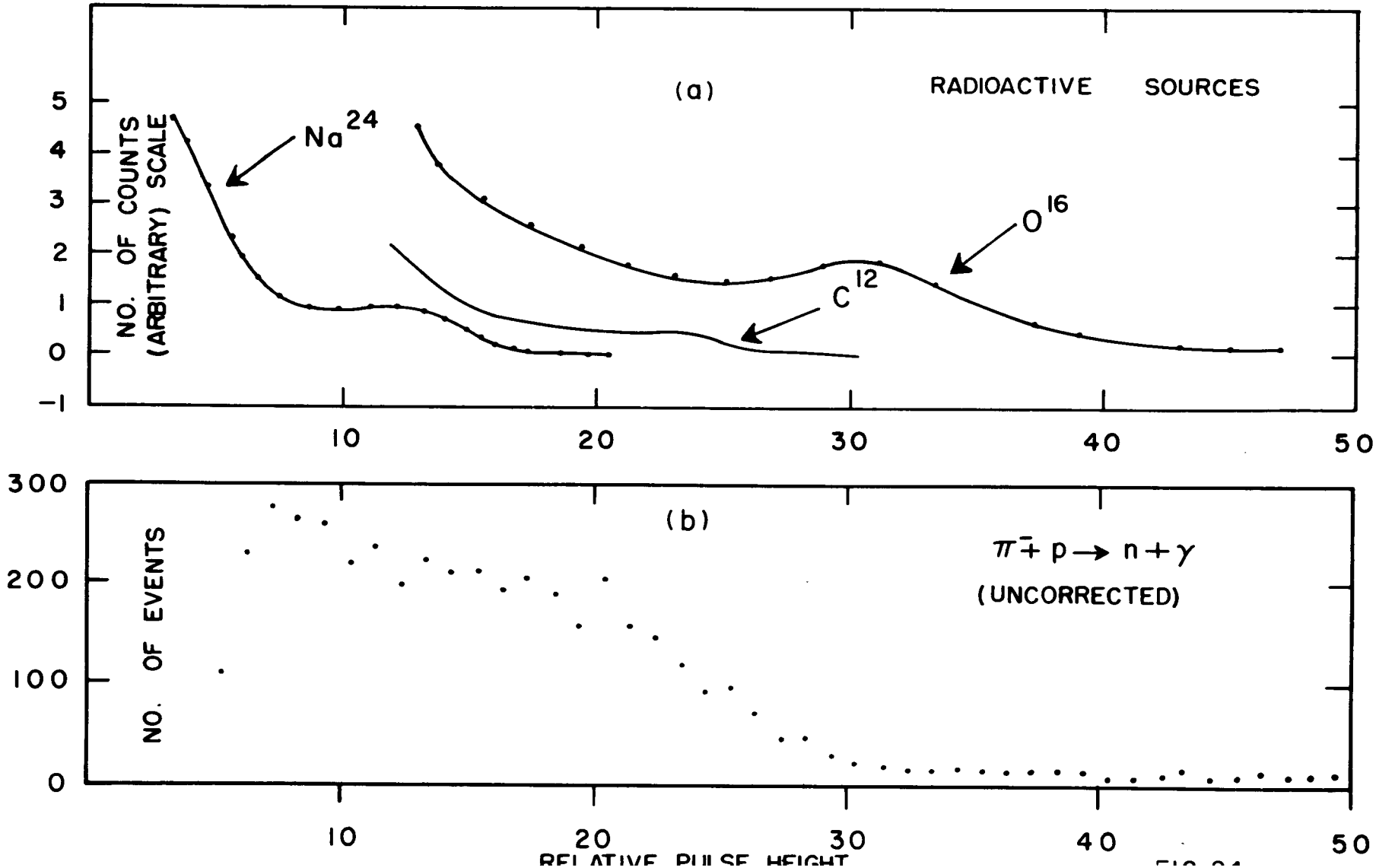
(a)
RADIOACTIVE SOURCES
NO. OF COUNTS (ARBITRARY) SCALE
Na 24
O 16
C 12
5
4
3
2
1
0
-1
10
20
30
40
50
(b)
$\pi^- + p \rightarrow n + \gamma$
(UNCORRECTED)
NO. OF EVENTS
300
200
100
0
10
20
30
40
50
RELATIVE PULSE HEIGHT

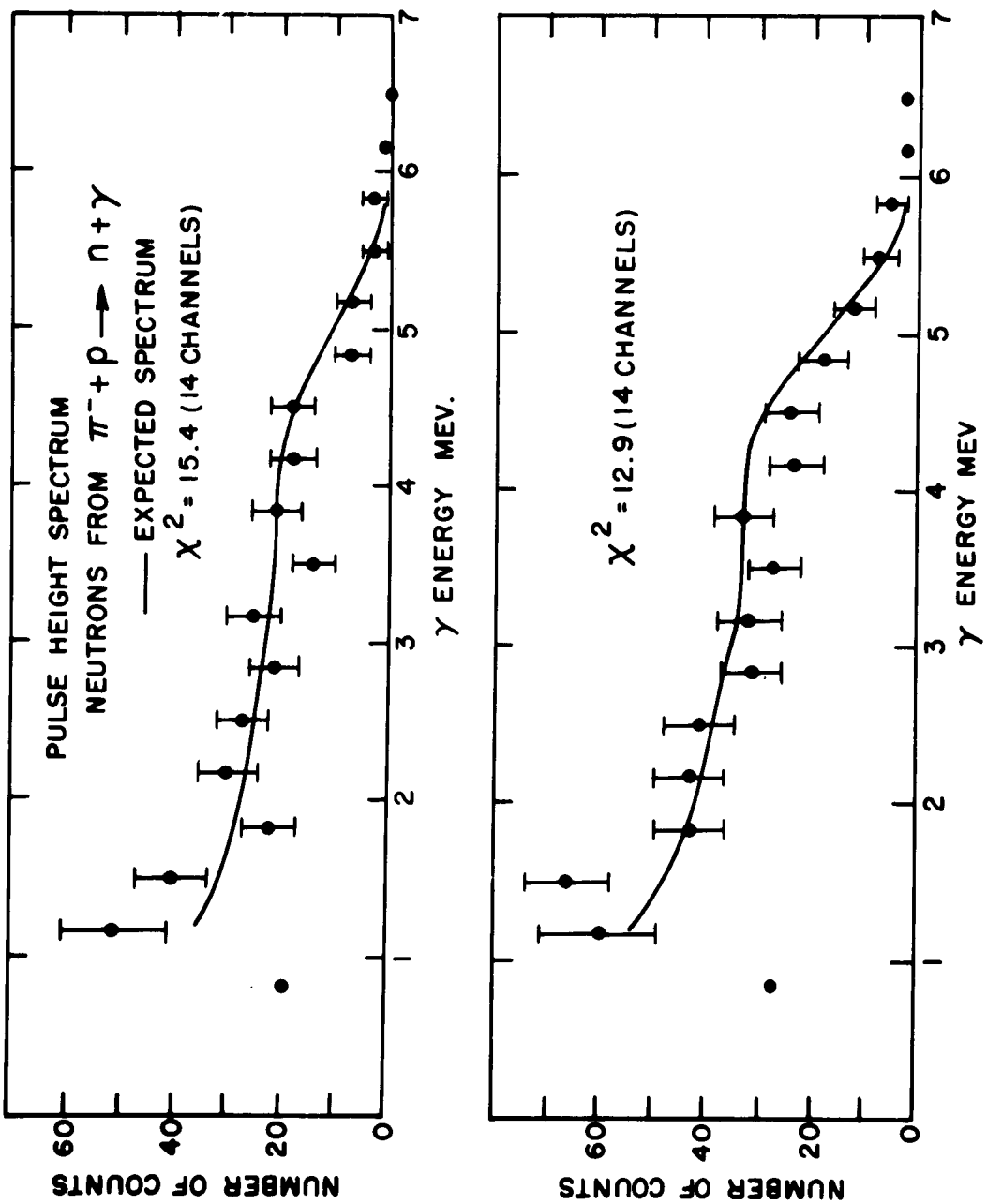
PULSE HEIGHT SPECTRUM
NEUTRONS FROM $\pi^- + p \rightarrow n + \gamma$
— EXPECTED SPECTRUM
χ^2 = 15.4 (14 CHANNELS)
NUMBER OF COUNTS
γ ENERGY MEV.
χ^2 = 12.9 (14 CHANNELS)
NUMBER OF COUNTS
γ ENERGY MEV

FIG. 25

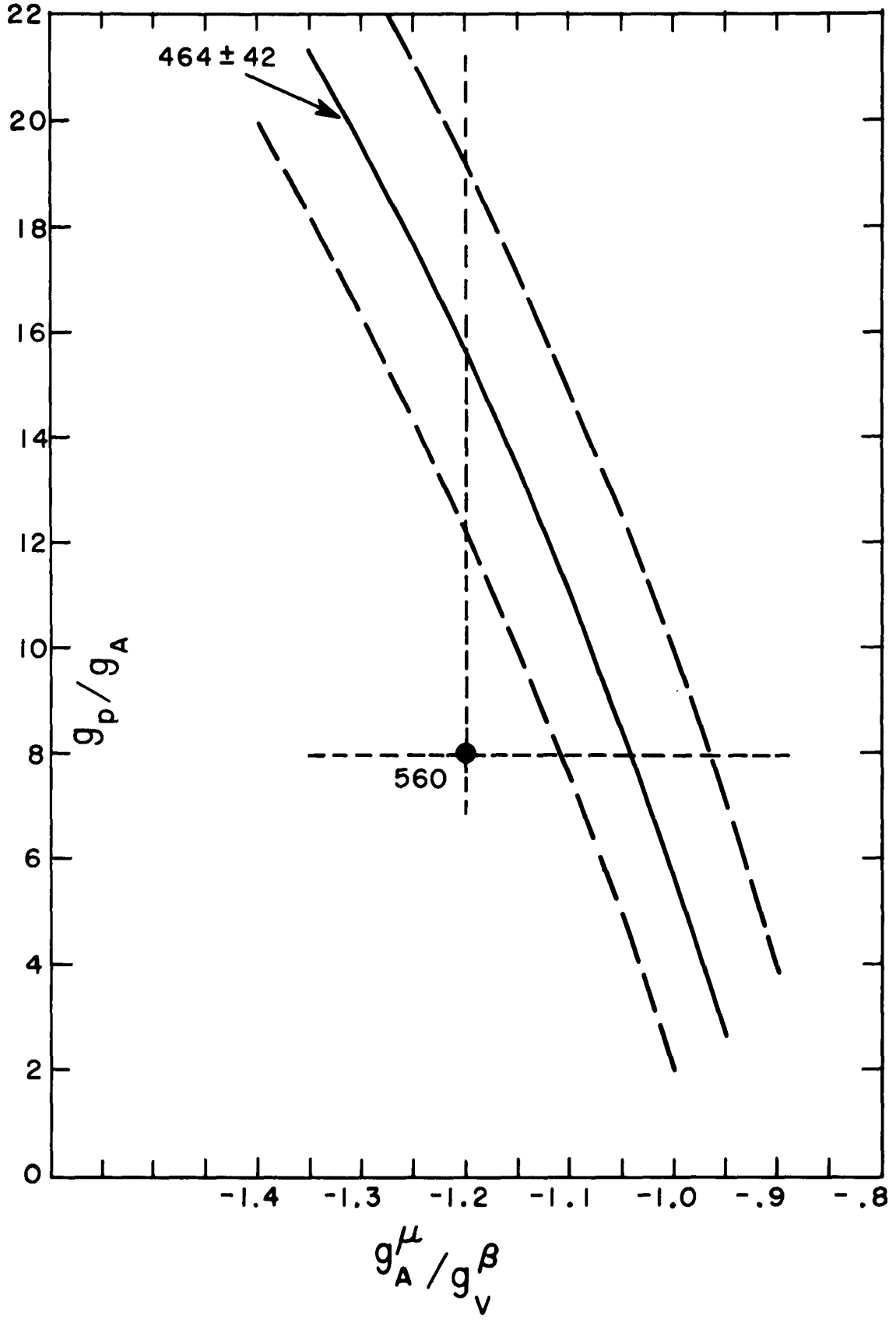
464 ± 42
560
22
20
18
16
14
12
10
8
6
4
2
0
-1.4
-1.3
-1.2
-1.1
-1.0
-.9
-.8
g_p/g_A
g_A^μ/g_V^β

FIG. 26

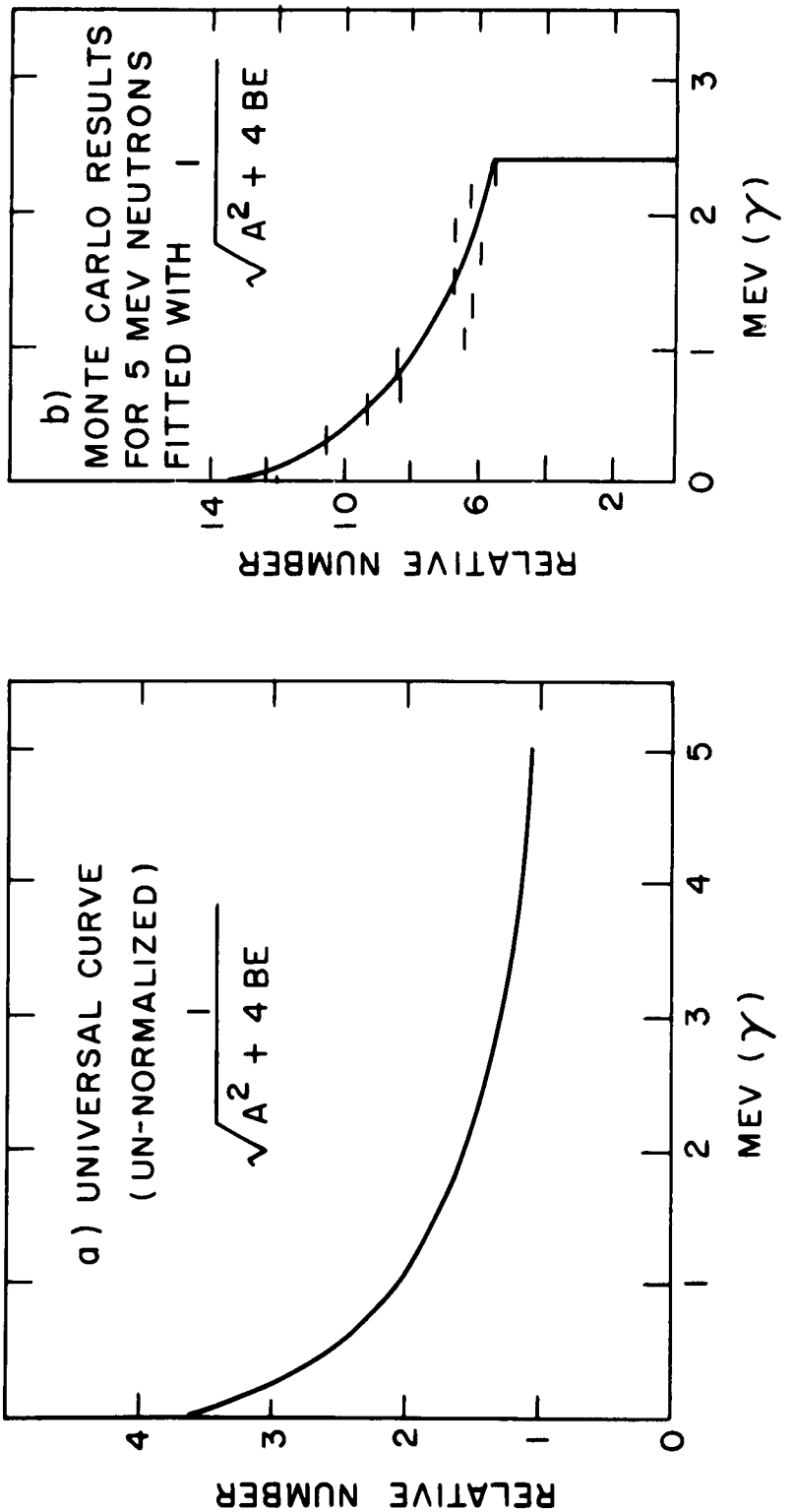
a) UNIVERSAL CURVE
(UN-NORMALIZED)
$\frac{1}{\sqrt{A^2 + 4BE}}$
RELATIVE NUMBER
MEV (γ)
0
1
2
3
4
5
b)
MONTE CARLO RESULTS
FOR 5 MEV NEUTRONS
FITTED WITH $\frac{1}{\sqrt{A^2 + 4BE}}$
RELATIVE NUMBER
MEV (γ)
2
6
10
14
0
1
2
3

FIG. 27

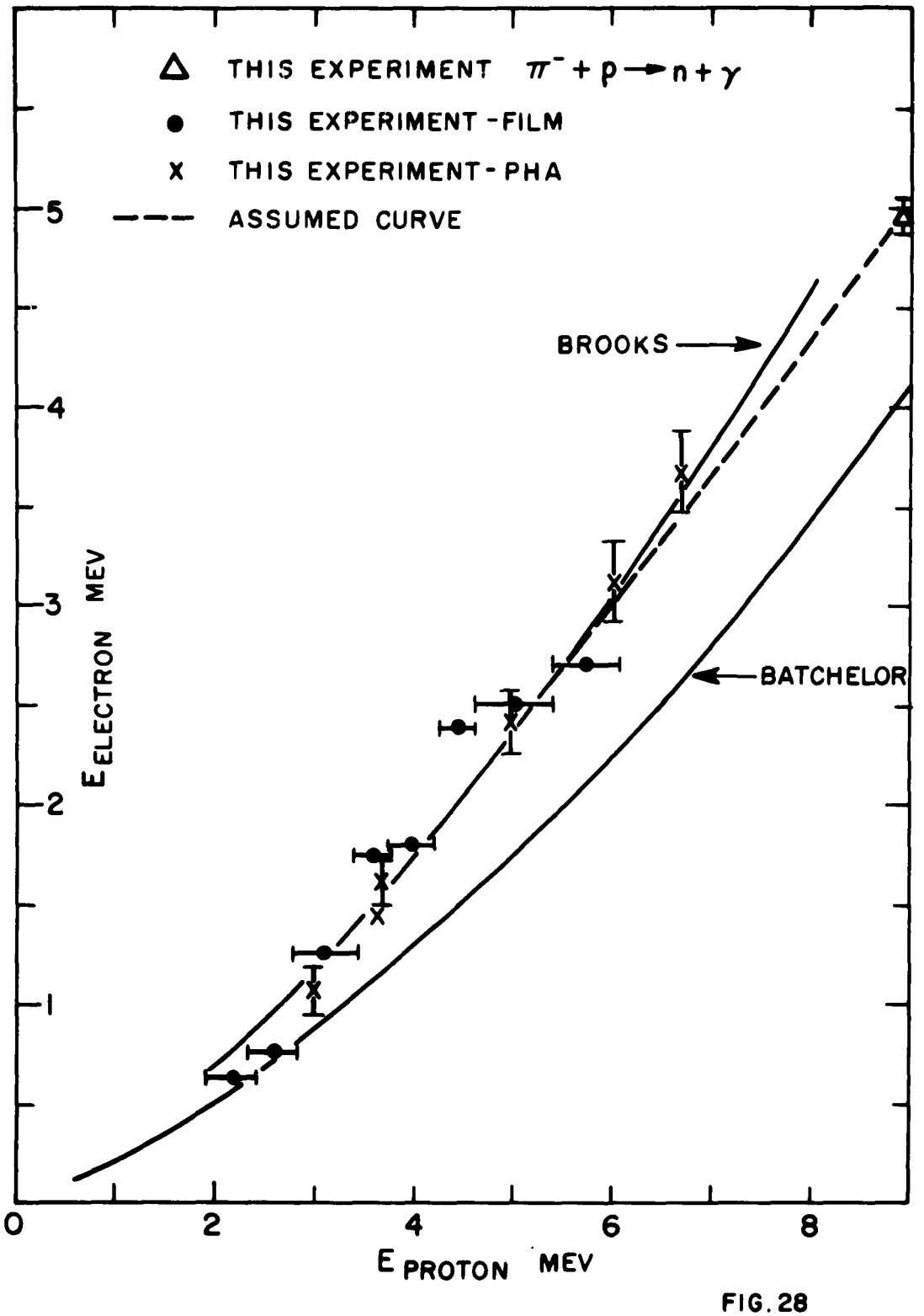
THIS EXPERIMENT $\pi^- + p \rightarrow n + \gamma$
THIS EXPERIMENT - FILM
THIS EXPERIMENT - PHA
ASSUMED CURVE
BROOKS
BATCHELOR
$E_{ELECTRON}$ MEV
E_{PROTON} MEV
0
2
4
6
8
1
2
3
4
5

FIG. 28

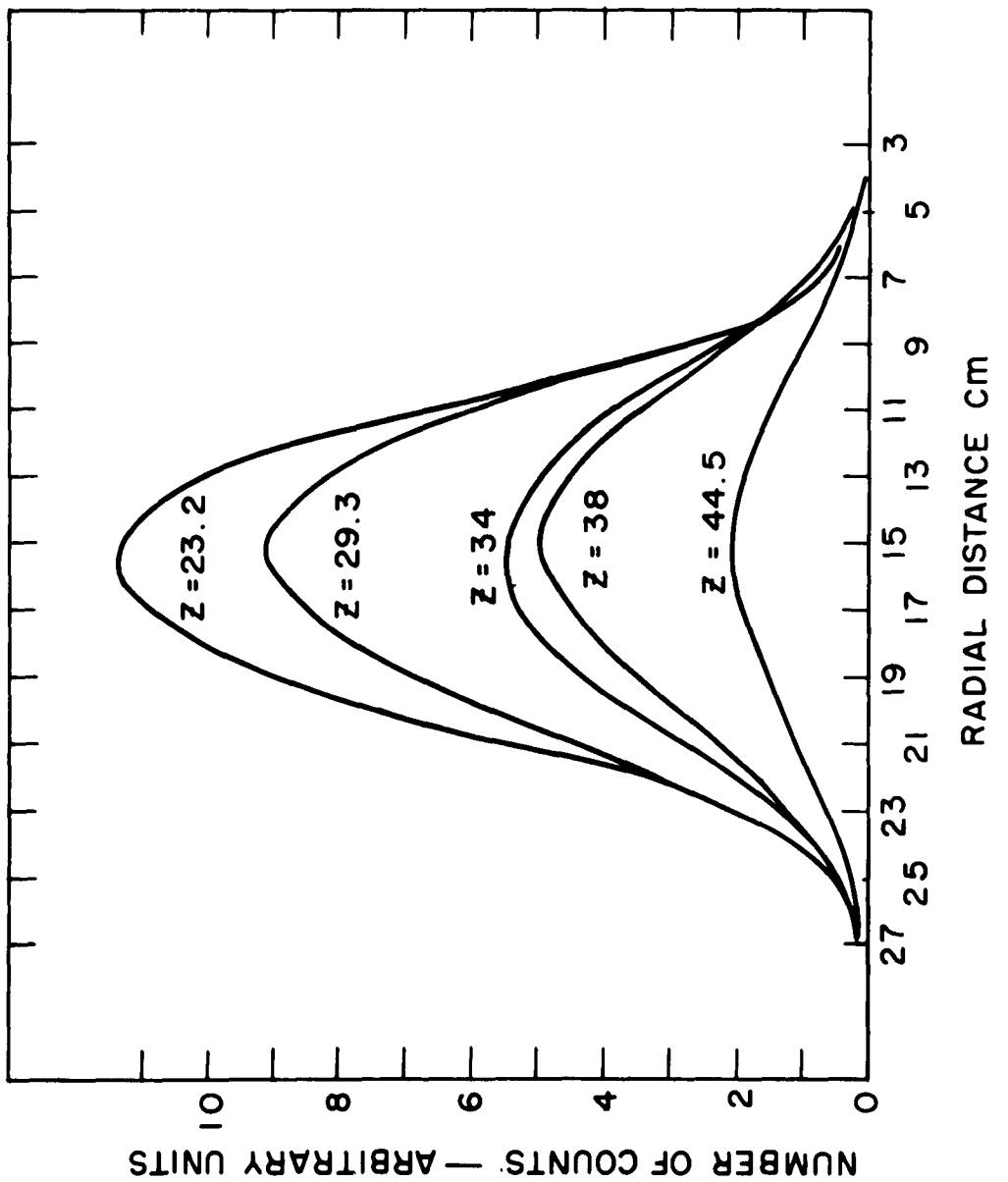
NUMBER OF COUNTS — ARBITRARY UNITS
0
2
4
6
8
10
RADIAL DISTANCE cm
3
5
7
9
11
13
15
17
19
21
23
25
27
Z = 23.2
Z = 29.3
Z = 34
Z = 38
Z = 44.5

FIG. 29

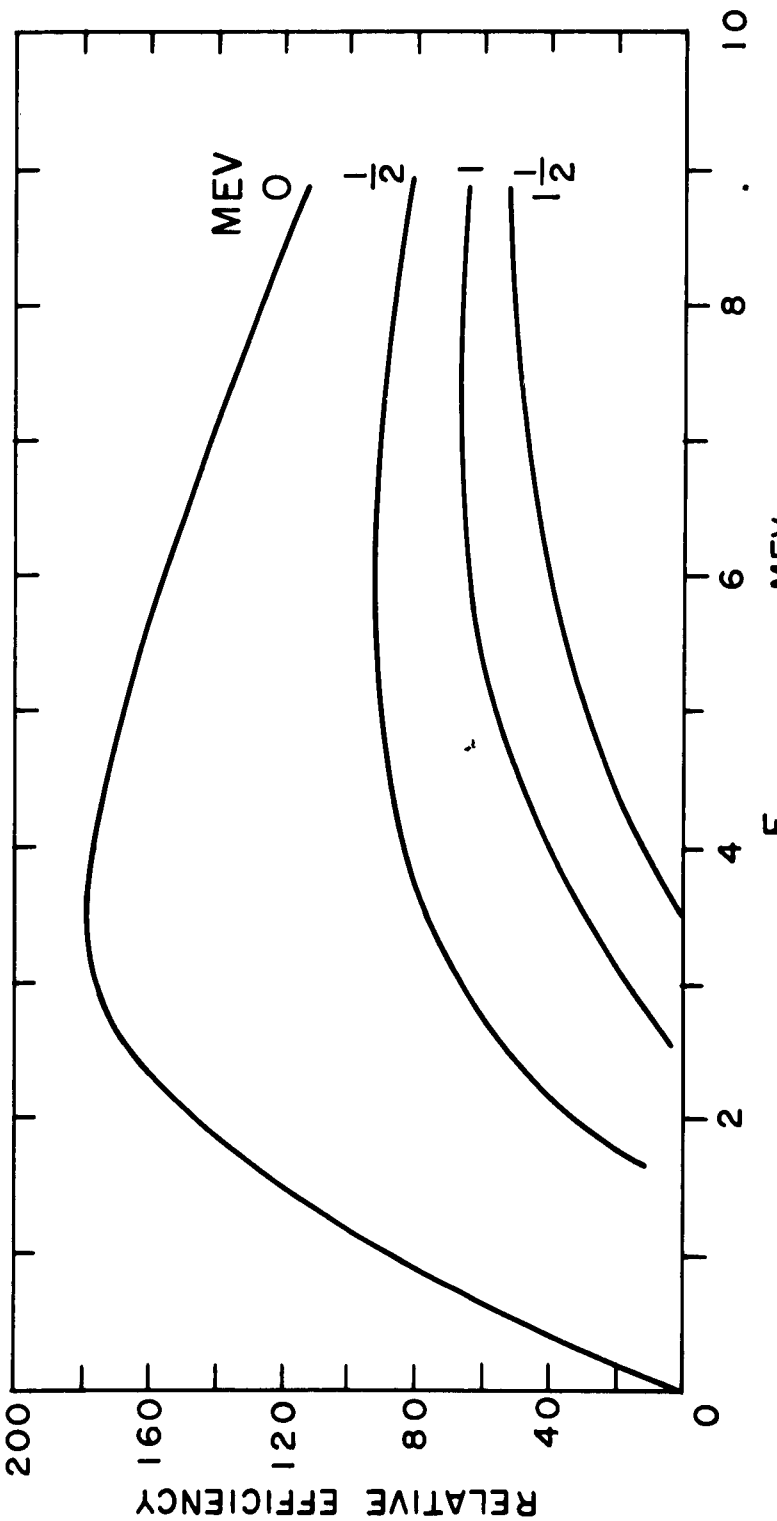
RELATIVE EFFICIENCY
200
160
120
80
40
0
2
4
6
8
10
E NEUTRON MEV
MEV
0
1/2
1
1 1/2

FIG. 30